THE UNIVERSITY OF
WARWICK

AUTHOR: **Richard Lake** DEGREE: **Ph.D.**

TITLE: **Consequences of Fast Ion Driven Modes in MAST**

DATE OF DEPOSIT: .....

I agree that this thesis shall be available in accordance with the regulations governing the University of Warwick theses.

I agree that the summary of this thesis may be submitted for publication.

I **agree** that the thesis may be photocopied (single copies for study purposes only).

Theses with no restriction on photocopying will also be made available to the British Library for microfilming. The British Library may supply copies to individuals or libraries. subject to a statement from them that the copy is supplied for non-publishing purposes. All copies supplied by the British Library will carry the following statement:

> "Attention is drawn to the fact that the copyright of this thesis rests with its author. This copy of the thesis has been supplied on the condition that anyone who consults it is understood to recognise that its copyright rests with its author and that no quotation from the thesis and no information derived from it may be published without the author's written consent."

AUTHOR'S SIGNATURE: .....

USER'S DECLARATION

1. I undertake not to quote or make use of any information from this thesis without making acknowledgement to the author.
2. I further undertake to allow no-one else to use this thesis while it is in my care.

DATE SIGNATURE ADDRESS

.....

.....

.....

.....

.....

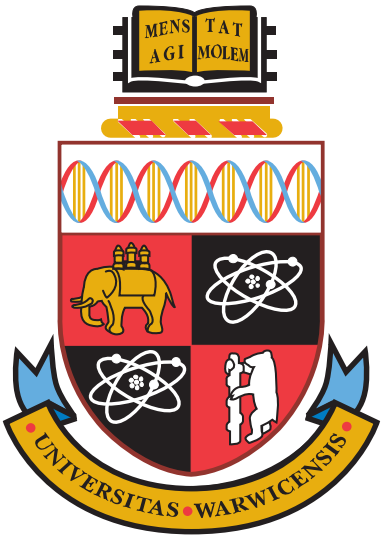

Consequences of Fast Ion Driven Modes in MAST

by

Richard Lake

Thesis

Submitted to the University of Warwick

for the degree of

Doctor of Philosophy

Centre for Fusion, Space and Astrophysics.

May 2013

THE UNIVERSITY OF WARWICK

Contents

List of Tables

List of Figures

Acknowledgments

I would first like to thank Hayleigh Barnett, since without her endless kindness and support I would not have been able to complete this PhD. I would also like to say thank you to my family who have encouraged and inspired me throughout, and to my wonderful friends for their boundless humour.

Thank you to Dr Simon Pinches (CCFE/ITER Organization) and Dr Erwin Verwichte (University of Warwick) for acting as my supervisors. I owe a great deal of thanks to everyone at CCFE who has assisted me with my research, in particular to Dr David Dickinson, Dr Sarah Newton and Dr Ian Chapman for going out of their way and giving up their time to help me, and to Dr Ken McClements for his support over the last year. Thanks also to Sarah Elmore, Stuart Henderson, Matt Leyland and Nick Walkden for making CCFE an enjoyable place to work.

This thesis includes work which is due in whole or in part to collaboration with other scientists: The analysis of the experimental Neutron Camera data and the LINE2 interpretation of the simulated Neutron Camera data that I have included in Chapter 7 was performed by Iwona Wodniak and Marco Cecconello (Uppsala University, Sweden). The MAST fast ion distribution function that I have used in Chapters 5-7 was provided by Rob Akers (CCFE). The MAST-U fast ion distribution function that I have included in Chapter 5 was determined from TRANSP runs that were provided by Dave Keeling (CCFE). The optical LCFS analysis of the equilibrium using the OFIT code that I used in Chapter 5 was performed by Robert Voorhoeve and Gillis Hommen (Technishe Universiteit Eindhoven, The Netherlands). I am grateful to all of these people for their contributions.

This work has been made possible through funding provided by EPSRC and CCFE.

Declarations

This thesis is submitted to the University of Warwick for admission to the degree of Doctor of Philosophy. The work presented was performed at Culham Centre for Fusion Energy and the University of Warwick under the supervision of Dr Simon Pinches and Dr Erwin Verwichte during the period October 2009 to May 2013. None of the research reported here has been submitted to the University of Warwick or any other academic institution for admission to another degree. Some parts of the work reported in this thesis have been published in peer reviewed journals and reported at conferences, a list is included on page 143.

I declare that the work presented in this thesis, other than the contributions listed in the acknowledgements or cited in the text, is my own.

Richard Lake, May 2013.

Abstract

As we enter the era of burning plasmas in next step devices such as ITER, the confinement of fusion born α-particles for sufficient duration that they impart their energy to the bulk fuel ions in order to maintain the thermonuclear burn is an important challenge in magnetically confined fusion. Fast ion driven plasma instabilities can cause significant redistribution and loss of the suprathermal energetic particle (EP) population, degrading performance. With dimensionless parameters such as the ratio of fast ion to thermal ion beta ($\beta_{\mathrm{fi}}/\beta_{\mathrm{th}} \sim 50\%$) and the relative fast ion velocity to the Alfvén velocity ($v_{\mathrm{fi}}/v_{\mathrm{A}} \sim 2$) similar to those anticipated in ITER, the Mega Ampere Spherical Tokamak (MAST) provides the ideal place to study such instabilities. During periods of Neutral Beam Injection (NBI) heating, 'fishbone' instabilities are observed that coincide with a reduction to the fusion rate measured by drops in the neutron emission. Via experimental observations, fishbones are identified to be low frequency internal kink modes that burst in amplitude and chirp downwards in frequency and are synonymous with high power tokamak discharges on a wide range of devices around the world.

This thesis provides a detailed analysis of what occurs during a single fishbone event. Experiments have been performed on MAST that have been interpreted using fast ion plasma physics codes. Modelling of the instability shows a resulting flux of fast ions away from the core, providing evidence at a fundamental level that they drive sufficient levels of anomalous fast ion transport to explain experimental observations. The diffusivity is shown to scale with mode amplitude, and the effect of altering other fishbone parameters within the scope of the experimental observations have been explained by identifying the extent of the fast ion population that is resonant with the mode. Resonant surfaces that sweep through phase space during the chirp are presented that coincide with populous domains of the EP distribution function; it is the gradients in this distribution function that define the drive and or damping of the instability. Via the use of synthetic diagnostics, changes to the radial profiles of neutron emissivity caused by a fishbone are shown to match those measured experimentally.

Chapter 1

Introduction

In 1920 English astrophysicist Arthur Eddington gave a talk at the Presidential Address of the British Association entitled 'The Internal Constitution of the Stars' [1]. In his lecture, Eddington outlined for the first time the process that powers stars. Until this point it was thought that stars were powered by the 'contraction hypothesis' of Kelvin and Helmholtz, in which they slowly contracted, converting gravitational energy into heat. This lead to a scientific crisis; it aged the Sun at around 20 million years - younger than the the age put on the Earth by geologists and biologists.

Eddington proposed that 'stellar synthesis' could be the only possible method for powering stars, a process by which the discrepancy between the mass of four hydrogen nuclei and one helium nucleus (shown recently by F.W. Aston to be about 1 part in 120 [2]) is turned directly into energy, the quantity released given by the mass difference by Einstein's equation $E = mc^2$ [3]. Eddington estimated that this well-nigh inexhaustible supply of energy could maintain the heat output of the Sun for 15 billion years, alluding to the fact that one day humans may harness the power of the Sun,

> *This reservoir can scarcely be other than the sub-atomic energy which, it is known, exists abundantly in all matter; we sometimes dream that man will one day learn how to release it and use it for his service.*

1.1 The World Energy Crisis

Since 1950 the number of people in the world has almost trebled to around seven billion, and is predicted to continue rising to over ten billion by the year 2100 [4]. This population explosion, coupled with the improved quality of life in developing

nations such as China, India and Brazil means that the global demand for energy will increase rapidly. Electricity consumption has risen almost 50% since 1990, and is set to continue rising to well over 2×10^5 TWh by the year 2035, as shown in Fig. 1.1(a). While the demand for energy in the developed world (those members of the Organisation for Economic Co-operation and Development (OECD)) is estimated to be relatively stable, a steep rise is predicted for those in the developing world (non-OECD countries).

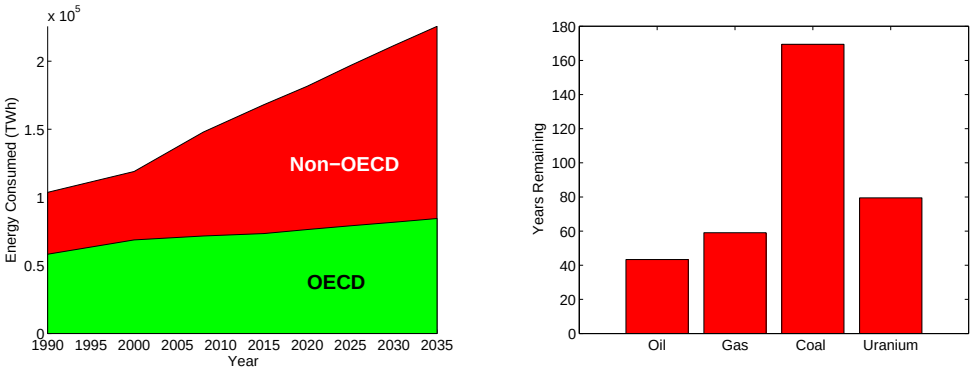

(a) Estimated future energy demand for members and non-members of the OECD. OECD countries are those with high-income economies and remain almost steady, but a large increase is expected amongst non-OECD countries.

(b) Known remaining global energy resources (Exclusively using that resource, estimated at 2011 consumption levels). Data from [5, 6].

Figure 1.1: World energy consumption.

How this increased energy demand will be met is not clear. Conventional energy production is by means of combustion of fossil fuels. This is unsustainable; not only does this process release greenhouse gasses leading to global warming, but the fossil fuels themselves are in limited supply. At 2011 consumption levels, there are only 270 years of known fossil fuels remaining (a number significantly depleted when the increase in demand shown in Fig. 1.1(a) is taken into account - consider, for example, that China alone opens *two* coal power stations every week [7]). Coupled with political unrest leading to unwanted 'commodity dependence' [8] by much of the world on oil-rich regions such as the Arabian Gulf, our current reliance on fossil fuels can not last forever.

Uranium, the fuel used in nuclear fission power stations, is also in limited supply. The fissile isotope ^{235}U makes up around 0.72% of naturally occurring uranium. As the sole source of electricity for the world at 2011 requirements, there is enough ^{235}U remaining to last around 80 years [6]. Fission power stations offer potential as long-term solutions to the energy crisis using other technologies,

for example Fast Breeder Reactors [9]. Nuclear power however remains politically unpopular, despite being the safest known method of electricity production [10, 11].

Renewable energy sources such as solar, hydroelectric and wind power make up 2-3% of world electricity production, and whilst increasing are expected to stay at this level at least for the next twenty five years due to comparable increases in other energy sources [12]. Renewable energy sources are particularly susceptible to their environments - consistent enough wind is hard to find, as are locations viable for hydroelectric power. Solar power offers a genuine contender, although to make a significant contribution to the world's energy requirements would have to be done on a large scale in a region of the world with consistent and bright enough sunlight - again leading to a similar risk of commodity dependence as fossil fuels.

There is no individual solution to the world's energy crisis. Our dependence on fossil fuels must be phased out and replaced by other technologies. A range of renewable sources have been introduced worldwide, where financially and geographically viable. What is really required is a clean, sustainable energy resource that can produce electricity on a large scale for costs comparable to current fossil fuel technology. One such potential source if energy production that fulfils these criteria is nuclear fusion, which has been the subject of much research over the last 60 years.

1.2 Nuclear Fusion

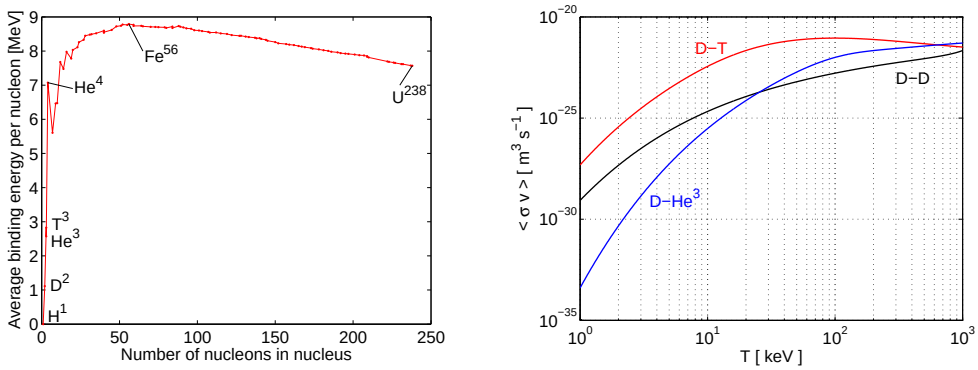

(a) Binding energy per nucleon for the most stable isotope of each element [13].

(b) Reactivity as a function of temperature [14].

Figure 1.2: Nuclear fusion.

As initially alluded to by Eddington in 1920, the mass of a nucleus comprises of the mass of the constituent protons and neutrons (the nucleons) and a 'binding energy'. During a fission reaction, it is the binding energy of a heavy nucleus that is

released when it splits into smaller nuclei. Figure 1.2(a) shows the average binding energy per nucleon for the most stable isotope of each element, in addition to other isotopes of hydrogen; deuterium D and tritium T. The energy released during fission is shown in this figure as the difference between the initial heavy nucleus and the resulting lighter nuclei. The peak in this figure is ^{56}Fe, thus the reaction to split a ^{56}Fe (or any heavier) nucleus is exothermic. For the same reason, fusing together two nuclei that are lighter than ^{56}Fe will release energy. This fusion process offers a more attractive option for energy production due to the abundance and stability of the lighter elements compared to heavy ones such as uranium. It is fusion that powers the sun, and for this reason any nucleus heavier than ^{56}Fe cannot be created in the sun and is produced only in supernovae and laboratories on Earth.

In order to fuse, two nuclei must come sufficiently close together that the nuclear force overcomes the Coulomb repulsion between the two like-charged nuclei. It is therefore the singly charged nuclei (isotopes of hydrogen) that require the lowest energy to fuse. The Coulomb energy can be estimated as the electronic potential between two nuclei. For two hydrogen atoms with charge $q_1 = q_2 = e$, and a typical classical radius $r = 1.0$ fm the potential energy is

$$U = \frac{q_1 q_2}{4\pi\epsilon_0 r} \sim 600 \text{ keV}. \tag{1.1}$$

Four fusion reactions for the isotopes of Hydrogen are given below (the kinetic energy carried by the products are quoted in the brackets, produced by the binding energy discrepancy) [15].

$$\begin{aligned}
^2D + {}^2D &\rightarrow {}^3T \text{ (1.01 MeV)} + p \text{ (3.02 MeV)} \\
^2D + {}^2D &\rightarrow {}^3He \text{ (0.82 MeV)} + n \text{ (2.45 MeV)} \\
^2D + {}^3T &\rightarrow {}^4He \text{ (3.5 MeV)} + n \text{ (14.1 MeV)} \\
^2D + {}^3He &\rightarrow {}^4He \text{ (3.6 MeV)} + p \text{ (14.7 MeV)}
\end{aligned}$$

Each fusion reaction has an associated reactivity $\langle\sigma v\rangle$, which is a velocity-averaged cross section. This governs the reaction rate of the fusion and is strongly dependent on the plasma temperature T. Figure 1.2(b) shows the reactivity as a function of the temperature, assuming a Maxwellian velocity distribution. The two $D-D$ reactions are equally likely and their reactivity is very similar so are represented by the same line in the figure. The $D-T$ reaction is clearly favourable (the red line), as it affords the highest energy yield at the lowest temperature. These fuels are virtually inexhaustible; deuterium can be extracted from seawater using electrolysis and tritium may be produced in-situ via neutron bombardment of lithium which is sufficiently abundant on Earth. The products of the $D-T$ reaction are a neutron

with 14.1 MeV of energy and a helium nucleus (α-particle) with 3.5MeV of energy; both of which are significantly more energetic than the fuel.

Figure 1.2(b) shows that reactivity peaks at a deuterium energy of $\sim$ 100 keV; lower than the 600 keV required to overcome the Coulomb repulsion. The high energy tail of the distribution function can however quantum mechanically tunnel though the Coulomb barrier at temperatures lower than this, so a fuel temperature of $\sim$ 20 keV ($\sim$ 200 million K) is sufficient. At temperatures as high as this it is fully ionised and forms a plasma. To produce energy, the plasma must be confined by a device at this high temperature at a sufficiently high density and for long enough that the fusion power emitted P_F is greater than the externally applied heating power P_H. This scenario is referred to as having a 'fusion energy gain factor' Q greater than one, where $Q = P_F/P_H > 1$. To achieve this, the energy leaving the plasma must exceed the heating energy entering the plasma. The rate of energy loss P_L is the total plasma energy W divided by the characteristic time it takes for energy to escape the plasma, known as the energy confinement time τ_E.

$$P_L = \frac{W}{\tau_E} = \frac{3\overline{nT}V}{\tau_E}, \tag{1.2}$$

where $3\overline{nT}$ is the average energy per unit volume V assuming a Maxwellian plasma and $T = k_B T'$ is the temperature in energy units (generally accepted in this field [16]) that is equivalent to T' Kelvin. In addition to the externally applied heating, the hot α-particle that was a product of the fusion slows down in the plasma, and in doing so imparts energy to the background ions. This form of heating is known as 'α-particle heating'. Assuming the plasma is comprised of balanced densities of deuterium and tritium $n_T = n_D$, the total α-particle heating power is [16]

$$P_\alpha = \frac{1}{4}\overline{n^2 \langle \sigma v \rangle} E_\alpha V. \tag{1.3}$$

This leads to a power balance, whereby the power lost from the plasma is balanced by the heating put in, $P_H + P_\alpha = P_L$,

$$P_H + \frac{1}{4}\overline{n^2 \langle \sigma v \rangle} E_\alpha V = \frac{3\overline{nT}V}{\tau_E}. \tag{1.4}$$

where E_α is the reaction energy carried by the α-particle. Since the power lost is linear with the plasma temperature, but the α-particle heating increases more rapidly (see Fig. 1.2(b)), there is a point at which the α-particle heating exceeds the power loss and the externally applied heating can be turned off. This point

is known as the 'ignition condition', beyond which exists a self-sustained 'burning' plasma. From Equation 1.4 the requirement for the plasma to achieve this is

$$n\tau_E = \frac{12}{E_\alpha}\frac{T}{\langle\sigma v\rangle}. \tag{1.5}$$

For plasma temperatures in the region 10-20 keV, the reaction rate is well approximated by $\langle\sigma v\rangle \simeq 1.1\times10^{21}$ T^{2}m^{3}s^{-1} so that for a $D-T$ fusion-produced α-particle, where $E_A = 3.5$ MeV the modified Lawson criterion [17] is

$$nT\tau_E > 3\times10^{21}\mathrm{m}^{-3}\mathrm{keVs} \tag{1.6}$$

that states the 'triple product' required for burning plasma (modified as Lawson assumed the plasma was externally heated, neglecting α-particle heating).

A device is needed that is capable of confining a sufficiently hot, dense plasma for long enough that the triple product exceeds the value set by the Lawson criterion. The first of these is gravitational confinement fusion (GCF) which is naturally occurring, and powers stars. Another form of nuclear fusion is inertial confinement fusion (ICF). This is a process in which a small sphere of deuterium and tritium is heated extremely quickly, causing the surface of the sphere to rapidly expand. The implosion of the surface ionises the fuel, sending a shock wave through it. The Lawson criterion is surpassed by means of an extremely high nT despite the short confinement time. Experiments are ongoing at the National Ignition Facility (NIF) [18]. The third approach to fusion is magnetic confinement fusion (MCF), whereby the charged plasma is confined by an electromagnetic (EM) field. The most technologically mature approach to MCF is by means of the tokamak configuration [19], which comes from the Russian **токамак** (**to**roidal'naya **ka**mera s **ma**gnitnymi **k**atushkami), literally translated as 'toroidal chamber with magnetic field'.

1.3 The Tokamak

The tokamak is a device whereby a fusion plasma is confined in a torus shaped magnetic field. When referring to such devices it is instructive to do so using a toroidal coordinate system (r,ζ,θ), where r is the minor radius, ζ is the toroidal angle and θ is the poloidal angle, see Figure 1.3. The magnetic axis is located at $R = R_0$, where R is the major radius.

The plasma is principally confined by a toroidal field B_ζ. This alone is insufficient to achieve an equilibrium, so a secondary poloidal field B_θ is also present to provide stability, distinguishing it from preceding devices such as the Z-pinch

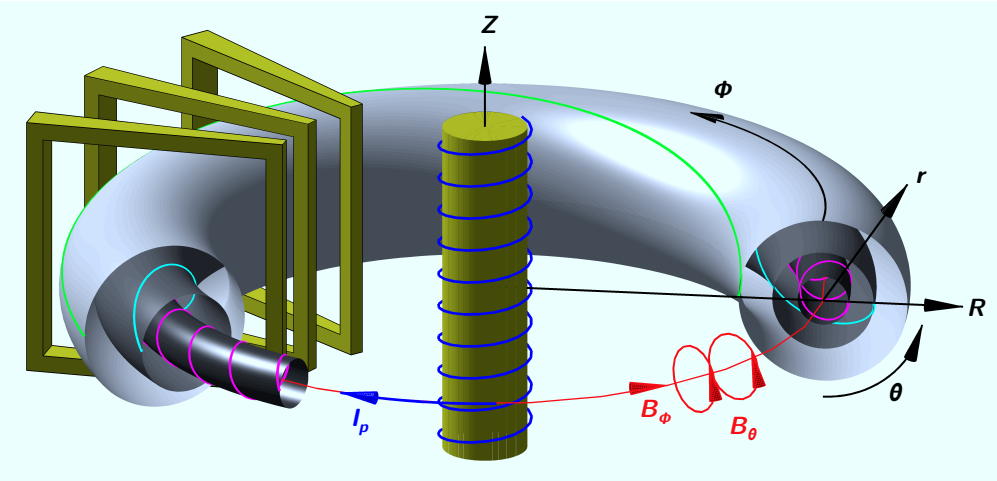

Figure 1.3: Tokamak schematic. The plasma is confined by poloidal and toroidal magnetic fields. Particles gyrate around field lines (green, cyan and magenta) which lie on surfaces of constant flux (shown in grey). Magnetic coils are shown in yellow. The primary coil in the centre of the torus drives the plasma current I_p. Three examples of toroidal field coils are shown on the left (these are equally spaced around the whole torus in a tokamak) which provide the B_ζ. B_ζ and I_p can be in equal or opposite directions depending on the device, see Appendix A.

which were inherently vulnerable to magnetohydrodynamic (MHD) instabilities (a review of the Z-pinch is given in [20]). The combination of these two results in helical field lines traversing the torus, around which the confined charged particles gyrate. The helical field lines exist on radially concentric 'flux surfaces' that have approximately constant pressure and temperature, shown by the grey surfaces in Figure 1.3; perpendicular to these flux surfaces however exist significant gradients. The poloidal field B_θ is produced principally by a toroidal plasma current I_p. The current is driven by a toroidal magnetic field induced by a flux change through the torus. A current 'ramp up' is driven through a primary coil located around the torus, and coupled to the plasma via the same induction interaction as employed by a transformer. The poloidal field is limited by the duration of the current ramp up. For this reason, so called 'non-inductive' current drive is required for future tokamaks in order to retain stability when the current in the solenoid plateaus [21]. The finite resistivity causes the plasma to heat up, a technique known as 'ohmic heating'. The resistivity η is temperature dependent $\eta \propto T^{-3/2}$, so this is limited to $\gtrsim 10$ keV [16]; additional heating is therefore required. This is provided by means of electromagnetic waves or injected beams of high energy atoms known as Neutral Beam Injection (NBI).

The plasma is prevented from coming into contact with the walls of the

tokamak by the confining magnetic field. An exhaust, however, is required in order to remove the unwanted charged fusion products, often referred to as helium 'ash'. This is done in one of two ways; the first is by means of a 'limiter configuration'. A limiter is an axisymmetric component of the tokamak that protrudes into the plasma, defining an outer boundary. The second is the use of a 'divertor configuration'. In this case, the magnetic field is modified to produce an 'x-point'; beyond which the field lines come into contact with a dedicated component called the divertor, which can handle the high heat load required as the exhaust of the tokamak. Tokamak divertors were initially developed in the 1970s [22] (having been previously implemented in stellerators [23]), subsequently becoming commonplace on devices such as the Joint European Torus (JET) [24, 25] and the Mega Ampere Spherical Tokamak (MAST) (but crucially not on the Tokamak Fusion Test Reactor (TFTR)). Advanced configurations are currently being investigated [26], including the 'super-X divertor' which will be an integral part of MAST-Updgrade (MAST-U) [27].

Including those that have been proposed, decommissioned and are currently running, there are a total of 181 tokamaks worldwide [28]. The highest ever fusion energy gain factor recorded on a tokamak was on JET [29] in 1997 with a quasi steady-state gain of $Q_{\mathrm{DT}} = 0.7$ when 16.1 MW of fusion energy was produced by a $D-T$ plasma [30]. The absence of tritium handling facilities at the Japanese large Tokamak (JT-60) [31] mean that only $D-D$ plasmas are studied, however the highest $D-T$ equivalent energy gain on this device $Q_{\mathrm{DT}}^{\mathrm{eq}} = 1.25$ surpasses the break even point [32]. A future power plant will require a $Q > 10$, which is the baseline for long pulse (>1000 s) operation on the next step fusion tokamak experiment ITER [33].

1.3.1 The Spherical Tokamak

Conventional tokamaks have a 'large aspect ratio', where the aspect ratio is the ratio of the major radius R to the minor radius r, and is generally quoted in terms of the inverse aspect ratio $\varepsilon = r/R$. A concept for a low aspect ratio 'spherical torus' device was suggested initially in 1986 [34], with an aspect ratio of $\varepsilon > 0.5$. Known as a spherical tokamak (ST), the low aspect ratio means that they look more like a cored apple than the elongated torus of a traditional tokamak shown in Figure 1.3. There are currently 34 proposed, decommissioned or operational STs in the world [28]. The primary goal of the ST was to reach an unprecedented high-β limit, where β is the ratio of plasma pressure to the magnetic pressure [34]. In addition to this, STs offer good MHD stability due to high edge safety factor q and large elongation

κ. The high natural elongation offers MHD stability because the field lines spend more time on the High Field Side (HFS) of the device. The goal was achieved in 1998 with a record breaking value of volume-averaged $\beta \geqslant 30\%$ set by the Small Tight Aspect Ratio Tokamak (START) [35]. Future ST power plants have been proposed [36], which require large (92%) non-inductive current drive because of limited space for a central solenoid and its associated shielding.

The work in this thesis has been carried out using the MAST device [37] based at Culham Centre for Fusion Energy (CCFE) in Oxfordshire, typical parameters of which are given in Table 1.1. It has a scientific programme focused on developing the ST as a Component Test Facility (CTF) and/or a power plant, as well as researching key physics requirements needed in the development of ITER [38]. The other major ST in the world is the National Spherical Tokamak Experiment (NSTX) in Princeton, USA [39].

Parameter	**Value**
Major Radius	0.85 m
Minor Radius	0.65 m
Plasma Volume	8 m^2
Plasma Current	$<$ 1.45 MA
Toroidal Field	0.3 - 0.7 T
Auxiliary heating power	$<$ 4.4 MW (70 keV)
Typical Pulse Length	$<$ 0.6 s
Typical Density	$< 10^{20}$ particles/m^2
Elongation	2
Triangularity	0.5

Table 1.1: MAST parameters.

1.4 Fast Ion Driven Instabilities

For MCF to become a viable energy source it is imperative that the charged energetic fusion products are confined for sufficient duration that they impart enough of their energy to the fuel ions for them to in turn surmount the required temperature to fuse, achieving a self-sustained burning plasma. They are therefore an intrinsic component of burning plasma experiments such as ITER. In addition to heating the plasma, the energetic particles (EPs) must be confined in order to minimise losses which can result in damage to the vessel first wall and other sensitive plasma facing components. For this reason, the study of EP transport in fusion plasmas is a key area of research within the fusion community. Populations of EPs include isotropic fusion born particle populations, typically α-particles in the case of $D-T$

fusion which exist in JET and will be present in ITER and a demonstration power plant. Additional heating via NBI and resonant microwave interaction results in anisotropic EP populations.

The suprathermal ion population in MAST arises both directly, via the ionisation of NBI atoms, and indirectly via fusion reactions occurring between the beam ions with themselves (beam-beam fusion) and the beam ions with the thermal ion population (beam-bulk fusion). The fusion contribution from the thermal plasma (bulk-bulk fusion) is negligible, since the thermal plasma is 'cold' (typically 1 keV) compared with the beam ions typically injected at 60 keV. The large Larmor radius of the fusion products due to the low magnetic field in MAST (typically 0.3-0.6 T) results in orbit trajectories that are not confined, so the resulting population is made up largely of the thermalised NBI ions.

Various instabilities exist in tokamak plasmas that determine the confinement and may cause redistribution of these fast ions away from the core where they are required to heat the plasma. They include normal modes of the background plasma determined by the thermal ion population, which may exist even in the absence of the EP population, as well as energetic particle modes (EPMs) which manifest themselves only when the EP pressure builds to a significant enough level [40].

Due to the nature of the ST, they require a relatively low toroidal field B_ζ compared to conventional aspect ratio tokamaks. This results in a comparatively large fast ion Larmor radius ($\rho_{\text{fi}} \propto 1/B_\zeta \sim 0.2a$) which, in conjunction with supra-Alfvénic fast ion velocities ($v_{\text{fi}} > v_{\text{A}}$), yields a regime in which fast ion driven instabilities play a significant role [41]. The dimensionless plasma parameters in MAST such as the ratio of fast ion to thermal ion beta ($\beta_{\text{fi}}/\beta_{\text{th}} \sim 50\%$) and the relative fast ion velocity to the Alfvén velocity ($v_{\text{fi}}/v_{\text{A}} \sim 2$) are similar to those anticipated for both ITER and a future demonstration power plant, making it an ideal candidate on which to study fast ion driven instabilities [42].

1.4.1 Fishbones

Periods of NBI heating in MAST coincide with a diverse array of EPMs. One such instability is a low-frequency internal kink mode which has a bursting nature and rapidly chirps downwards in frequency during its lifetime, referred to as 'fishbone' modes due to their characteristic signal in the magnetic pickup coils, which resemble the bone structure of a fish [43]. Initially seen on the Poloidal Divertor Experiment (PDX) [43], fishbones have been observed on other devices such as TFTR [44], Doublet 3^{rd} generation 'D'-shaped Tokamak (DIII-D) [45], JET [46] and the Axially Symmetric Divertor EXperiment - Upgrade (ASDEX-U) [47], as well as the spher-

ical tokamaks START, MAST [48] and the NSTX [49]. Their proliferation across devices means that they are considered to be synonymous with high-energy tokamak discharges, and seen to be a significant issue for future devices [50], including ITER [51] and JT-60 Super Advanced (JT-60SA) [52].

Via resonant wave-particle interaction, energy is exchanged between the fish-bone modes and the fast ion population. This results in redistribution of the fast ions in both velocity space and real space. They are moved radially away from the site of injection, potentially into orbits that are no longer confined by the device and are therefore lost from the plasma. This is done on a timescale of a few milliseconds, which is far shorter than the thermalisation time of the EPs (known as the 'slowing down time' of the fast ion distribution function). These modes are therefore responsible for significant degradation to the NBI heating efficiency. One may observe the reduction in the core density by means of a drop in the fusion rate, measured by a drop in the neutron emissivity which is coincidental with the detection of the fish-bone modes [48], as well as increased signal in the Fast Ion D_α (FIDA) diagnostic [53].

1.5 MAST Diagnostics

To understand the dynamics of the tokamak plasma discharge, models must match the experimentally observed events as accurately as possible. To do this, data from the comprehensive set of diagnostics present on MAST is utilised. The diagnostics that are relevant for this fast ion study are outlined below.

To determine the equilibrium plasma state, two Thomson Scattering (TS) systems [54] allow electron density n_e and temperature T_e measurements to be taken every 4-5 ms with 1-2 cm spatial resolution. Also, a multi-chord Motional Stark Effect (MSE) system [55] allows for measurement of the current profile (and subsequent diagnostic of the q-profile). Ion density measurements can also be made using the multi-chord Soft X-Ray (SXR) system. A Charge eXchange Recombination Spectroscopy (CXRS) system is available to provide ion velocity and temperature profiles [56].

The fast ion population is inferred from the injected NBI parameters along with fast ion density measurements given by the new FIDA system [57]. Fast ion information can also be derived from the neutron diagnostics, comprising of a ^{235}U fission chamber for high time resolution integrated neutron detection [58] and also a Neutron Camera (NC) equipped with a total of four columnated channels; two horizontal channels on the equatorial mid-plane and two diagonal channels looking

below it which allows radial profiles to be built up over multiple shots [59, 60].

Magnetic perturbations to the plasma are measured using Mirnov coils, whereby a change in voltage measured allows $\delta B/B$ to be inferred using Faraday's law. MAST is equipped with a array of Outboard Vertical Mirnov (OMV) coils that are field integrators designed to detect low frequency perturbations (<250kHz) to the equilibrium magnetic field; high frequency (>10MHz) perturbations are detected using the Outboard Mirnov Array for High frequency Acquisition (OMAHA) coil array [61]. Multiple toroidal locations of the Mirnov coils allow for the structure of the perturbation to be determined via mode number analysis.

1.6 Outline of Thesis

This thesis provides an investigation into the fishbone mode on MAST. Experiments are carried out and analysed, with modes identified and modelled. This modelling is interpreted to give quantitative results and provide a comparison with the experimental observations.

The theoretical approach undertaken in the fishbone modelling requires an understanding of how tokamak plasmas behave. This is given by means of a Theoretical Review in Chapter 2, whereby the basics of particle motion are introduced, along with the concept of MHD. This leads on to describe the motion of the fast ions by means of a Lagrangian approach that is used throughout this thesis. Chapter 3 goes into further detail specifically on fishbones, from historical observations to their behaviour MAST. It also explains the experimental work that was done on MAST to obtain data for the computational modelling. An introduction to the code that is used to model the fishbones is given in Chapter 4. The chapter then goes on to explain how the code has been expanded to include a new, high resolution fast ion distribution function that enables improved modelling to be undertaken that is more closely matched to the real experiment. How the fishbone model is built up from the diagnostic data is explained in Chapter 5, which leads to the identification of regions of the fast ion distribution function that are resonant with the mode, and also includes predictions for the future MAST-U device. The subsequent redistribution of the fast ions is shown in Chapter 6, along with transport coefficients which allow the redistribution to be quantified. In Chapter 7, direct comparisons are made with the experimental diagnostics in order to validate what has been found in the simulations. Finally, the thesis is concluded in Chapter 8 and future work is discussed.

Chapter 2

Theoretical Review

2.1 Particle Motion in Toroidal Magnetic Devices

The behaviour of charged particles in plasmas is determined by both the Coulomb interactions of the particles with one another and also by interactions with any externally applied magnetic or electric fields. When considering the motion of charged particles in a plasma, we start with the equation of motion of a single particle of mass m and charge e moving with velocity $\mathbf{v}$ in the presence of an electric field $\mathbf{E}$ and magnetic field $\mathbf{B}$. This is the Lorentz force equation [62]

$$m\frac{\mathrm{d}\mathbf{v}(t)}{\mathrm{d}t} = \mathbf{F}(\mathbf{r},t) + e\left[\mathbf{E}(\mathbf{r},t) + \mathbf{v}(t)\times\mathbf{B}(\mathbf{r},t)\right] \ , \tag{2.1}$$

where $\mathbf{r}$ is the location of the particle, t is the time and $\mathbf{F}$ represents an external force such as gravity. Gravity is ignored in Tokamak plasmas as it is small compared to the externally applied fields. In the presence of a uniform magnetic field but no electric field (or externally applied forces), Equation 2.1 may be written as

$$\frac{\mathrm{d}\mathbf{v}}{\mathrm{d}t} = \frac{e}{m}\left(\mathbf{v}\times\mathbf{B}\right) \ .$$

This can be split into components that are parallel and perpendicular to the magnetic field,

$$\frac{\mathrm{d}\mathbf{v}_{\parallel}}{\mathrm{d}t} = 0 \ , \tag{2.2}$$

$$\frac{\mathrm{d}\mathbf{v}_{\perp}}{\mathrm{d}t} = \frac{e}{m}\left(\mathbf{v}_{\perp}\times\mathbf{B}\right) \ , \tag{2.3}$$

where the motion parallel to the field is constant. Defining a vector $\boldsymbol{\omega}_c$ as

$$\boldsymbol{\omega}_c = \frac{e\mathbf{B}}{m} \ , \tag{2.4}$$

it is possible to rewrite Equation 2.3 as

$$\frac{\mathrm{d}\mathbf{v}_\perp}{\mathrm{d}t} = (\mathbf{v}_\perp \times \boldsymbol{\omega}_c) \ . \tag{2.5}$$

The motion described by Equation 2.5 is a rotation, quantified by a constant angular frequency ω_c, which is known as the cyclotron (or gyro-) frequency. The combination of this rotation superimposed onto the constant velocity along the field line given by Equation 2.2 results in a helical charged particle trajectory which follows the field line. The radius of the circular gyration around the field line is known as the 'Larmor radius' or 'gyroradius' ρ_c and is calculated by integrating Equation 2.3. This is facilitated by considering the particle position with respect to the centre of the gyration, $\boldsymbol{\rho}_c$, defined in terms of the perpendicular velocity ($\mathbf{v}_\perp = \mathrm{d}\boldsymbol{\rho}_c/\mathrm{d}t$) as

$$\mathbf{v}_\perp = \boldsymbol{\rho}_c \times \boldsymbol{\omega}_c \ .$$

The Larmor radius is given by the magnitude of $\boldsymbol{\rho}_c$ and determined using

$$\rho_c = \frac{v_\perp}{\omega_c} = \frac{m v_\perp}{|e|B} \ .$$

Larmor radii for fast ions resulting from confined beam atoms in MAST can typically reach up to ∼0.15 m, representing a fraction of the minor radius $\rho_c/a \sim 1/5$. This is significantly larger than on other devices, and is due to the low magnetic field and tight aspect ratio of the ST.

2.1.1 Conserved Quantities

Charged particles moving in EM fields possess adiabatically invariant quantities, which remain almost constant during the motion of the particle. The requirements for these to remain approximately constant are that the the typical time scale of any changes to the system τ is long compared to the gyro-period $\tau_c = 2\pi/\omega_c$, and that the typical length scales of the system L are large compared to the Larmor radius,

$$\tau \gg \tau_c \ , \tag{2.6}$$

$$L \gg \rho_c \ . \tag{2.7}$$

Energy

The scalar product of the Lorentz force (Equation 2.1) with the particle velocity yields

$$\begin{aligned} m\frac{\mathrm{d}\mathbf{v}}{\mathrm{d}t}\cdot\mathbf{v} &= e\left(\mathbf{E}+\mathbf{v}\times\mathbf{B}\right)\cdot\mathbf{v} \\ \frac{\mathrm{d}}{\mathrm{d}t}\left(\frac{1}{2}mv^2\right) &= e\mathbf{E}\cdot\mathbf{v}. \end{aligned} \tag{2.8}$$

Since $\boldsymbol{\nabla}\times\mathbf{E}=0$ it is possible to express a static electric field in terms of the scalar potential Φ using $\mathbf{E}=-\nabla\Phi$. This allows Equation 2.8 to be rewritten as

$$\frac{\mathrm{d}}{\mathrm{d}t}\left(\frac{1}{2}mv^2\right) = -e\nabla\Phi\cdot\mathbf{v} = -e\frac{\mathrm{d}\Phi}{\mathrm{d}t}\ .$$

This can be rearranged to show that the sum of the kinetic and potential energy remain invariant in the presence of a static electromagnetic field,

$$\frac{\mathrm{d}}{\mathrm{d}t}\left(\frac{1}{2}mv^2+e\Phi\right)=0\ .$$

Magnetic Moment

The magnetic moment of the current loop associated with a helical charged particle trajectory is the product of the current through the loop I with the area of the loop A [62],

$$\mu = IA = \frac{e\omega_c}{2\pi}\pi\rho_c^2 = \frac{mv_\perp^2}{2B}\ . \tag{2.9}$$

In an inhomogeneous magnetic field, assuming that $\mathbf{B}$ is in the z-direction, the force on the guiding centre is

$$F_\parallel = m\frac{\mathrm{d}v_\parallel}{\mathrm{d}t} = -\mu\boldsymbol{\nabla}_\parallel\mathbf{B}\ , \tag{2.10}$$

where the adiabatic expansion of $\mathbf{B}$ around the guiding centre location of the particle is assumed. Multiplying Equation 2.10 by $v_\parallel = \mathrm{d}z/\mathrm{d}t$ gives

$$\frac{m}{2}\frac{\mathrm{d}v_\parallel^2}{\mathrm{d}t} = -\mu\frac{\partial B}{\mathrm{d}z}\frac{\mathrm{d}z}{\mathrm{d}t}\ . \tag{2.11}$$

The left hand side of this equation is the kinetic energy of the parallel motion $\mathcal{E}_\parallel$. In the timescales considered (Equation 2.6), B is considered to be constant in time

such that Equation 2.11 may be rewritten as

$$\frac{\mathrm{d}\mathcal{E}_{\parallel}}{\mathrm{d}t} = -\frac{\mathcal{E}_{\perp}}{B}\frac{\mathrm{d}B}{\mathrm{d}t} \ ,$$

which states that in a spatially varying but temporally stationary field, the moving particle sees a time-dependent field. The total kinetic energy of the particle is the sum of the components parallel and perpendicular to the field; $\mathcal{E} = \mathcal{E}_{\parallel} + \mathcal{E}_{\perp} =$ constant. This means that

$$\begin{aligned} \frac{\mathrm{d}\mathcal{E}_{\parallel}}{\mathrm{d}t} + \frac{\mathrm{d}\mathcal{E}_{\perp}}{\mathrm{d}t} &= 0 \\ \frac{\mathrm{d}\mathcal{E}_{\perp}}{\mathrm{d}t} &= \frac{\mathcal{E}_{\perp}}{B}\frac{\mathrm{d}B}{\mathrm{d}t} \ . \end{aligned} \tag{2.12}$$

Conversely, considering just the time variation of $\mathcal{E}_{\perp}$

$$\frac{\mathrm{d}\mathcal{E}_{\perp}}{\mathrm{d}t} = \frac{\mathrm{d}}{\mathrm{d}t}\left(\frac{\mathcal{E}_{\perp}}{B}B\right) = \frac{\mathcal{E}_{\perp}}{B}\frac{\mathrm{d}B}{\mathrm{d}t} + B\frac{\mathrm{d}}{\mathrm{d}t}\left(\frac{\mathcal{E}_{\perp}}{B}\right) \ .$$

When this is compared to Equation 2.12 we find

$$B\frac{\mathrm{d}}{\mathrm{d}t}\left(\frac{\mathcal{E}_{\perp}}{B}\right) = B\frac{\mathrm{d}}{\mathrm{d}t}\mu = 0$$

so that $\mu =$ constant is an adiabatic invariant.

2.1.2 $\mathbf{E} \times \mathbf{B}$ drift

If an electric field $\mathbf{E}$ perpendicular to the magnetic field $\mathbf{B}$ is included, charged particles will experience a drift to their motion perpendicular to both fields. It is independent of e, m and $\mathcal{E}$, so the whole plasma is subject to the drift. The gyro-averaged velocity of the drift in the absence of any other externally applied forces, $\mathbf{v}_{\mathbf{E}\times\mathbf{B}}$ is found by taking the cross product of the Lorentz force, Equation 2.1, with the magnetic field such that

$$\mathbf{v}_{\mathbf{E}\times\mathbf{B}} = \frac{\mathbf{E}\times\mathbf{B}}{B^2} \ .$$

2.1.3 The Mirror Force and ∇B drift

The parallel velocity of the particle is given by

$$v_{\parallel}^2 \ = \ v^2 - v_{\perp}^2 \ = \ v^2 - \frac{2\mu B}{m} \ .$$

When B becomes large, $v_\parallel^2$ goes to zero, before becoming negative. A negative $v_\parallel^2$ is not possible, so the parallel particle velocity changes direction, going back in the direction it came from. This effect is known as a 'magnetic mirror', and was used in several early confinement schemes [63]. The magnetic mirror force for an individual particle is given by

$$\mathbf{F}_\mathrm{m} = -\mu \boldsymbol{\nabla} \mathbf{B} \ .$$

In a tokamak the toroidal magnetic field varies as the inverse of the major radius, $\mathbf{B}_\zeta \sim 1/R$. This means that charged particles experience the mirror force as they move towards the HFS of the device, also experiencing a drift due to the gradient in the field known as the $\nabla \mathbf{B}$ drift. The magnitude of the drift can be found by putting $\mathbf{F}_\mathrm{m}$ into the equation for an external force,

$$\mathbf{v}_{\nabla \mathbf{B}} = \frac{\mathbf{F}_\mathrm{m} \times \mathbf{B}}{eB^2} = -\mathcal{E}_\perp \frac{\nabla \mathbf{B} \times \mathbf{B}}{eB^3} \ . \tag{2.13}$$

It can be seen from Equation 2.13 that the ∇B drift, unlike the $\mathbf{E} \times \mathbf{B}$ drift, is dependent upon the e, m and $\mathcal{E}$ of the particle. The cosine of the pitch angle of a particle λ can be used to determine whether or not it will experience a bounce point due to a magnetic mirror, where

$$\lambda = \cos(\theta_v) = \frac{v_\parallel}{v} \ . \tag{2.14}$$

Particles that experience the magnetic mirror effect in a tokamak and change direction are known as 'trapped' particles. Those particles for which $v_\parallel$ is sufficiently large do not experience a turning point, and are therefore referred to as 'passing' particles, completing full poloidal orbits.

For trapped particles, the turning point occurs at a point in the orbit where $v_\parallel = 0$, such that all of the velocity is in the perpendicular direction $v = v_\perp$. Conservation of $\mathcal{E}$ throughout the orbit means that at the point on the midplane of the tokamak where the particle experiences the minimum magnetic field in it's orbit, $B = B_\mathrm{min}$ has total velocity v_0 that equals the perpendicular velocity at the bounce point $v_{\perp,\mathrm{b}}$,

$$v_0^2 = v_{\perp,0}^2 + v_{\parallel,0}^2 = v_{\perp,\mathrm{b}}^2 = v_\mathrm{b}^2 \ .$$

Conversely, conservation of μ requires that the magnetic moment at the bounce point (where $B = B_b$) is equal to that on the midplane at the location of B_{min},

$$\frac{v_b^2}{B_b} = \frac{v_{\perp,0}^2}{B_\mathrm{min}} \ ,$$

hence

$$\frac{B_b}{B_{\min}} = 1 + \frac{v_{\parallel,0}^2}{v_{\perp,0}^2} \ .$$

2.1.4 Curvature Drift

Particles that follow curved field lines will experience a centripetal force which leads to a 'curvature drift' that is perpendicular to the vector from the centre of curvature to the particle location, $\mathbf{R}$ and the magnetic field. The curvature force $\mathbf{F}_{\rm c}$ is given by

$$\mathbf{F}_{\rm c} = -\frac{mv_{\parallel}^2}{R^2}\mathbf{R}$$

with a resulting drift velocity $\mathbf{v}_{\rm c}$ found (using the same technique as for the ∇B drift) as

$$\mathbf{v}_{\rm c} = \frac{\mathbf{F}_{\rm c} \times \mathbf{B}}{eB^2} = \frac{mv_{\parallel}^2}{eB^2R^2}\mathbf{R} \times \mathbf{B} \ .$$

2.2 Magnetohydrodynamics

When faced with the challenge of determining plasma equilibrium and stability, the long wavelength, low frequency, macroscopic behaviour of the plasma can be modelled by means of a single perfectly conducting fluid immersed in a magnetic field. For a given geometry, the way in which the inertial, magnetic and pressure forces interact within the plasma are described by by what is known as the MHD model. This is valid for plasma phenomena with length scales greater than the Debye length λ_D. The Debye length represents a sphere around the particle, beyond which charges are screened. It is given by [64]

$$\lambda_D = \sqrt{\frac{\epsilon_0 k_B T_e}{n_e e^2}} \ ,$$

where T_e, n_e and e are the electron temperature, density and charge respectively, ϵ_0 is the permittivity of free space and k_B is the Boltzmann constant. The additional assumptions

$$\begin{aligned} v &< c \\ L_\perp &\ll \rho_c \\ L_\parallel &\ll L_{\rm mfp} \\ \tau &\gg t_c \end{aligned}$$

are also required, where c is the speed of light, $L_\perp$ and $L_\parallel$ are the perpendicular and parallel length scales, L_{mfp} is the mean free path of a particle, τ is the timescale of changes in the system and t_c is the typical collision time. The plasma may be considered quasi-neutral, i.e.

$$n_e = Z n_i$$

where n_i is the ion density and Z is the atomic number.

2.2.1 Ideal MHD

Treating the plasma as a perfect conductor in which the resistivity is zero $\eta = 0$, a simplification of MHD can be made, referred to as 'ideal' MHD. Under these considerations, the ideal MHD model is governed by a set of equations that may be written as [62]

$$\frac{\partial \rho}{\partial t} + \rho \boldsymbol{\nabla} \cdot \mathbf{v} = 0 \quad \text{Mass Continuity,} \tag{2.15}$$

$$\frac{\partial P}{\partial t} + \mathbf{v} \cdot \boldsymbol{\nabla} P + \gamma_c P \boldsymbol{\nabla} \cdot \mathbf{v} = 0 \quad \text{Adiabatic Equation of State,} \tag{2.16}$$

$$\rho \frac{\partial \mathbf{v}}{\partial t} + \rho \mathbf{v} \cdot \boldsymbol{\nabla} \mathbf{v} + \boldsymbol{\nabla} P - \mathbf{j} \times \mathbf{B} = 0 \quad \text{Momentum Equation,} \tag{2.17}$$

$$\boldsymbol{\nabla} \times \mathbf{B} - \mu_0 \mathbf{j} = 0 \quad \text{Ampère's Law,} \tag{2.18}$$

$$\frac{\partial \mathbf{B}}{\partial t} + \boldsymbol{\nabla} \times \mathbf{E} = 0 \quad \text{Faraday's Law,} \tag{2.19}$$

$$\boldsymbol{\nabla} \cdot \mathbf{B} = 0 \quad \text{No Magnetic Monopoles,} \tag{2.20}$$

$$\mathbf{E} + \mathbf{v} \times \mathbf{B} = 0 \quad \text{Ohm's Law,} \tag{2.21}$$

where the convective derivative

$$\frac{\mathrm{d}}{\mathrm{d}t} = \frac{\partial}{\partial t} + \mathbf{v} \cdot \boldsymbol{\nabla}$$

has been assumed and ρ is the plasma mass density, $\mathbf{v}$ is the plasma velocity, P is the plasma pressure, $\mathbf{j}$ is the current density, γ_c is the ratio of specific heats and μ_0 is the permeability of free space. $\mathbf{B}$ and $\mathbf{E}$ represent the magnetic and electric fields, which consist of the externally applied field plus the averaged internal fields arising from inter-particle interactions. The ideal MHD model of a plasma requires that the motion of the plasma is both spatially and temporally linked to the magnetic field configuration. This is known as the 'frozen in' condition.

2.2.2 Linearised MHD

Equations 2.15 to 2.19 provide a nonlinear ideal MHD model of the plasma. In order to model waves and instabilities in the plasma, it is instructive to linearise this set of equations. The linearisation is justified by considering the bulk plasma to be stationary and unperturbed by the instability, which is modelled by a small, time dependent perturbation to the plasma. Each quantity in the ideal MHD equations is replaced by a time-independent equilibrium term $Q_0(\mathbf{r})$ and a time-dependent Eulerian perturbation $\tilde{Q}(\mathbf{r}, t)$,

$$Q(\mathbf{r}, t) = Q_0(\mathbf{r}) + \tilde{Q}(\mathbf{r}, t) \ . \tag{2.22}$$

Linearisation requires that the perturbation remains small, $|\tilde{Q}|/|Q_0| \ll 1$. Assuming this, along with a stationary equilibrium plasma ($\mathbf{v} = 0$) at $t = 0$, the linearised equations are found:

$$\frac{\partial \tilde{\rho}}{\partial t} + \boldsymbol{\nabla} \cdot (\rho_0 \tilde{\mathbf{v}}) = 0 \quad \text{Mass Continuity,} \tag{2.23}$$

$$\frac{\partial \tilde{P}}{\partial t} + \tilde{\mathbf{v}} \cdot \boldsymbol{\nabla} P_0 + \gamma_c P_0 \boldsymbol{\nabla} \cdot \tilde{\mathbf{v}} = 0 \quad \text{Adiabatic Equation of State,} \tag{2.24}$$

$$\rho_0 \frac{\partial \tilde{\mathbf{v}}}{\partial t} + \boldsymbol{\nabla} \tilde{P} - \tilde{\mathbf{j}} \times \mathbf{B}_0 - \mathbf{j}_0 \times \tilde{\mathbf{B}} = 0 \quad \text{Momentum Equation,} \tag{2.25}$$

$$\boldsymbol{\nabla} \times \tilde{\mathbf{B}} - \mu_0 \tilde{\mathbf{j}} = 0 \quad \text{Ampère's Law,} \tag{2.26}$$

$$\frac{\partial \tilde{\mathbf{B}}}{\partial t} + \boldsymbol{\nabla} \times \tilde{\mathbf{E}} = 0 \quad \text{Faraday's Law,} \tag{2.27}$$

$$\boldsymbol{\nabla} \cdot \tilde{\mathbf{B}} = 0 \quad \text{No Magnetic Monopoles,} \tag{2.28}$$

$$\tilde{\mathbf{E}} + \tilde{\mathbf{v}} \times \mathbf{B}_0 = 0 \quad \text{Ohm's Law.} \tag{2.29}$$

The velocity of the plasma perturbation $\tilde{\mathbf{v}}$ is the rate of change of the displacement $\boldsymbol{\xi}$, defined as

$$\tilde{\mathbf{v}} = \frac{\partial \boldsymbol{\xi}}{\partial t} \ ; \tag{2.30}$$

i.e. $\boldsymbol{\xi}$ is the displacement of a fluid element from its equilibrium position $\mathbf{r}_0$

$$\mathbf{r} = \mathbf{r}_0 + \boldsymbol{\xi}(r_0, t) \ .$$

By eliminating $\tilde{j}$ and $\tilde{E}$ from the linearised ideal MHD equations (Equations 2.23 - Equation 2.29), a reduced trio of equations is obtained.

$$\rho_0 \frac{\partial^2 \boldsymbol{\xi}}{\partial t^2} + \boldsymbol{\nabla}\tilde{P} + \frac{1}{\mu_0}\left[\tilde{\mathbf{B}} \times (\boldsymbol{\nabla} \times \mathbf{B}_0) + \mathbf{B}_0 \times \left(\boldsymbol{\nabla} \times \tilde{\mathbf{B}}\right)\right] = 0 \,, \tag{2.31}$$

$$\tilde{P} + \boldsymbol{\xi} \cdot \boldsymbol{\nabla} P_0 + \gamma_c P_0 \boldsymbol{\nabla} \cdot \boldsymbol{\xi} = 0 \,, \tag{2.32}$$

$$\tilde{\mathbf{B}} + \boldsymbol{\nabla} \times (\mathbf{B_0} \times \boldsymbol{\xi}) = 0 \,. \tag{2.33}$$

Equation 2.31 is the linearised momentum equation, which balances the inertial force (first term), pressure force (second term) and magnetic force (third term). From the linearised momentum equation, the force-operator $\mathbf{F}(\boldsymbol{\xi})$ is defined using the following equation,

$$\rho_0 \frac{\partial^2 \boldsymbol{\xi}}{\partial t^2} = \mathbf{F}(\boldsymbol{\xi}) \tag{2.34}$$

which is found by using Equations 2.32 and 2.33 to eliminate $\tilde{P}$ and $\tilde{\mathbf{B}}$ from the linearised momentum equation,

$$\begin{aligned} \mathbf{F}(\boldsymbol{\xi}) &= \rho_0 \frac{\partial^2 \boldsymbol{\xi}}{\partial t^2} \\ &= \boldsymbol{\nabla}\left(\boldsymbol{\xi} \cdot \boldsymbol{\nabla} P_0 + \gamma_c P_0 \boldsymbol{\nabla} \cdot \boldsymbol{\xi}\right) \\ &\quad + \frac{1}{\mu_0}\left[(\boldsymbol{\nabla} \times \mathbf{B}_0) \times (\boldsymbol{\nabla} \times (\boldsymbol{\xi} \times \mathbf{B_0})) + (\boldsymbol{\nabla} \times \boldsymbol{\nabla} \times (\boldsymbol{\xi} \times \mathbf{B_0})) \times \mathbf{B}_0\right]. \end{aligned}$$

2.2.3 Normal Mode Formulation

By reformulating Equation 2.34 as a normal mode problem, the linear stability problem becomes more amenable to analysis. This is done by treating the perturbation of each quantity ($\tilde{Q}(\mathbf{r}, t)$ in Equation 2.22) as the product of a spatial displacement and an oscillatory time dependant part,

$$\tilde{Q}(\mathbf{r}, t) = \tilde{Q}(\mathbf{r})\ \mathrm{e}^{-i\omega t} \,.$$

Applying this formulation to Equation 2.34, the force operator equation can now be written

$$-\omega^2 \boldsymbol{\xi} = \frac{1}{\rho_0}\mathbf{F}(\boldsymbol{\xi}) \,. \tag{2.35}$$

The normal-mode formulation above allows the generalised MHD stability to be solved in three dimensional equilibria. By applying appropriate boundary conditions to $\boldsymbol{\xi}$ it becomes an eigenvalue problem, with eigenvalue ω^2.

2.2.4 Self-Adjointness of F

A mathematical property which is of great significance to stability analysis of linearised ideal MHD is that the force operator $\mathbf{F}(\boldsymbol{\xi})$ is self-adjoint. This is the case for an operator whose matrix is Hermitian (a Hermitian matrix is equal to its own conjugate transpose). For two independent displacement vectors $\boldsymbol{\xi}_1$ and $\boldsymbol{\xi}_2$ a self-adjoint, Hermitian operator satisfies

$$\frac{1}{2}\int \rho_0 \, \boldsymbol{\xi}_1^* \cdot \mathbf{F}(\boldsymbol{\xi}_2) \, \mathrm{d}^3x = \frac{1}{2}\int \rho_0 \, \boldsymbol{\xi}_2^* \cdot \mathbf{F}(\boldsymbol{\xi}_1) \, \mathrm{d}^3x \ ,$$

where the integration is over all space. The consequence of this for the force operator is that any eigenvalue ω^2 is purely real. A normal mode with $\omega^2 > 0$ represents a pure oscillation, and is considered to be stable. A mode with $\omega^2 < 0$ however has a branch which grows exponentially and thus corresponds to an ideal linear MHD instability. The stability threshold is therefore at $\omega = 0$; crossing this boundary defines the point at which a mode becomes linearly unstable. This is shown in Figure 2.1.

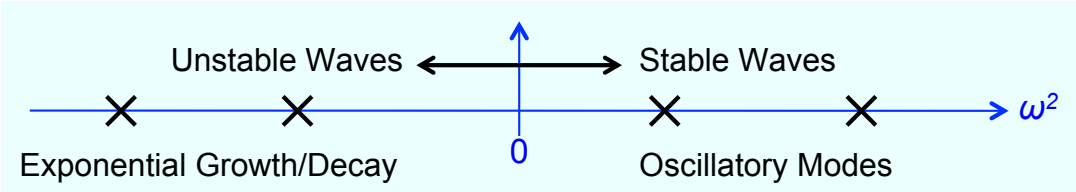

Figure 2.1: Ideal MHD ω^2 spectrum of frequency eigenvalues. Adapted from [65].

The spectrum of the operator $\frac{1}{\rho_0}\mathbf{F}$ considered in the ω-plane is confined to the real and imaginary axes. By introducing an EP population it is possible to perturb the stable eigenvalues of the system, causing weakly growing or decaying oscillatory modes as depicted in Figure 2.2. In addition to perturbing modes already present in the plasma, causing them to grow (for example that shown by the red arrow in the figure), an independent set of modes referred to as EPMs exists. These are purely due to the EP population, and in its absence would not manifest themselves.

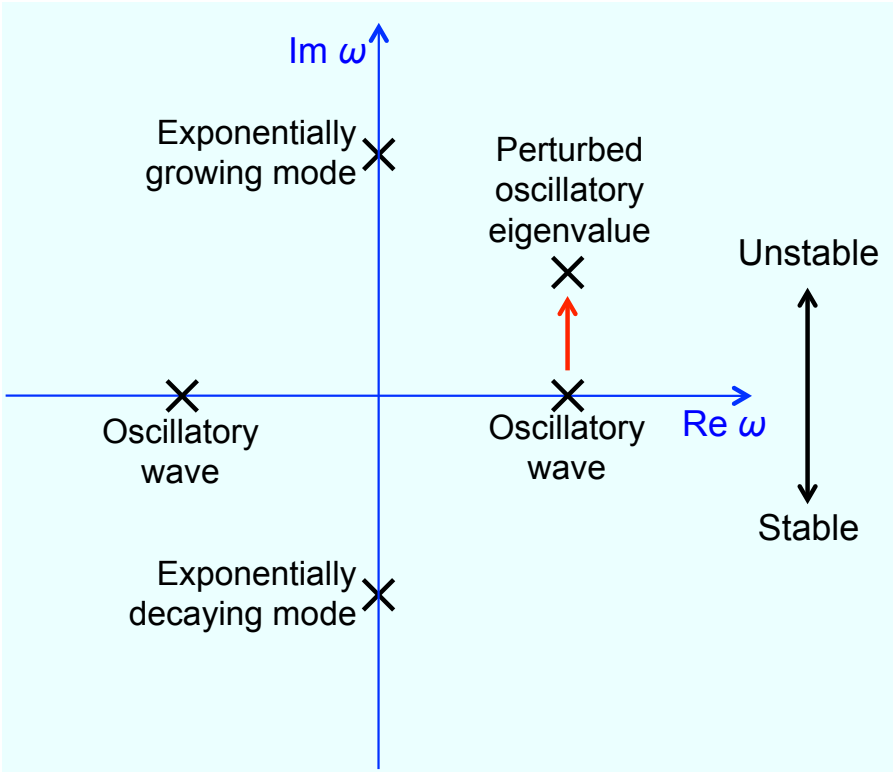

Figure 2.2: Ideal MHD ω^2 spectrum of frequency eigenvalues in the presence of an EP population. The fast ions produce the perturbation shown by the red arrow, resulting in an oscillatory wave that is weakly growing. Adapted from [65].

2.3 Tokamak Equilibria

In order to study instabilities in a tokamak plasma, it is necessary to begin with a toroidal plasma in equilibrium. Although MAST discharges typically last for less than one second, periods of relative stability are reached on timescales given by Equation 2.6 whereby the system is considered to be in equilibrium. The equilibrium is governed by two main aspects: the force balance between the magnetic pressure and the plasma pressure; and the position and shaping of the plasma which is controlled by currents in specific coils. As explained in Section 1.3, the primary field is the toroidal field B_ζ which is created by driving a poloidal current I_p through the plasma. The toroidal field varies roughly as $B_\zeta \sim 1/R$ such that the edge of the plasma near the central solenoid is referred to as the HFS, and the outer edge as the Low Field Side (LFS). For a tokamak with scalar pressure, the gradient in the pressure is balanced by the Lorentz force, which can be found for a stationary plasma by setting $\mathbf{v} = 0$ in Equation 2.17

$$\mathbf{j} \times \mathbf{B} = \boldsymbol{\nabla} P \ . \tag{2.36}$$

2.3.1 Flux Functions

To simplify the study of tokamak equilibria is is intuitive to introduce various so-called 'flux functions'. In an axisymmetric (independent of ζ) equilibrium, magnetic field lines lie on nested flux surfaces. This becomes apparent when the scalar product of the magnetic field is taken with Equation 2.36, $\mathbf{B} \cdot \boldsymbol{\nabla} P = 0$. The magnetic field $\mathbf{B}$ varies along a field line as it wraps around on a flux surface, as shown in Figure 1.3 (it is this variation that is responsible for particle trapping), hence the pressure must be constant on a flux surface. The same process can be applied to show that $\mathbf{j} \cdot \boldsymbol{\nabla} P = 0$ and hence the current density is also constant on a flux surface.

The poloidal flux is given by

$$\psi_p(R, z) = \int \mathbf{B} \cdot \mathrm{d}\mathbf{s} \ , \tag{2.37}$$

where the surface integral is over a flux surface. The poloidal flux is also a flux function, so $\mathbf{B} \cdot \nabla \psi_p = 0$. For this reason, the poloidal flux is used as a radial coordinate within this cylindrical coordinate system. Writing the magnetic field in Equation 2.37 in terms the the vector potential $\mathbf{A}$, and applying Stoke's theorem

$$\psi_p = \int (\boldsymbol{\nabla} \times \mathbf{A}) \cdot \mathrm{d}\mathbf{s} = \oint \mathbf{A} \cdot \mathrm{d}l,$$

the toroidal vector potential is

$$A_\zeta = \frac{\psi_p(R,z)}{R},$$

so the R and z components of the magnetic field can be written

$$\begin{aligned} B_R &= (\boldsymbol{\nabla}\times\mathbf{A})_R \\ &= -\frac{1}{R}\frac{\partial\psi_p(R,z)}{\partial z}\ , \end{aligned} \qquad\qquad \begin{aligned} B_z &= (\boldsymbol{\nabla}\times\mathbf{A})_z \\ &= \frac{1}{R}\frac{\partial\psi_p(R,z)}{\partial R}\ . \end{aligned}$$

Using Equation 2.20,

$$\boldsymbol{\nabla}\cdot\mathbf{B} = 0 = \frac{1}{R}\frac{\partial}{\partial R}\left(RB_R\right) + \frac{\partial B_z}{\partial z}\ .$$

In the same way that a magnetic field flux function exists, there is a current density flux function. The current flux function F is related to the poloidal current density

$$j_R = -\frac{1}{R}\frac{\partial F}{\partial z} \qquad (2.38) \qquad\qquad j_z = \frac{1}{R}\frac{\partial F}{\partial R}\ . \qquad (2.39)$$

From Ampére's law (Equation 2.18),

$$j_R = -\frac{1}{\mu_0}\frac{\partial B_\zeta}{\partial z} \qquad (2.40) \qquad\qquad j_z = \frac{1}{\mu_0}\frac{1}{R}\frac{\partial}{\partial R}\left(RB_\zeta\right)\ . \qquad (2.41)$$

Via a comparison between Equations 2.38 and 2.40 as well as 2.39 and 2.41, the relationship between the current flux function and the toroidal field found to be

$$F = \frac{RB_\zeta}{\mu_0}\ . \qquad (2.42)$$

By substituting Equations 2.38 and 2.40 into $\mathbf{j}\cdot\boldsymbol{\nabla}P = 0$,

$$\begin{aligned} \frac{\partial F}{\partial R}\frac{\partial P}{\partial z} - \frac{\partial F}{\partial z}\frac{\partial P}{\partial R} &= 0 \\ \boldsymbol{\nabla}F\times\boldsymbol{\nabla}P &= 0\ . \end{aligned}$$

Since F is a function of P, and P is itself a flux function, it is necessary for F to also be a flux function,

$$F = F(\psi_p)\ .$$

2.3.2 Grad-Shafranov Equation

An axisymmetric tokamak equilibrium written in terms of a differential equation of the poloidal flux ψ_p may be constructed as a function of the pressure $P(\psi_p)$ and current density flux function $F(\psi_p)$. To find the equation, one must start by writing the force balance equation in the form

$$\mathbf{j}_\theta \times B_\zeta \mathbf{e}_\zeta + j_\zeta \mathbf{e}_\zeta \times \mathbf{B}_\theta = \boldsymbol{\nabla} P \ , \tag{2.43}$$

where $\mathbf{j}_\theta$ is the poloidal current density, $\mathbf{B}_\theta$ is the poloidal magnetic field and $\mathbf{e}_\zeta$ is a unit vector in the toroidal coordinate direction. These quantities can be written in terms of the poloidal flux function ψ_p,

$$\begin{aligned} \mathbf{B}_\theta &= \frac{1}{R}\left(\boldsymbol{\nabla}\psi_p \times \mathbf{e}_\zeta\right) \ , \\ \mathbf{j}_\theta &= \frac{1}{R}\left(\boldsymbol{\nabla} F \times \mathbf{e}_\zeta\right) \ . \end{aligned}$$

Substituting these into Equation 2.43 gives

$$\frac{1}{R}\left(\boldsymbol{\nabla} F \times \mathbf{e}_\zeta\right) \times \mathbf{e}_\zeta B_\zeta + j_\zeta \mathbf{e}_\zeta \times \frac{1}{R}\left(\boldsymbol{\nabla}\psi_p \times \mathbf{e}_\zeta\right) \ .$$

Since flux functions are (by definition) constant on a flux surface, one notes that $\mathbf{e}_\zeta \cdot \boldsymbol{\nabla}\psi_p = \mathbf{e}_\zeta \cdot \boldsymbol{\nabla} F = 0$ such that this can be rewritten as

$$-\frac{B_\zeta}{R}\boldsymbol{\nabla} F + \frac{j_\zeta}{R}\boldsymbol{\nabla}\psi_p = \boldsymbol{\nabla} P \ . \tag{2.44}$$

Since we know that

$$\boldsymbol{\nabla} F(\psi_p) = \frac{\mathrm{d}F}{\mathrm{d}\psi_p}\boldsymbol{\nabla}\psi_p \qquad\qquad \boldsymbol{\nabla} P(\psi_p) = \frac{\mathrm{d}P}{\mathrm{d}\psi_p}\boldsymbol{\nabla}\psi_p \ ,$$

these can be substituted into Equation 2.44 to give

$$j_\zeta = R\frac{\mathrm{d}P}{\mathrm{d}\psi_p} + B_\zeta \frac{\mathrm{d}F}{\mathrm{d}\psi_p} \ .$$

By replacing the toroidal magnetic field using Equation 2.42, this may be written as

$$j_\zeta = RP' + \frac{\mu_0}{R}FF' \ . \tag{2.45}$$

The final step required is to rewrite j_ζ in Equation 2.45 as a flux function (in terms

of ψ_p). This is done by writing Ampère's law (Equation 2.18) in the form

$$-\mu_0 R j_\zeta = R\frac{\partial}{\partial R}\frac{1}{R}\frac{\partial \psi_p}{\partial R} + \frac{\partial^2 \psi_p}{\partial z^2} \ , \tag{2.46}$$

such that substituting Equation 2.46 into Equation 2.45 yields the equation required to find the tokamak equilibrium. Known as the 'Grad-Shafranov Equation' [66, 67], it is most commonly written in the form [16]

$$R\frac{\partial}{\partial R}\frac{1}{R}\frac{\partial \psi_p}{\partial R} + \frac{\partial^2 \psi_p}{\partial z^2} = -\mu_0 R^2 P' - \mu_0^2 F F' \ . \tag{2.47}$$

For plasma simulations, the tokamak equilibrium is calculated using Equation 2.47 by determining a balance between P' and FF'.

2.4 Important Tokamak Quantities

Poloidal and Toroidal Mode Numbers

For a toroidal device, so-called 'mode numbers' can be introduced in order to specify poloidal m and toroidal n transits of the magnetic field lines. These can, for example, be used to specify 'kink' instabilities. Kink modes are displacements to the equilibrium magnetic field structure. Examples of greatly exaggerated amplitude are shown in Figure 2.3.

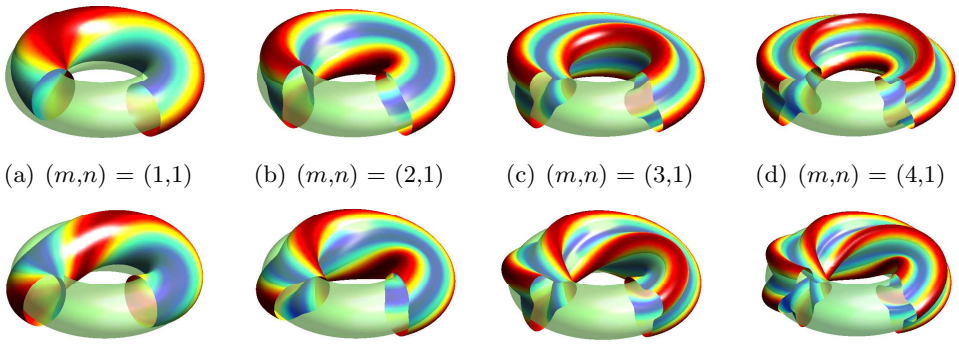

(a) $(m,n) = (1,1)$ (b) $(m,n) = (2,1)$ (c) $(m,n) = (3,1)$ (d) $(m,n) = (4,1)$

(e) $(m,n) = (1,2)$ (f) $(m,n) = (2,2)$ (g) $(m,n) = (3,3)$ (h) $(m,n) = (4,4)$

Figure 2.3: Examples flux surface perturbations due to kink modes. The unperturbed flux surface is shown by the semitransparent green surface, and the perturbed surface inwards is blue and outwards is red.

Safety Factor & Magnetic Shear

The safety factor q of a field line is defined as the number of toroidal rotations per poloidal rotation. A field line will return to the toroidal location ζ after a change in the toroidal angle $\Delta\zeta$ such that the q value for that field line is defined as [16]

$$q = \frac{\Delta\zeta}{2\pi} \ .$$

It is called the safety factor due to the role it plays in plasma stability; a high safety factor means that the toroidal field dominates and instabilities such as kink modes tend to be stabilised. So-called 'rational surfaces' occur on field lines where

$$m = nq \ , \tag{2.48}$$

upon which the field line joins up on itself. These surfaces are more susceptible to instabilities as the periodic perturbations join up on themselves. Subsequently, for plasmas whereby the the minimum safety factor is above unity $q_{\min} > 1$ are resilient to the dominant $n = 1$, $m = 1$ kink modes. A general form of the safety factor is given by

$$q = \frac{1}{2\pi} \oint \frac{1}{R} \frac{B_\zeta}{B_\theta} \, \mathrm{d}s = \frac{\mathrm{d}\psi_t}{\mathrm{d}\psi_p} \ ,$$

where the integral is over a poloidal circuit of the flux surface and ψ_t and ψ_p are the toroidal and poloidal flux functions respectively.

Due to poloidal and toroidal variations in the magnetic field, the safety factor varies radially in a tokamak equilibrium. This results in what is referred to as a 'q-profile' in the plasma, where the magnetic field lines are more tightly twisted in the core of the plasma than near the edge, as depicted in Figure 1.3. The gradient in the q-profile is known as the magnetic shear S, high values of which have a stabilising effect. The surface-averaged value of the magnetic shear is given by [16]

$$S = \frac{r}{q} \frac{\mathrm{d}q}{\mathrm{d}r} \ .$$

In a tokamak, the minimum in the q-profile does not always lie at the magnetic axis, which can lead to what is referred to as 'reversed-shear' within a core-localised region.

Plasma β

How efficiently the plasma pressure P is confined by the magnetic field is given by the ratio of the two, known as the 'plasma β' [16]

$$\beta = \frac{P}{B^2/2\mu_0} \ .$$

Often quoted is the poloidal β, given by [16]

$$\beta_p = \frac{\int P \ \mathrm{d}X / \int \mathrm{d}X}{B_a^2/2\mu_0} \ ,$$

where the integrals are over the poloidal cross section, $B_a = \mu_0 I/l$ and l is the poloidal perimeter of the plasma.

2.5 Coordinate Systems

To model wave particle interactions in a tokamak plasma, it is important to work within a suitable coordinate system that both adequately describes the system and most simply defines it within the tokamak geometry. A generalised set of 'magnetic flux coordinates' does this, whereby three coordinates (ψ, ζ, θ) describe the radial location and the toroidal and poloidal angles respectively. For a tokamak with scalar pressure, the gradient in the pressure is balanced by the Lorentz force, Equation 2.36. The result of this is that $\mathbf{j}$ and $\mathbf{B}$ reside on surfaces of constant pressure. With the pressure highest along the magnetic axis of the device, these make up concentric 'nested' magnetic surfaces. Magnetic field lines lie on these surfaces, and since the poloidal flux on the surface is constant these are referred to as 'magnetic flux surfaces' (shown by the grey surfaces in Figure 1.3). The so-called magnetic flux coordinates mean that the radial coordinate ψ is constant on a flux surface, and the location on this surface is defined by a grid of θ and ζ which between them make up a curvilinear coordinate system.

Within this curvilinear coordinate system, the choice of θ and ζ is somewhat arbitrary. Provided they make up a complete circuit of the torus toroidally and poloidally, a choice can be made between orthogonal coordinates and coordinates in which on each flux surface the magnetic field $\mathbf{B}$ appears as a straight line. The second of these, referred to as 'straight field line' coordinates, is achievable through a deformation of the magnetic field lines via a suitable coordinate transform $(\psi, \zeta, \theta) \rightarrow (\psi, \zeta_{\mathrm{new}}, \theta_{\mathrm{new}})$. This straight field line representation results in the poloidal and toroidal angles related via the safety factor, which is itself a flux

function (i.e. constant on a flux surface, $q = q(\psi)$).

$$\zeta - q(\psi)\theta = \text{constant} , \qquad \psi = \text{constant} .$$

2.5.1 Boozer Coordinates

In 1981, Boozer introduced a coordinate system [68] in which the choice of poloidal and toroidal coordinates is made such that the periodic part of the electric scalar potential in the covariant representation of the magnetic field is zero $\Phi = 0$, providing a simple form for the Jacobian [69]. It is a dual covariant and contravariant representation, where the magnetic field $\mathbf{B}$ is shown in Equations 2.49 and 2.50 respectively in terms of the poloidal magnetic field $I(\psi_p)$ and the toroidal magnetic field $g(\psi_p)$.

$$\begin{aligned} \text{Covariant From: } \mathbf{B} &= B_{\psi_p}\boldsymbol{\nabla}\psi_p + B_\theta\boldsymbol{\nabla}\theta + B_\zeta\boldsymbol{\nabla}\zeta \\ &= \delta(\psi_p,\theta)\boldsymbol{\nabla}\psi_p + I(\psi_p)\boldsymbol{\nabla}\theta + g(\psi_p)\boldsymbol{\nabla}\zeta \qquad (2.49) \\ \text{Contravariant Form: } \mathbf{B} &= \boldsymbol{\nabla}\psi_t \times \boldsymbol{\nabla}\theta + \boldsymbol{\nabla}\zeta \times \boldsymbol{\nabla}\psi_p \\ &= \boldsymbol{\nabla}\left(\zeta - q\theta\right) \times \boldsymbol{\nabla}\psi_p \qquad (2.50) \end{aligned}$$

where

$$\begin{aligned} \delta(\psi_p,\theta) &= -\frac{I\boldsymbol{\nabla}\theta\cdot\boldsymbol{\nabla}\psi_p + g\boldsymbol{\nabla}\zeta\cdot\boldsymbol{\nabla}\psi_p}{\left|\boldsymbol{\nabla}\psi_p\right|^2} \\ &= -\frac{I\mathrm{g}^{12} + g\mathrm{g}^{13}}{\mathrm{g}^{11}} . \end{aligned}$$

Here, g^{ij} is used to represent the contravariant components of the metric tensor $\mathbf{g}$. In this system the angular field components in the θ and ζ directions are flux functions, $B_\zeta = B_\zeta(\psi_p) \equiv g(\psi_p)$ and $B_\theta = B_\theta(\psi_p) = \mathcal{J}B^2 - q(\psi_p)g(\psi_p) \equiv I(\psi_p)$ is ensured via the Jacobian, given by

$$\mathcal{J} = \frac{1}{\boldsymbol{\nabla}\psi_p\cdot\boldsymbol{\nabla}\theta\times\boldsymbol{\nabla}\zeta} = \frac{I+qg}{B^2} . \qquad (2.51)$$

The safety factor is the ratio of the contravariant components of $\mathbf{B}$,

$$q(\psi_p) = \frac{B^\zeta}{B^\theta} = \frac{\mathbf{B}\cdot\boldsymbol{\nabla}\zeta}{\mathbf{B}\cdot\boldsymbol{\nabla}\theta} = \frac{\mathrm{d}\psi_t}{\mathrm{d}\psi_p}$$

so this ratio is constant on a flux surface. The values ψ_t and ψ_p are the toroidal and poloidal magnetic flux respectively, and since these are flux functions either may be

used as the radial coordinate. In this thesis, the radial coordinate is chosen to be ψ_p.

2.6 Guiding Centre Motion

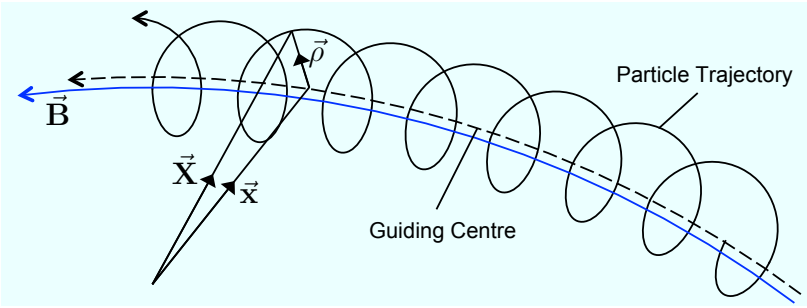

Figure 2.4: Guiding centre of helical particle trajectory.

Due to the large nature of the ∇B and curvature drifts of the fast ions (especially prominent in a ST), they cannot be fully represented by the MHD approach. An alternative approach is available, whereby a gyro-averaging procedure is used to follow the centre of the gyrating fast ion orbits. This is known as the 'guiding centre' approximation, and reduces the phase space of the problem. The equations of motion to describe the guiding centre drifts were first set out by Alfén in 1940 [70].

In Section 2.1 it was shown that due to the Lorentz force the particles gyrate in a helical trajectory about the guiding centre with a radius equal to the Larmor radius ρ_c. The approximation is valid provided any field inhomogeneities are smaller than ρ and any characteristic field frequencies are smaller than ω_c. The position of the guiding centre $\mathbf{x}$ is defined as

$$\mathbf{x} = \mathbf{X} - \boldsymbol{\rho}_c \ ,$$

where $\mathbf{X}$ is the actual location of the particle. The guiding centre of a particle orbit is shown in Figure 2.4. This approximation is important as the guiding centre position evolves slower than the full orbit position, so solving the equations becomes computationally more tractable when studying a large ensemble of particles.

2.6.1 Guiding Centre Equations of Motion

The dynamics of charged particle motion in magnetic fields can be represented in a more tractable form by using the guiding centre approximation, and in so doing

lower the number of system variables that must be evolved. This is done using a Lagrangian approach to determine the equations of motion that govern the system.

Using canonical variables for the generalised position $\mathbf{q}(t)$, velocity $\dot{\mathbf{q}}(t)$ and time t the exact particle Lagrangian for a particle of mass m and charge e in a stationary reference frame is

$$\mathcal{L}(\mathbf{q}, \dot{\mathbf{q}}, t) = \frac{1}{2} m \left|\dot{\mathbf{q}}\right|^2 + e\mathbf{A}(\mathbf{q}, t) \cdot \dot{\mathbf{q}} - e\Phi(\mathbf{q}, t) \ , \tag{2.52}$$

where $\mathbf{A}$ and Φ are the vector and scalar potential respectively in this frame. The general form of the Hamiltonian can be defined from the Lagrangian using the Legendre transformation [71]

$$\mathcal{H}(\mathbf{p}, \mathbf{q}, t) = \mathbf{p} \cdot \dot{\mathbf{q}} - \mathcal{L}(\mathbf{q}, \dot{\mathbf{q}}, t) \ ,$$

which is written in terms of the generalised momentum, defined as the 'canonical momentum' $\mathbf{p}$ rather than $\dot{\mathbf{q}}$, calculated from the Lagrangian (Equation 2.52) as

$$\mathbf{p} = \frac{\partial \mathcal{L}}{\partial \dot{\mathbf{q}}} = m\dot{\mathbf{q}} + e\mathbf{A}(\mathbf{q}, t) \ .$$

The Hamiltonian can now be written as

$$\begin{aligned} \mathcal{H}(\mathbf{p}, \mathbf{q}, t) &= \frac{1}{2} m \left|\dot{\mathbf{q}}\right|^2 + e\Phi(\mathbf{q}, t) \\ &= \frac{1}{2m} \left[\mathbf{p} - e\mathbf{A}(\mathbf{q}, t)\right]^2 + e\Phi(\mathbf{q}, t) \ . \end{aligned}$$

By finding a Lagrangian $\mathcal{L}$ for which the subsequent Euler-Lagrange equations (found by applying the variational principle given by Equation 2.53), Littlejohn found a set of canonical variables to define the guiding centre equations of motion [72].

$$\delta \int_{t_1}^{t_2} \mathcal{L} \ \mathrm{d}t = 0 \tag{2.53}$$

The guiding centre Lagrangian that was found can be written as [72]

$$\mathcal{L} = e\mathbf{A}^* \cdot \dot{\mathbf{x}} + \frac{m}{e} \mu \dot{\xi} - \mathcal{H} \ . \tag{2.54}$$

Here, $\dot{\mathbf{x}} = \mathrm{d}\mathbf{x}/\mathrm{d}t$ is the velocity of the guiding centre, ξ is the gyro-phase and $\mathbf{A}^* = \mathbf{A} + \rho_{\|}\mathbf{B}$ is the 'modified vector potential', where $\rho_{\|} = v_{\|}/\omega_c$ is the projection of the gyroradius in the parallel direction, known as the 'parallel gyroradius'. The gyro-averaged Hamiltonian is given by

$$\mathcal{H} = \frac{1}{2} m v_{\parallel}^2 + \mu B + e\Phi \ .$$

Next, canonical coordinates must be identified. To facilitate this, the Lagrangian must be re-written in the form

$$\mathcal{L} = \sum_i p_i \dot{q}_i - \mathcal{H} \ ,$$

which is done by substituting in the covariant form of $\mathbf{B}$ (Equation 2.49) and the vector potential from $\mathbf{B} = \boldsymbol{\nabla} \times \mathbf{A} = \boldsymbol{\nabla} \times (\psi_t \boldsymbol{\nabla}\theta - \psi_p \boldsymbol{\nabla}\zeta)$ into Equation 2.54,

$$\mathcal{L} = \left(\rho_{\parallel} I + \psi_t\right) \dot{\theta} + \left(\rho_{\parallel} g - \psi_p\right) \dot{\zeta} + \mu \dot{\xi} - \mathcal{H} + \delta \rho_{\parallel} \dot{\psi_p} \ . \tag{2.55}$$

where we have transformed into a set of normalised units in which $e = m = 1$.

Using the Boozer coordinate system explained in Section 2.5.1 to form the canonical coordinates, it is possible to read the conjugate variables from this equation, apart from the final term. A guiding centre modification can be made to correct for this. By altering the second order guiding centre velocity $\mathbf{v} \to \mathbf{v} + \mathbf{w}$, a transformation is made to a new guiding centre. In doing so, an additional term of the form $\mathbf{A}^* \cdot \mathbf{w}$ is introduced into Equation 2.55. By choosing this velocity transformation such that

$$\mathbf{A}^* \cdot \mathbf{w} + \delta \rho_{\parallel} \dot{\psi_p} = 0$$

we find $\mathbf{w} = -\delta \dot{\psi_p} \mathbf{B} / B^2$. The Lagrangian may now be written in the form of Equation 2.6.1,

$$\mathcal{L} = \left(\rho_{\parallel} I + \psi_t\right) \dot{\theta} + \left(\rho_{\parallel} g - \psi_p\right) \dot{\zeta} + \mu \dot{\xi} - \mathcal{H} \tag{2.56}$$

from which the canonical momenta associated with the three canonical coordinates θ, ζ and ξ are identified as

$$P_\theta = \rho_{\parallel} I + \psi_t, \tag{2.57a}$$

$$P_\zeta = \rho_{\parallel} g - \psi_p, \tag{2.57b}$$

$$P_\xi = \mu. \tag{2.57c}$$

and in the conventional manner of Hamiltonian mechanics the equations of motion follow conveniently from the canonical variables [73] using

$$\dot{\mathbf{p}}_j = -\frac{\partial \mathcal{H}}{\partial \mathbf{q}_j}; \qquad\qquad \dot{\mathbf{q}}_j = \frac{\partial \mathcal{H}}{\partial \mathbf{p}_j},$$

so the equations of motion for this case are

$$\dot{\theta} = \frac{\partial \mathcal{H}}{\partial P_\theta} \qquad \dot{P}_\theta = -\frac{\partial \mathcal{H}}{\partial \theta}$$
$$\dot{\zeta} = \frac{\partial \mathcal{H}}{\partial P_\zeta} \qquad \dot{P}_\zeta = -\frac{\partial \mathcal{H}}{\partial \zeta}$$
$$\dot{\xi} = \frac{\partial \mathcal{H}}{\partial P_\xi} \qquad \dot{P}_\xi = -\frac{\partial \mathcal{H}}{\partial \xi} \ .$$

The toroidal component of the canonical angular momentum completes a set of three adiabatic guiding centre orbit invariants, $(\mathcal{E}, P_\zeta, \mu)$. These Constants of Motion (CoM) of the guiding centre orbits can be used to uniquely represent each particle in the plasma. Within this framework some orbits will be degenerate; the instantaneous direction of travel (i.e. the sign of λ) given by

$$\sigma_d = \frac{v_\parallel}{|v_\parallel|} = \frac{\mathbf{v}\cdot\mathbf{B}}{|\mathbf{v}\cdot\mathbf{B}|} \tag{2.58}$$

is used to distinguish between such orbits.

Electromagnetic Perturbation

At this stage, it is possible to introduce to the system a small, generalised EM perturbation in terms of a small adjustment to the vector and scalar potentials of the form $\tilde{\mathbf{A}}(\mathbf{x},t) = \tilde{A}_{\psi_p}\boldsymbol{\nabla}\psi_p + \tilde{A}_\theta\boldsymbol{\nabla}\theta + \tilde{A}_\zeta\boldsymbol{\nabla}\zeta$ and $\tilde{\Phi}(\mathbf{x},t)$. The perturbed form of the Lagrangian is now written

$$\mathcal{L} = \left(\rho_\parallel I + \psi_t + \tilde{A}_\theta\right)\dot{\theta} + \left(\rho_\parallel g - \psi_p + \tilde{A}_\zeta\right)\dot{\zeta} + \mu\dot{\xi} - \mathcal{H} + \left(\delta\rho_\parallel + \tilde{A}_{\psi_p}\right)\dot{\psi}_p \ , \tag{2.59}$$

whereby, after the same treatment as before to remove the final term, the canonical momenta for the perturbed system are

$$P_\theta = \rho_\parallel I + \psi_t + \tilde{A}_\theta \tag{2.60a}$$
$$P_\zeta = \rho_\parallel g - \psi_p + \tilde{A}_\zeta \tag{2.60b}$$
$$P_\xi = \mu \ . \tag{2.60c}$$

The generalised set of guiding centre equations can now be determined, and are found to be [74]

$$\dot{\theta} = \frac{1}{D}\left[\rho_{\parallel}B^2\left(1-\rho_{\parallel}g'-\tilde{A}'_{\zeta}\right)+g\left\{\left(\rho_{\parallel}^2B+\mu\right)B'+\tilde{\Phi}'\right\}\right] \tag{2.61a}$$

$$\dot{\zeta} = \frac{1}{D}\left[\rho_{\parallel}B^2\left(\rho_{\parallel}I'+q+\tilde{A}'_{\theta}\right)-I\left\{\left(\rho_{\parallel}^2B+\mu\right)B'+\tilde{\Phi}'\right\}\right] \tag{2.61b}$$

$$\begin{aligned}\dot{P}_{\theta} = &-\frac{\rho_{\parallel}B^2}{D}\left[\left(\rho_{\parallel}g'-1+\tilde{A}'_{\zeta}\right)\frac{\partial\tilde{A}_{\theta}}{\partial\theta}-\left(\rho_{\parallel}I'+q+\tilde{A}'_{\theta}\right)\frac{\partial\tilde{A}_{\zeta}}{\partial\theta}\right]\\ &-\left(\rho_{\parallel}B+\mu\right)\frac{\partial B}{\partial\theta}-\frac{\partial\tilde{\Phi}}{\partial\theta}\end{aligned} \tag{2.61c}$$

$$\dot{P}_{\zeta} = -\frac{\rho_{\parallel}B^2}{D}\left[\left(\rho_{\parallel}g'-1+\tilde{A}'_{\zeta}\right)\frac{\partial\tilde{A}_{\theta}}{\partial\zeta}-\left(\rho_{\parallel}I'+q+\tilde{A}'_{\theta}\right)\frac{\partial\tilde{A}_{\zeta}}{\partial\zeta}\right]-\frac{\partial\tilde{\Phi}}{\partial\zeta} \tag{2.61d}$$

where the primes represent derivatives with respect to ψ_p and

$$D = \rho_{\parallel}\left[gI'-g'I\right]+I+qg-I\tilde{A}'_{\zeta}+g\tilde{A}'_{\theta}\ .$$

These four equations represent the guiding centre motion, although the more useful forms of the equations

$$\dot{\psi}_p = \frac{1}{D}\left[\left(I\frac{\partial\tilde{A}_{\zeta}}{\partial\theta}-g\frac{\partial\tilde{A}_{\theta}}{\partial\theta}\right)\dot{\theta}+\left(I\frac{\partial\tilde{A}_{\zeta}}{\partial\zeta}-g\frac{\partial\tilde{A}_{\theta}}{\partial\zeta}\right)\dot{\zeta}-g\dot{P}_{\theta}-I\dot{P}_{\zeta}\right] \tag{2.62a}$$

$$\dot{\rho}_{\parallel} = \frac{1}{I}\left[\dot{P}_{\theta}-\frac{\partial\tilde{A}_{\theta}}{\partial\theta}\dot{\theta}-\frac{\partial\tilde{A}_{\theta}}{\partial\zeta}\dot{\zeta}-\frac{\partial\tilde{A}_{\theta}}{\partial t}-\left(q+\frac{\partial\tilde{A}_{\theta}}{\partial\psi_p}+\rho_{\parallel}I'\right)\dot{\psi}_p\right] \tag{2.62b}$$

can also be formulated. The set of dynamical equations that must be solved in order to follow particle motion using the Hamiltonian guiding centre approach are therefore given by Equations 2.61a, 2.61b, 2.62a and 2.62b [74].

The EM perturbation described here results in a non-conservation of the orbit invariants, as energy is transferred to the perturbation form the particle. Since $\omega \ll \omega_c$, the magnetic moment remains invariant $\Delta\mu = 0$, resulting in a change to $\mathcal{E}_{\perp}$ as the particle experiences a change in magnetic field. The particle energy and toroidal canonical angular momentum in the presence of a perturbation vary according to the relationship [75]

$$\mathcal{E} - (\omega/n)\,P_{\zeta} = K\ , \tag{2.63}$$

where K is a new constant of motion for each particle. The physical interpretation of this is that as a particle moves radially outwards from the core its energy decreases according to $\Delta\mathcal{E} = (\omega/n)\,\Delta P_{\zeta} \sim -(\omega/n)\,\Delta\psi_p$. Due to the low frequency of the

fishbone modes ($\omega < \omega_c$), the change is predominantly to the canonical angular momentum P_ζ (rather than $\mathcal{E}$), leading to a radial redistribution of the fast ions from the assumption that $P_\zeta \sim -\psi_p$.

2.7 Transport in Magnetically Confined Plasmas

The Lawson criterion (Equation 1.6) requires that the heat and particles are confined for sufficient duration that a self-sustained thermonuclear burning plasma is accomplished. Some transport is required in order to remove helium ash, however various detrimental processes occur which result in excessive transport of the heat and particles away from the core.

2.7.1 Classical Transport

In a collisionless plasma, magnetically confined particles are constrained (within a Larmor radius) to move along field lines, and cannot move across the field. Including collisions however can result in a change to the velocity $\Delta\mathbf{v}$, corresponding to a change to the guiding centre position $\Delta\mathbf{x}$ of [76]

$$\Delta\mathbf{x} = -\frac{\mathbf{B} \times \Delta\mathbf{v}}{B\ \omega_c} \ ,$$

hence introducing a cross-field particle transport. This is a key difference between a plasma and a gas; in a plasma, changes in velocity lead to a shift in the orbit position. The culmination of small deflections to $\mathbf{v}$ accumulate over the typical collision time t_c leading to a flux of particles, with a step size approximately equal to ρ_c. The classical diffusion coefficient perpendicular to the field D_c is [16]

$$D_\mathrm{c} \sim \nu_c \rho_c^2 \ ,$$

where $\nu_\mathrm{c} = 1/t_\mathrm{c}$ is the collision frequency. Collisional diffusion is considered to be ambipolar, since the smaller collision frequency $\nu_{ie} = (m_e/m_i)\nu_{ei}$ is cancelled out by the larger step size of the ions $\rho_i = (m_i/m_e)\rho_e$ (where the subscripts i and e represent the electrons and ions), so $D_\mathrm{e,c} \simeq D_\mathrm{i,c} \simeq D_\mathrm{c}$.

2.7.2 Neoclassical Theory

Neoclassical theory expands on the classical theory, retaining the Coulomb collisions but also incorporating the toroidal geometry of the tokamak plasma. At low temperatures, the plasma is considered to be very collisional, so the classical theory

is adequate. At higher temperatures however, when the collision frequency is low, classical transport theory is inadequate. Due to the toroidal geometry, trapped particles have a major influence on the transport. The magnetic field strength varies approximately inversely to the major radius $B_\zeta \sim 1/R$. Particles that are trapped on the LFS of the tokamak due to the magnetic mirror effect experience $\boldsymbol{\nabla}\mathbf{B}$ and curvature drifts that cause them to have finite orbit width w_b of the order [16]

$$w_b \sim \frac{q\rho_c}{\varepsilon_r^{1/2}}$$

where $\varepsilon_r(\psi_p)$ is the inverse aspect ratio on a flux surface, which varies with radius. The radial excursion of the trapped particles is larger than the Larmor radius $w_b > \rho_c$. An important parameter in magnetic confinement fusion is the 'collisionality' ν_* [76], defined as the ratio of the trapped particle bounce time t_b to the effective confinement time τ_eff

$$\nu_* \equiv \frac{t_b}{\tau_\mathrm{eff}} \equiv \frac{\nu_\mathrm{eff}}{\omega_\mathrm{b}} = \frac{\nu \mathbf{R} q}{\varepsilon^{3/2} v_\mathrm{th}}$$

where $\nu_\mathrm{eff} = \nu/\varepsilon$ is the effective collision frequency and $\omega_\mathrm{b} = 1/t_\mathrm{b}$ is the bounce frequency. The collisionality defines the number of times a trapped particle completes a banana orbit before it is scattered into a passing orbit. Using the effective collision frequency in conjunction with the banana orbit width, an estimate for the neoclassical diffusion coefficient D_n can be made, assuming that the fraction of trapped particles is $\sim \varepsilon_r^{1/2}$ [16]

$$D_n \sim \frac{q^2}{\varepsilon_r^{3/2}} \nu_\mathrm{eff} \rho_c^2 = \frac{q^2}{\varepsilon_r^{3/2}} D_\mathrm{c} \ .$$

The neoclassical regime described above considers trapped particles which undergo at least one banana orbit before a collision. This is referred to as the (virtually collisionles) banana regime, defined by $\nu_* \ll 1$. At larger collisionality is the Pfirsch-Schlüter regime, defined by $\nu_* \gg 1$, where no banana orbits exists since the trapped particles are deflected via a collision before the orbit can be completed. Between these two regimes lies a range of collision frequencies in which the diffusivity remains constant. This is the plateau regime, which is dominated by a class of slowly circulating particles. The variation of diffusion coefficient with collisionality is shown in Figure 2.5.

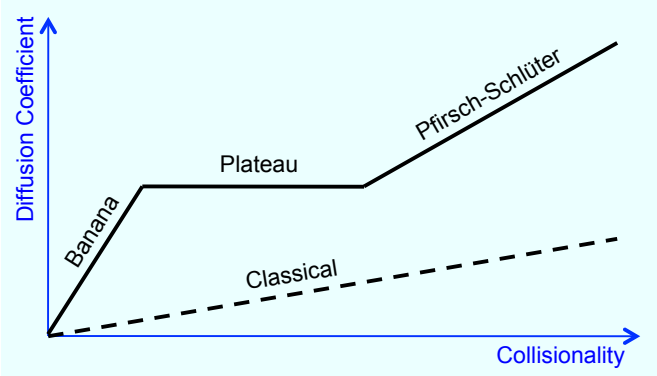

Figure 2.5: Three diffusion coefficient regimes as a function of collision frequency. Adapted from [16].

2.7.3 Anomalous Transport

Transport in tokamak plasmas is significantly larger than predicted by either of the aforementioned theories. The reason for this transport is not well understood, and is subsequently referred to as 'anomalous transport'. Anomalous transport causes particles and heat to be lost at a level larger even than neoclassical levels (by as much as two orders of magnitude for electrons [16]). It is primarily this large level transport that has resulted in fusion not yet becoming a commercial reality.

The current understanding of anomalous transport is that heat and particles are transported due to plasma instabilities. Turbulence plays a key role in transporting heat and particles across field lines [77]. Macroscopic plasma instabilities also play a role, with MHD-like modes that affect the magnetic structure.

The anomalous transport greatly reduces both the particle and energy confinement time. To combat this, ever larger tokamak devices are required, such as ITER which has a plasma volume of 840m^3, over eight times the volume of the current largest tokamak, JET [78]. A fundamental understanding of the anomalous transport effects on confinement is not known; our best estimates are built up using empirical methods via the accumulation of data from a range of tokamaks. It is these empirical estimates that are extrapolated to make predictions for future devices [79, 80].

2.7.4 Fast Ion Transport

The EPs in the tokamak used to heat the plasma is not immune to transport; as discussed previously the transport of these fast ions is observed to cause significant degradation to the plasma heating. In MAST, transport of the fast ions appears

mainly to be due to EPMs. The plasma instabilities responsible for the transport processes described here are explained in the next section.

Transport of fast ions can be classified into four types [81]. The first is phase-locked convective transport, where resonant particles 'lock' into phase with a plasma instability (defined as a wave) as they traverse the device [82]. EPMs of this type often adjust in frequency to match the orbit frequency of the particles as they move out radially, and the transport caused by these modes scales linearly with mode amplitude. The second type is when the fast particle orbit topology changes from one type to another, due to an invariance in the constants of motion of its orbit caused by an instability. A wide range of orbit types exist beyond just trapped and passing, see Section 4.2. The enhanced effect that trapped orbits have on the transport has been discussed previously. On top of this, small changes to the constants of motion of the particle caused by the instability can result in it being moved into an orbit which is no longer confined by the device. Diffusive transport makes up the third type of EP transport, whereby the fast ions are subject to multiple perturbations from the $\mathbf{E} \times \mathbf{B}$ force during their orbit, resulting in stochastic transport [83]. The fourth type of fast particle transport is avalanches. These occur when an instability moves fast ions to a new location, steepening the spatial gradient there. This destabilises another mode, causing an 'avalanche' of destabilised modes one after another [84]. An example is Toroidal Alfvén Eigenmode (TAE) avalanches observed on NSTX [49], modelling of which has shown good agreement with experiment [85, 86].

2.8 MHD Instabilities

2.8.1 Alfvén Gap Modes

Shear Alfvén Waves (SAWs) are low frequency EM waves that propagate along the magnetic field $\mathbf{B}$. Analogous to waves on propagating along a taught string, their restoring force is due to the magnetic field. For a low wave frequency compared to the ion cyclotron frequency $\omega < \omega_c$ the dispersion relation may be written

$$\omega = k_{\|} v_A \ , \tag{2.64}$$

where $k_{\|}$ is the wave vector in the direction of the magnetic field and

$$v_A = \frac{B}{\sqrt{\mu_0 \sum_a n_a m_a}}$$

is the Alfvén speed [87]. The sum is over the density n_a and mass m_a of each species a in the plasma. Since the waves are polarised in the transverse direction, the perpendicular component of the perturbations to the magnetic and electric fields are much larger than the parallel components, i.e. $\tilde{\mathbf{B}} \gg \tilde{B}_{\|}$ and $\tilde{\mathbf{E}} \gg \tilde{E}_{\|}$ The waves have a constant phase velocity v_{phase} for all frequencies, where $v_{\text{phase}} = \omega\mathbf{k}/k^2$, such that in a uniform plasma the waves are dispersionless.

Consider a wave in a cylinder with a uniform field along its axis $\hat{z}$, the wave electric field is in the radial direction $\hat{r}$ and its magnetic field is in the azimuthal direction $\hat{\theta}$. The azimuthal component must be periodic, and is therefore represented by the poloidal mode number, m. Considering at this stage a tokamak to be akin to a cylinder bent around and connected end to end, the analogous is true along the axial direction, whereby the periodic nature of the perturbation is denoted by the toroidal mode number n. For an axial (toroidal) periodicity of $2\pi R$, these constraints impose the relation between the two mode numbers defined by the safety factor,

$$k_{\|} = \frac{(n - m/q)}{R} \ .$$

In contrast to the uniform cylinder case above, in a tokamak $B_\zeta \sim 1/R$. This means that both the safety factor and the Alfvén speed are functions of the major radius $q(R)$, $v_A(R)$, which leads to a radially dependent mode frequency. If the wave still satisfies the dispersion relation in Equation 2.64 it is subsequently referred to as being part of the Alfvén 'continuum' (depicted schematically in Figure 2.1).

Within the Alfvén continuum, instabilities are rapidly damped. This may be conceptualised by considering a wave packet of finite radial size within the continuum. The radial dependence of the frequency $\omega(R)$ means that across the width of the wave packet it is moving at different velocities and directions. Known as phase mixing [88], this effect causes the pulse to rapidly disperse [65, 81]. The EP population cannot provide sufficient energy to overcome this, such that the mode is damped with an associated damping rate rate proportional to the gradient in the phase velocity,

$$\gamma_d \sim -\left| \frac{\mathrm{d}}{\mathrm{d}r} \left(k_{\|}(R) v_A(R) \right) \right| \ .$$

When SAWs are located in the continuous part of the frequency spectrum there is rapid dispersion such that they are rarely destabilised. However, 'frequency gaps' can manifest themselves within the Alfvén continuum where the radial variation in frequency $\partial\omega/\partial r \to 0$, resulting in an effective potential well in the continuum frequency which results in a reduction to the continuum damping. Within these gaps discrete, weakly damped modes can appear of finite radial extent that grow with an

associated growth rate. The periodic nature of the tokamak geometry results in a multitude of frequency gaps prevailing in the device.

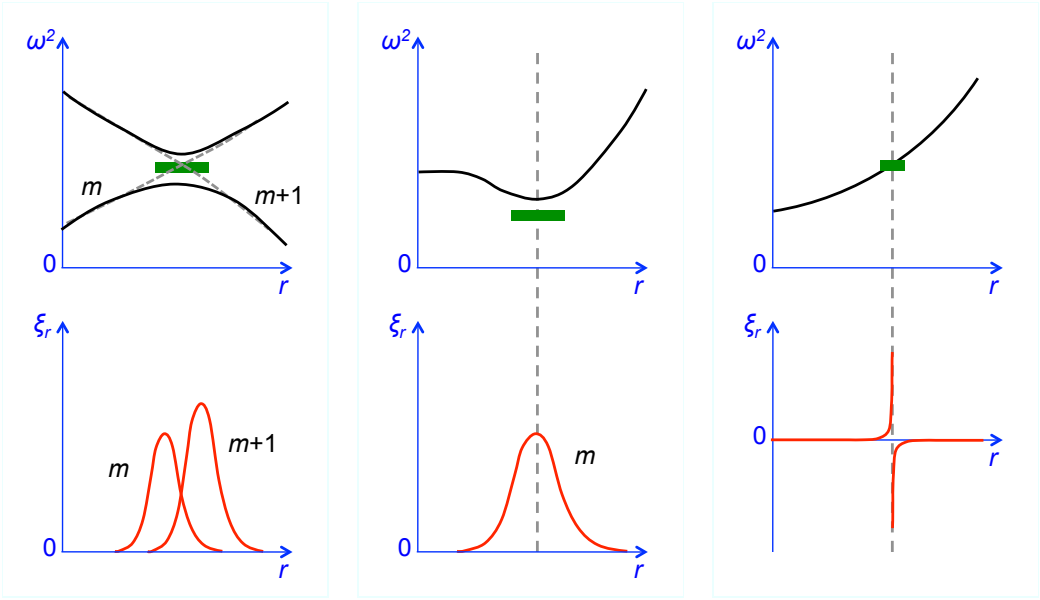

(a) Coupling type. (b) Extremum type. (c) Continuum type.

Figure 2.6: Frequency (top) and mode structure (bottom) of Alfvén wave instabilities, as if stimulated by an external antenna at the frequency shown by the green region. Adapted from [65, 81].

There are three general types of eigenmodes. The first is where the frequency of counter-propagating waves cross, creating a 'coupling type' mode, as shown in Figure 2.6(a). Since the field is inversely proportional to the major radius, $B_\zeta \sim 1/R$, the Alfvén speed varies along a field line (as it wraps around the device it moves towards and away from the central solenoid, see Figure 1.3). Counter-propagating waves with the same toroidal mode number n and adjacent poloidal mode numbers m and $m+1$ end up crossing at the point where their wave numbers are $k_\parallel = n/R - m/qR$ and $k_\parallel = -|n/R - (m+1)/qR|$ respectively. The toroidicity of the device resolves the degeneracy of the two waves at this location, which occurs where the safety profile is

$$q = \frac{m + 1/2}{n} \ ,$$

found by setting $k_\parallel$ of the two counter-propagating waves equal to each other. At the point at which the frequency crossing occurs, the continuum damping is removed, resulting in a weakly damped growing mode. Since this is due to the toroidicity of the device, they are referred to as TAE modes. The mode occurs at a specific

frequency at the centre of the frequency gap, given by

$$\omega = \left|k_{\|}\right| v_A = \frac{v_A}{2qR} \ ,$$

with a corresponding magnitude of

$$\left|k_{\|}\right| = \frac{n}{2R} \ .$$

The second type of mode is where there is an extremum in the continuous spectrum, such that the continuum damping is removed (see Figure 2.6(b)). Such 'extremum type' modes include Reversed Shear Alfvén Eigenmodes (RSAEs), the characteristic appearance of which is at rational $q_{\min}$ values where $\partial\omega/\partial r$ vanishes. Several RSAEs occurring at once is known as an 'Alfvén Cascade' and can even be used as a q-profile diagnostic [89].

The third type occurs when the EP pressure reaches a sufficiently high level, and modes appear at the frequency of the population whereby it is sufficiently large to actually overcome the continuum damping. These are known as 'continuum type' instabilities, as shown in Figure 2.6(c).

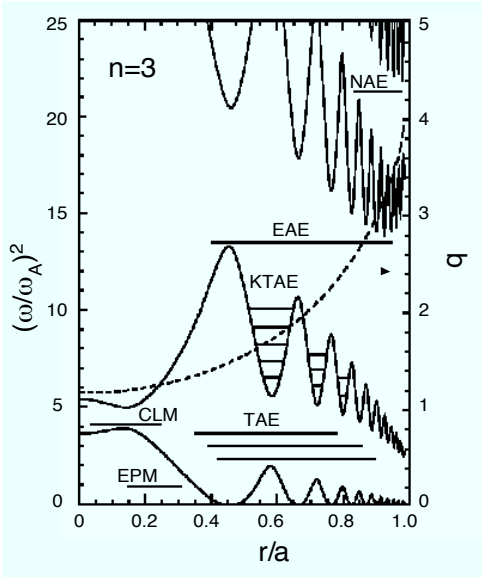

Figure 2.7: Shear Alfvén frequency continuum curves as a function of normalised radius. The horizontal lines represent approximate frequency, radial location and mode with of various modes. Figure taken from [50].

Further frequency gaps produced by the periodic variation in Alfvén speed result in a whole 'zoo' of Alfvén Eigenmodes (AEs), whose names refer to the cause

of the frequency gap. Figure 2.7 shows the modes mentioned above in addition to other modes as a function of radius. Compressional Alfvén Eigenmode (CAE) modes are compressional waves, where the perturbation is parallel to the equilibrium field, $\delta B \parallel B$. Global Alfvén Eigenmode (GAE) are shear waves with a perturbation perpendicular to the equilibrium field $\delta B \perp B$, referred to as global to distinguish them from singular eigenmodes [90]. Kinetic TAE (KTAE) are based on a theoretical model which also takes into account kinetic effects, yielding additional modes just above the TAE frequency [91]. A final example is the Beta-induced Alfvén Acoustic Eigenmode (BAAE) which results from coupling between shear Alfvén waves and acoustic waves [92].

2.8.2 Mode Destabilisation

It is the free energy in the EP population that drives the Alfvén instabilities. In order for power transfer to occur between the EP population and the wave, there must be a finite value of $\mathbf{v} \cdot \mathbf{E}$, where $\mathbf{v}$ is the velocity vector of the particle and $\mathbf{E}$ is the wave electric field. A relativistic transformation of the electric field means that a particle travelling though a uniform plasma at the phase velocity of the wave experiences only a magnetic perturbation. The rapid gyro-motion compared to the mode frequency means that the velocity contribution perpendicular to $\mathbf{B}$ averages to zero,

$$\oint \mathbf{v}_\perp \cdot \mathbf{E} = 0 \ .$$

The energy transfer between a particle and the field is given by [81]

$$\frac{\mathrm{d}\mathcal{E}}{\mathrm{d}t} = eZ\mathbf{v}_d \cdot \mathbf{E}_\perp + eZv_\parallel E_\parallel + \mu \frac{\partial B_\parallel}{\partial t} \ .$$

It is the first term on the right hand side of this equation containing the transverse electric field component $\mathbf{E}_\perp$ that is considered dominant, interacting with the drift velocity $\mathbf{v}_d$ of the fast ions (caused by the mechanisms outlined previously). This is best understood when considering the interaction over multiple orbit cycles (this is allowed since the growth rate is small compared to the mode frequency $\gamma < \omega$). A fraction of the fast particle population remains resonant with the wave for sufficient duration for energy transfer to take place. This fraction is referred to as the 'resonant' part of the distribution function, and is identified by means of the toroidal ω_ζ and poloidal ω_θ motion frequencies of the relevant fast ions. Resonant

ions fulfil the criteria

$$\begin{aligned} \omega - \langle \mathbf{k} \cdot \mathbf{v} \rangle &= 0 \\ \omega - n\omega_\zeta + p\omega_\theta &= 0 \ , \end{aligned} \tag{2.65}$$

where n is the familiar toroidal mode number and p is the bounce harmonic of the particle (an integer). This is the resonance condition, however it is necessary to have a nonzero $\oint \mathbf{v}_\perp \cdot \mathbf{E}$ for energy transfer to occur.

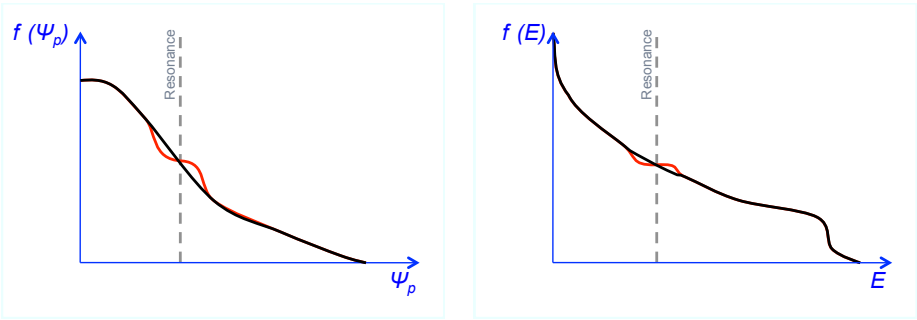

(a) $f(\psi_p)$ (b) $f(\mathcal{E})$

Figure 2.8: Instability drive and damping mechanisms of the EP population. The initial (black) and perturbed (red) fast ion distribution function is shown.

The magnitude of the energy transfer that takes place is dependent upon the properties of the fast ion population. The situation is comparable to the case of Landau damping [93], where particles travelling at velocities slightly below the phase velocity of the wave gain energy from it and those travelling slightly faster than the wave phase velocity loose energy to it. Landau damping is often explained by means of an analogy with a surfer on a wave. A Landau damping-like process occurs in fusion plasmas, resulting in a small-scale flattening of the EP population localised around the particle resonance. If the particle population is decreasing along the direction of the resonance coordinate, energy is transferred to the EP population and the wave is damped. This energy transfer to the wave is proportional to the growth rate, given by

$$\gamma = \omega \frac{\partial f}{\partial \mathcal{E}} + n \frac{\partial f}{\partial P_\zeta} \ . \tag{2.66}$$

The gradient along the third adiabatic invariant ($\partial f / \partial \mu$) makes no contribution as μ is unaltered by low frequency AEs.

An example of this local flattening is shown in Figure 2.8. The negative energy gradient in Figure 2.8(b) means that there are more lower-energy particles than higher-energy particles, resulting in the particles taking energy from the wave

(which is therefore damped). Since the canonical angular momentum $P_\zeta \sim -\psi$, the negative radial gradient shown in Figure 2.8(a) can actually result in energy transfer from particles to the wave. This can drive the mode, contributing to a positive growth rate γ. When the mode has been driven unstable, a wide range of nonlinear dynamics is observed including steady modes that gradually saturate, bursting mode behaviour and frequency chirping.

2.8.3 Energetic Particle Modes

The modes discussed above are normal modes of the background plasma. For these modes, it is the EP population that drives them unstable, as shown in Figure 2.2. The fast ions perturb both the real part (the frequency) and the imaginary part (the growth rate) of the mode by the same amount. Since the mode frequency ω_0 is already significant, the perturbation has little effect. The unperturbed wave is stable $\gamma = 0$, so the perturbation to the growth rate is significant.

When the EP pressure is close to (or greater than) that of the thermal plasma, EPMs appear, for which the EP population is responsible. Such instabilities have eigenfunctions which resemble that of a related gap mode, but have their own dispersion relation and belong to a separate wave branch. For a sufficiently large mode drive from the fast ions, the EPM will be unstable even if it has a frequency within the Alfvén continuum [81, 94].

Chapter 3

The Fishbone Instability

3.1 Tokamak Scenarios

In order to achieve the goal of a steady-state tokamak plasma operating in a fusion power plant, it will be necessary to apply the minimum amount of power required to drive the plasma current non-inductively whilst maintaining a sufficiently high plasma β to sustain the fusion. Present day assessments suggest that tokamak operation of this type will be done using what are referred to as 'Advanced Tokamak Scenarios' [95–97], whereby operation at a low plasma current and a high plasma pressure maximises the self-generation of the required non-inductive bootstrap current (a current resulting from radial pressure gradients that does not require external current drive). A major problem with this is that decreasing the plasma current causes a decrease to the energy confinement time. In addition, high-pressure, low-current regimes are particularly susceptible to MHD instabilities, such that the study of these instabilities is crucial in the development of scenarios for future devices.

The two primary candidates for continuous tokamak operation are the steady-state scenario [95], which has reversed magnetic shear in the core and the hybrid scenario [98], which has a broad low-shear region and retains q >1. The magnetic shear profile in this scenario is a consequence of the optimised bootstrap current. The current profiles, in conjunction with core-peaked pressure profiles results in an inherent susceptibility to ideal $n = 1$ kink-ballooning modes [99]. For this reason, it is desirable to retain an above-unity minimum value of the safety factor profile $q_{\min} > 1$ to reduce the vulnerability to kink modes.

3.2 Fishbones

Suprathermal ions injected into a tokamak were at one stage considered to have a stabilising influence on the magnetically confined plasma. This was because their net potential is averaged out due to their high precession frequency, and also because they can form a diamagnetic well which acts to 'stiffen up' the plasma. Fast ions with a precession frequency larger than the mode frequency have a stabilising effect on both ballooning modes, shown by Connor *et. al.* [100] (when the precession frequency is larger than the bounce frequency) and Rosenbluth *et. al.* [101] (when the precession frequency is less than the bounce frequency).

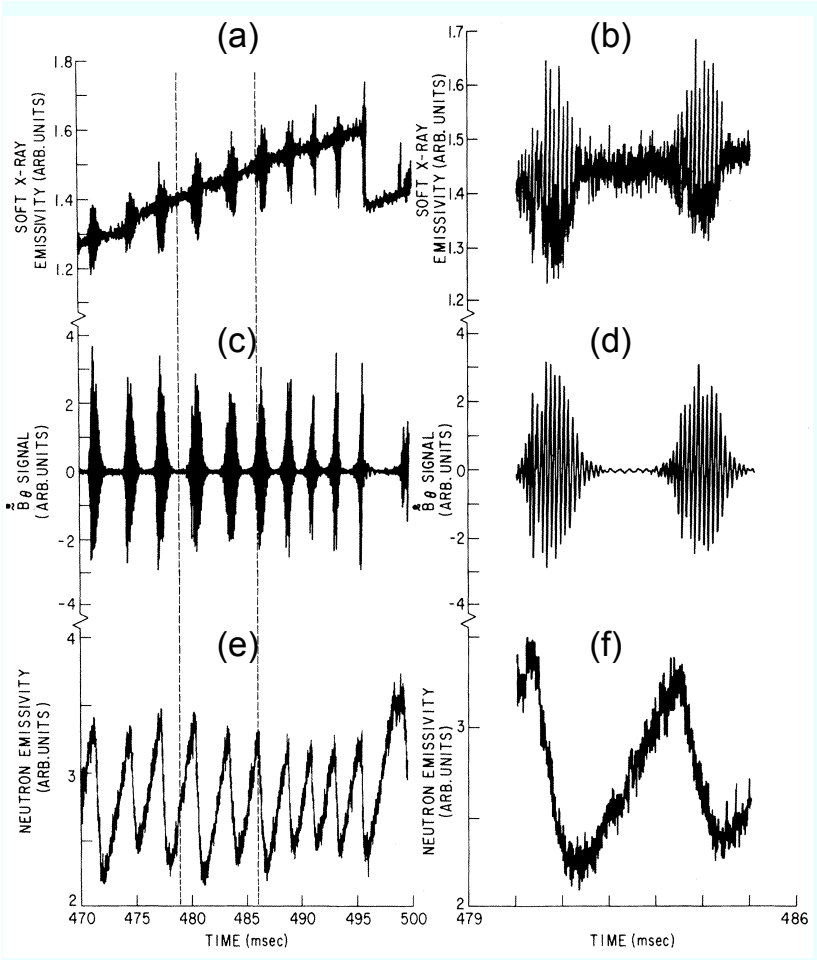

Figure 3.1: Fishbone modes were first observed in PDX [43] and named after their characteristic Mirnov coil signal, shown in (d). Signal bursts in the SXR signal (a) and (b) coincide with similar bursting activity in the magnetic perturbation diagnostic (c) and (d). The bursts result in a drop in the fusion rate, detected by means of a drop in the neutron emissivity (e) and (f).

The opposite was subsequently observed during perpendicular neutral beam injection on PDX in the early 1980s [43]. Bursting modes were detected in both the SXR and magnetic perturbation diagnostics for high beta ($\beta_q \geqslant 0.045$) discharges. Shown in Figure 3.1, the modes typically lasted for <1ms with an inter-mode period of 1-6ms. They were found to cause a 20%-40% loss in beam heating power (measured by means of the neutron emission, which dropped by up to 40% - Figure 3.1(f)). The characteristic form of the Mirnov coil signal detected during these bursts of MHD activity is considered to resemble the skeleton of a fish which led to the modes being dubbed the 'fishbone instability'. Two such fishbones are shown in figure Figure 3.1(d) from the paper that coined the term [43]. The fishbones were attributed to a $n = 1$, $m = 1$ 'precursor' mode, superimposed onto a larger $n = 0$, $m = 0$ sawtooth mode. Fourier decomposition of the Mirnov coil signal found the mode to be rotating in the ion diamagnetic drift direction (the same direction as the beam injection and fast ion precession direction). The complex mode structure was found to also consist of modes with $m > 1$. The MHD activity occurs near the $q = 1$ surface. The maximum fishbone activity was found at low magnetic field and high beam power.

White showed analytically and computationally [82] that the fast ions led to a degradation in confinement via resonant ejection of the trapped particles in the case where their precession rate matched the mode frequency of the n=1 m=1,2,3 internal kink mode.

The frequency sweeping is caused because a marginally unstable eigenmode in the system will sweep in frequency. The nonlinear bounce frequency ω_b of a particle trapped in the potential well of a wave is related to the frequency shift $\delta\omega$, and it is the nonlinear wave-particle interaction that determines the frequency sweep rate [102].

3.2.1 Types of Fishbone Mode

The linear instability is identified as two separate branches. The original interpretation described above makes up the first of these, referred to as so-called 'precessional' fishbones. The theoretical framework for these was put into place by Chen, White and Rosenbluth [103] who identified the key role played by the fast ions in destabilising the modes below the plasma pressure threshold predicted by the ideal MHD theory (see Section 3.4). The precessional branch is concerned with modes with frequencies greater than the thermal ion diamagnetic frequency $\omega_{*\mathrm{i}}$,

$$\omega \gg \omega_{*\mathrm{i}}$$

where [104]

$$\omega_{*\mathrm{i}} = \frac{n}{en_i}\frac{\partial P_i}{\partial \psi_p}$$

in which P_i, n_i and e are the ion pressure, density and charge. The ion diamagnetic frequency is a function of radius, as density and pressure are both functions of radius and are approximated to flux functions (functions of ψ_p). Precessional fishbones are continuum-type EPMs, whereby trapped energetic ions destabilise the dominant $n = 1$, $m = 1$ mode in the Alfvén continuum, and are as such subject to continuum damping. The mode drive from the EP population almost balances the damping, reaching a marginal stability near the $q = 1$ surface [105]. The continuum damping means that the fishbones are excited at high values of fast ion beta β_f, since at low β_f there is insufficient mode drive (a threshold exists, see Equation 3.11). The second regime is for fishbones resonant at the ion diamagnetic frequency,

$$\omega \approx \omega_{*\mathrm{i}}$$

introduced by Coppi and Porcelli [106]. These 'diamagnetic' fishbones lie within a low frequency gap in the Alfvén continuum, and are subsequently not subject to continuum damping.

Precessional fishbones are often referred to as a trapped particle induced instability since the real frequency of the mode (the imaginary part being the growth rate) is comparable to the trapped particle precession frequency, ω_ζ. Destabilisation of fishbones is not reserved only to trapped particles, resonant passing particles can also contribute [107]. For passing particles, ω_ζ refers to the 'transit' frequency, which is equivalent to the trapped precession frequency for passing particles. It is the reciprocal of the time taken to traverse the plasma once toroidally. Resonant destabilisation of kink modes at the transit frequency of passing particles is also possible and therefore also contributes [108]. The resonant interaction between the internal $n = 1$, $m = 1$ kink mode and the trapped fast particles is characterised by a classic Landau damping mechanism, whereby a flattening occurs in the distribution function centred around the resonance (Section 2.8.2).

In addition to fishbones driven by suprathermal ions, barely trapped suprathermal electrons have been attributed to causing what is known as 'electron fishbones', destabilised by an inverted spatial gradient in the suprathermal electron tail. A gap mode travelling in the ion diamagnetic direction can be destabilised, or a continuum mode in the electron diamagnetic direction [109]. The small size of the electron drift orbits means that electron fishbones in present day devices may be used to make predictions for the features of ion driven fishbones in larger future devices [110].

The high plasma β achievable [111] in conjunction with the significant trapped particle fraction due to the magnetic topology of STs suggests that they are particularly susceptible to the fishbone instability [112, 113]. Studies have found that a magnetic valley can lead to fishbone stabilisation in ST plasmas when the magnetic field is increasing outward for enough of the plasma with $q > 1$ [113].

In order to achieve ignition in future devices such as ITER, the effect of fast particle driven instabilities will be crucial [50]. A study was carried out specifically into fishbones, and found that for ITER-like parameters the threshold for the onset of fishbones is an on-axis plasma β of 1% [51]. This is only marginally above the expected value in ITER, so α-particle driven fishbone oscillations are considered likely.

3.3 Interpretation of Fishbone Modes

The instability responsible for the fishbone mode is interpreted from the Mirnov coil data to be an internal kink mode that is driven unstable by the fast ion population. It is called a kink mode because it leads to a kinking of the magnetic flux surfaces. The drive for the kink mode is the radial gradient in toroidal current at low β, and additionally the pressure gradient contributes at higher β. The potential energy of the kink mode contains a contribution from the plasma δW_{p} and a contribution from the vacuum δW_{v}, and is of the form [16]

$$\delta W = \delta W_{\mathrm{p}} + \delta W_{\mathrm{v}} \ .$$

The plasma contribution is given by [16]

$$\begin{aligned} \delta W_{\mathrm{p}} &= \frac{\pi^2 B_\zeta^2}{\mu_0 R} \int_0^a \left[\left(r \frac{\mathrm{d}\xi}{\mathrm{d}r} \right)^2 + \left(m^2 - 1 \right) \xi^2 \right] \left(\frac{n}{m} - \frac{1}{q} \right)^2 r \ \mathrm{d}r \\ &+ \left[\frac{2}{q_a} \left(\frac{n}{m} - \frac{1}{q_a} \right) + \left(\frac{n}{m} - \frac{1}{q_a} \right)^2 \right] a^2 \xi_a^2 \end{aligned}$$

where a denotes the radius at the plasma edge and the subscript a indicates the value at that radius. The vacuum contribution is given by [16]

$$\delta W_{\mathrm{v}} = \frac{\pi^2 B_\zeta^2}{\mu_0} m \left(\frac{1 + (a/b)^{2m}}{1 - (a/b)^{2m}} \right) \left(\frac{n}{m} - \frac{1}{q_a} \right)^2 a^2 \xi_a^2$$

In the case when this potential $\delta W_{\mathrm{p}} > 0$ the plasma will be stable, but when it becomes negative the instability will grow. Fishbone modes are considered to be

'internal' kink modes, contained fully within the Last Closed Flux Surface (LCFS), so the vacuum contribution is zero and the potential energy is reduced (within the large aspect ratio approximation, $\varepsilon = a/R \ll 1$) to [16]

$$\delta W_{\mathrm{p}} = \frac{\pi^2 B_\zeta^2}{\mu_0 R} \int_0^a \left[\left(r \frac{\mathrm{d}\xi}{\mathrm{d}r} \right)^2 + \left(m^2 - 1 \right) \xi^2 \right] \left(\frac{n}{m} - \frac{1}{q} \right)^2 r \, \mathrm{d}r + \mathcal{O}\left(\varepsilon^2 \right)$$

in which the $\mathcal{O}\left(\varepsilon^2\right)$ term is small compared to the first term. To leading order in ε the minimum value of δW is zero. This means that the mode is marginally stable, and the stability is determined by the sign of the $\mathcal{O}\left(\varepsilon^2\right)$ term [114].

3.4 Fishbone Dispersion Relation

The linearised MHD momentum equation is given in Equation 2.25. By replacing the velocity derivative with the fluid displacement vector (Equation 2.30) and assuming a constant fishbone mode growth rate γ, the first-order equation for the displacement is

$$\rho_0 \gamma^2 \boldsymbol{\xi} = \mathbf{j}_0 \times \tilde{\mathbf{B}} + \tilde{\mathbf{j}} \times \mathbf{B}_0 - \boldsymbol{\nabla} \tilde{P}_c - \boldsymbol{\nabla} \tilde{P}_h \ . \tag{3.1}$$

The pressure disturbance has been split into a core plasma pressure perturbation $\tilde{P}_c$ and a perturbation to the hot EP population pressure $\tilde{P}_h$

$$\tilde{P} = \tilde{P}_c + \tilde{P}_h \ . \tag{3.2}$$

The core plasma pressure displacement is given by

$$\tilde{P}_c = -\xi \cdot \boldsymbol{\nabla} P_c - \gamma_c P \boldsymbol{\nabla} \cdot \boldsymbol{\xi} \ ,$$

and the MHD relations $\tilde{\mathbf{E}}_\perp = \gamma \boldsymbol{\xi} \times \mathbf{B}_0$, $\tilde{\mathbf{E}}_\parallel = 0$, $\tilde{\mathbf{B}} = \boldsymbol{\nabla} \times (\boldsymbol{\xi} \times \mathbf{B}_0)$ and $\tilde{\mathbf{j}} = \boldsymbol{\nabla} \times \tilde{\mathbf{B}}$ are all retained. Assuming fixed boundary conditions and multiplying Equation 3.1 by $\int \boldsymbol{\xi}^* \mathrm{d}^3 x$ gives

$$\delta I + \delta W_{\mathrm{K}} + \delta W_{\mathrm{MHD}} = 0 \tag{3.3}$$

where

$$\delta I = \gamma^2 \int \rho_0 \left|\boldsymbol{\xi}\right|^2 \, \mathrm{d}^3x \tag{3.4}$$

$$\delta W_{\mathrm{K}} = \int \boldsymbol{\xi} \cdot \boldsymbol{\nabla} \tilde{P}_h \, \mathrm{d}^3x \tag{3.5}$$

$$\begin{aligned} \delta W_{\mathrm{MHD}} &= -\int \left(\mathbf{j}_0 \times \tilde{\mathbf{B}}\right) \cdot \boldsymbol{\xi} \, \mathrm{d}^3x + \int \left(\tilde{\mathbf{j}} \times \mathbf{B}_0\right) \cdot \boldsymbol{\xi}^* \, \mathrm{d}^3x - \int \boldsymbol{\nabla} \tilde{P}_c \cdot \boldsymbol{\xi} \, \mathrm{d}^3x \\ &= -\int \left[-\mathbf{j}_0 \cdot \left(\tilde{\mathbf{B}} \times \boldsymbol{\xi}^*\right) + \frac{1}{\mu_0} \left|\tilde{\mathbf{B}}\right|^2 - \tilde{P}_c \left(\boldsymbol{\nabla} \cdot \boldsymbol{\xi}\right)\right] \, \mathrm{d}^3x \end{aligned} \tag{3.6}$$

where δW_{MHD} is the potential energy from the core plasma, δI is the inertial term and δW_{K} is the contribution from the EP population. From here, it is possible to recover the Chen, White and Rosenbluth version of the dispersion relation [103] (a full derivation of this may also be found in [115]),

$$-\frac{i\omega}{\tilde{\omega}_A} + \delta\hat{W}_f + \delta\hat{W}_k = 0 \tag{3.7}$$

where the growth rate has been replaced using $\gamma = -i\omega$ and $\tilde{\omega}_A = v_A/(3^{1/2}R_0qS)$. The first term is the inertial layer contribution from the thermal ions. The other two terms are the potential energy comprising of the fluid (core plasma) contribution $\delta\hat{W}_f$ from the AE continuum described by ideal MHD and the kinetic (fast ion) contribution $\delta\hat{W}_k$ from the EP population. These terms can be found from those in Equation 3.3 using [115]

$$\delta\hat{W}_f \approx \frac{\delta W_{\mathrm{MHD}} + \delta I}{\pi R B_{\theta \mathrm{s}} \left|\boldsymbol{\xi}_r\right|^2 / \mu_0} + \frac{i\omega}{\tilde{\omega}_A} \tag{3.8}$$

for the fluid term and

$$\delta\hat{W}_k = \frac{\mu_0 \, \delta W_k}{\pi R B_{\theta \mathrm{s}}^2 \left|\boldsymbol{\xi}_r\right|^2} \tag{3.9}$$

for the kinetic contribution, where $B_{\theta \mathrm{s}}$ is the poloidal field at the peak radial location of the perturbation. The ideal MHD dispersion relation may be recovered by setting $\delta\hat{W}_k = 0$.

Two discrete types of modes are demonstrated by the fishbone dispersion relation (Equation 3.7). These are discrete gap modes, or AEs for $\mathbb{R}\mathrm{e}(\omega/\tilde{\omega}_A) < 0$ and EPMs for $\mathbb{R}\mathrm{e}(\omega/\tilde{\omega}_A) > 0$ [94]. For the AEs, the resonant fast ion response $\mathbb{R}\mathrm{e}(\delta W_k)$ in conjunction with δW_f provides a frequency shift, removing the SAW continuum degeneracy so that the mode is weakly damped [116]. Mode drive comes from the resonant wave-particle interaction $\mathbb{I}\mathrm{m}(\delta W_k)$, which is enough to overcome the small

(but finite) damping due to the core plasma component. For the EPM, the frequency ω is set by the characteristic frequency of the relevant EPs; in the case of fishbones it is the time-averaged toroidal precession frequency $\langle\omega_\zeta\rangle$. The drive required for the EPM must exceed the continuum damping threshold, i.e. $\mathbb{I}\mathrm{m}(\delta W_k) > \mathbb{R}\mathrm{e}(\omega/\tilde{\omega}_A)$. Additionally, the non-resonant fast ion response is important, as it provides a compressional effect to balance the wave potential energy [103].

Substituting $\delta\hat{W}_k$ for a distribution of fast particles at constant energy yields a threshholdless unstable solution (an EPM) with a frequency equal to the toroidal precession frequency $\omega = \langle\omega_\zeta\rangle$. The drive increases with the average fast particle beta within the $q = 1$ surface $\langle\beta_f\rangle_{q=1}$. This links the fast particle precession to a core-plasma MHD mode that is dissipated due to the Alfvén resonance at $\omega_r \sim k_\| v_A$ (Equation 2.64) [103]. The internal kink mode is also damped as it is coupled to the Alfvén continuum.

For a NBI powered slowing-down distribution function in a plasma with a monotonic q-profile the dispersion relation is [103]

$$-i\frac{\omega}{\omega_\mathrm{A}} + \delta\hat{W}_f + \left\langle\beta_f\hat{I}_0\right\rangle_{q=1}\Omega\,\log\left(1-\frac{1}{\Omega}\right) = 0 \tag{3.10}$$

where $\Omega = \omega/\langle\omega_\zeta\rangle$ and the toroidal precession frequency is found for the particle with the highest energy and $\hat{I}_0$ can be found in [103]. The fishbone is driven unstable when the β_f term surmounts the Alfvén continuum damping around the $q = 1$ surface. When the system is at the point of marginal stability, ω is real. The value of $\langle\beta_f\rangle_{q=1}$ provides a stability threshold that can be found from the imaginary part of Equation 3.10

$$\langle\beta_f\rangle_{q=1} > \frac{\omega_\zeta}{\left\langle\hat{I}_0\right\rangle_{q=1}\pi\omega_\mathrm{A}}\ . \tag{3.11}$$

The dispersion relation above can be extended to include a non-monotonic q-profile. The dispersion relation found is given by [117]

$$\begin{aligned}
&\sqrt{r_1^2 q''}\left[(\Delta q)^2 - 3\Omega(\Omega-\omega_{*i})\left(\frac{\langle\omega_\zeta\rangle^2}{\omega_\mathrm{A}}\right)\right]^{1/2} \\
\times\ &\left[\Delta q + \left((\Delta q)^2 - 3\Omega\,(\Omega-\omega_{*i})\,\frac{\langle\omega_\zeta\rangle^2}{\omega_\mathrm{A}^2}\right)^{1/2}\right]^{1/2} \\
+\ &\delta\hat{W}_f + \left\langle\beta_f\hat{I}_0\right\rangle_{q=1}\Omega\,\log\left(1-\frac{1}{\Omega}\right) = 0
\end{aligned} \tag{3.12}$$

where $\Delta q = q_\mathrm{min} - 1$. In this case, for which a region of reversed shear exists in the

plasma, fishbones can arise in a continuum gap whereby the damping is eliminated without the need for the ω_{*i} terms [117]. The kinetic drive for fishbones is greater than that for ideal modes (such as the long-lived $n = 1$ internal kink mode (LLM)), this argument is used to explain the transition from the busting, chirping fishbone modes to the LLM upon conception of a $q = 1$ surface in the plasma [117].

3.5 Fishbones in MAST

MAST plasmas exhibit many of the AEs outlined in Section 2.8.1. Tokamak MHD activity is most intuitively displayed by means of a 'spectrograph' which is a sliding Fourier transform of the Mirnov coil signal that detects the instabilities. This provides time-dependent information on the frequency of the instabilities present. A spectrograph from a MAST shot is shown in Figure 3.2(a) for medium frequency modes. Here, TAEs are shown in the frequency range 50kHz $< \omega <$ 300kHz. Another example is shown in Figure 3.2(b), where high frequency CAEs modes are shown in the range 1.5MHz $< \omega <$ 3.5MHz, along with lower frequency TAEs at around $\omega \sim$ 300kHz.

An example of the low frequency activity is shown in Figure 3.3. The low-frequency, bursting, chirping EPMs occur during NBI heating in the time period 0.14s $< t <$ 0.25s, subsequently evolving into a LLM after $t = 0.25$s until the plasma disrupts. These modes generally appear following periods of bursting TAE behaviour. During a MAST shot the q-profile evolves such that $|q_{\min}|$ is steadily falling (the modulus of q is used in order to draw comparisons with the literature, where the q is traditionally a positive value, however due to the definition of the safety factor the value of q on MAST is negative). The chirping modes appear before $|q_{\min}| = 1$, such that there is in fact no $|q| = 1$ surface. In PDX, fishbones are defined as being $n = 1$, $m = 1$ modes radially located on the $q = 1$ surface. Despite this difference in definition, the frequency evolution and mode structure are sufficiently similar such that the MAST Mirnov coils still pick up fishbone-like signatures, therefore to avoid proliferation of terms these modes will be referred to as fishbones. Due to the lack of a $|q| = 1$ surface, the modes are in fact equivalent to that of the 'infernal mode', which is a low-n mode that is driven unstable by the pressure in low-shear plasmas even when standard ballooning theory predicts stability [118]. Fishbones in MAST are typically observed to sweep through the frequency range 40kHz $> \omega >$ 12 kHz in the lab frame.

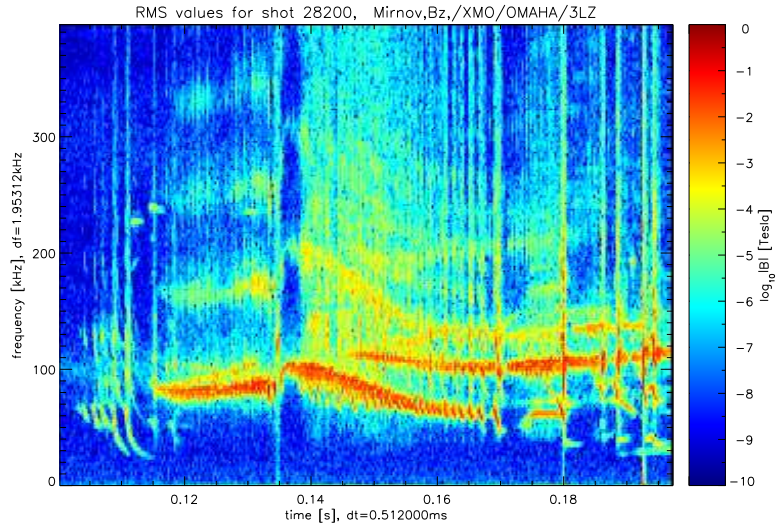

(a) TAEs exist typically with frequency 50kHz< f <300kHz.

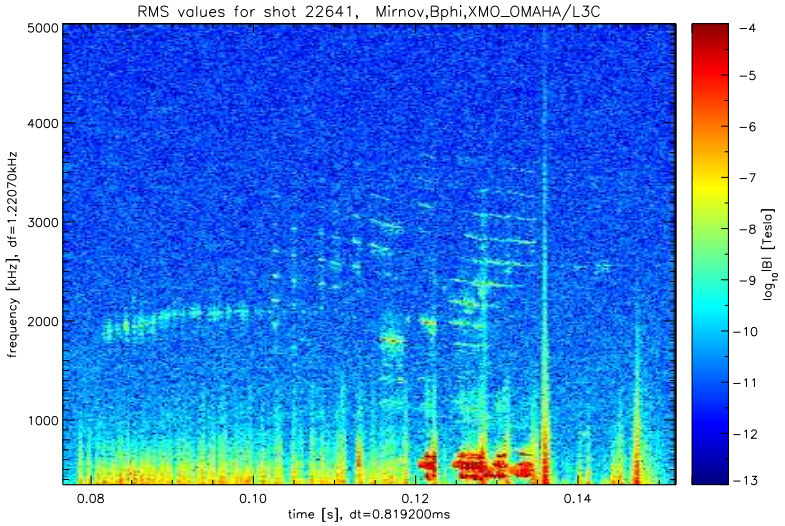

(b) CAEs exist typically with frequency >300kHz. Shown here in the range from 3MHz to 4MHz.

Figure 3.2: Examples of typical MHD activity in MAST in the range from 0-5MHz.

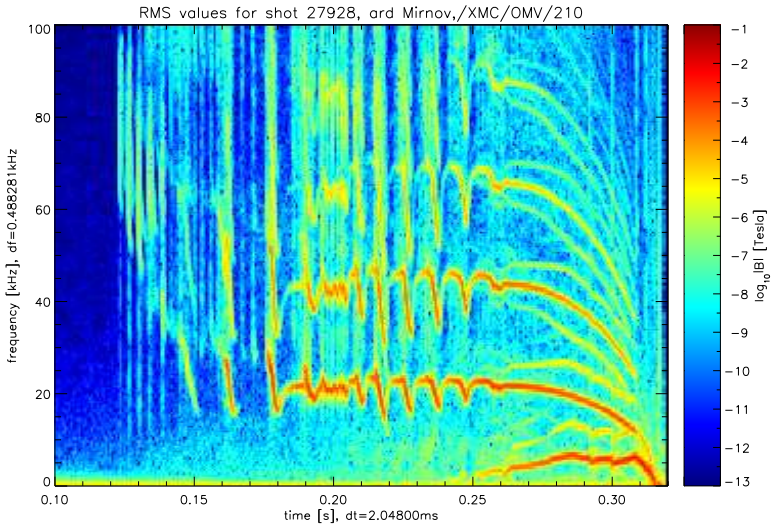

Figure 3.3: Low-frequency kink modes ('fishbones') in MAST typically exist at f <100kHz.

3.6 Dedicated MAST shots

Dedicated MAST shots were carried out during the M9 campaign [119]. The aim of these shots was to study the fishbone modes, allowing us to develop capabilities to better understand the redistribution and loss of fast ions caused by these modes in both MAST and other devices, and to quantify the level of impact that the modes have on tokamak operation. The shots were designed in order to produce large, well spaced, clearly visible fishbone modes. To accurately diagnose changes to the fast ion distribution function, the newly commissioned columnated NC [59] was scanned radially during several shots in order to build up a radial neutron profile. The same was done using the MAST FIDA system.

Stability analysis such as this is often performed experimentally with low density plasmas subject to early NBI heating. Early heating of the plasma in this way results in the plasma resistivity falling, subsequently lengthening the current diffusion time. This means that the inductively driven current takes long enough to diffuse into the core that there is a natural reversed shear (or at least a broad region of week shear) with $|q_{\min}| > 1$ for much of the shot. By increasing the density, a monotonic q-profile can be obtained with $|q| > 1$. The MSE pitch angle diagnostic allows for a temporally and spatially accurate q-profile reconstruction to be made.

The shot was performed in the Double Null Discharge (DND) configuration, which means the plasma has two x-points; one above the axis and one below. The

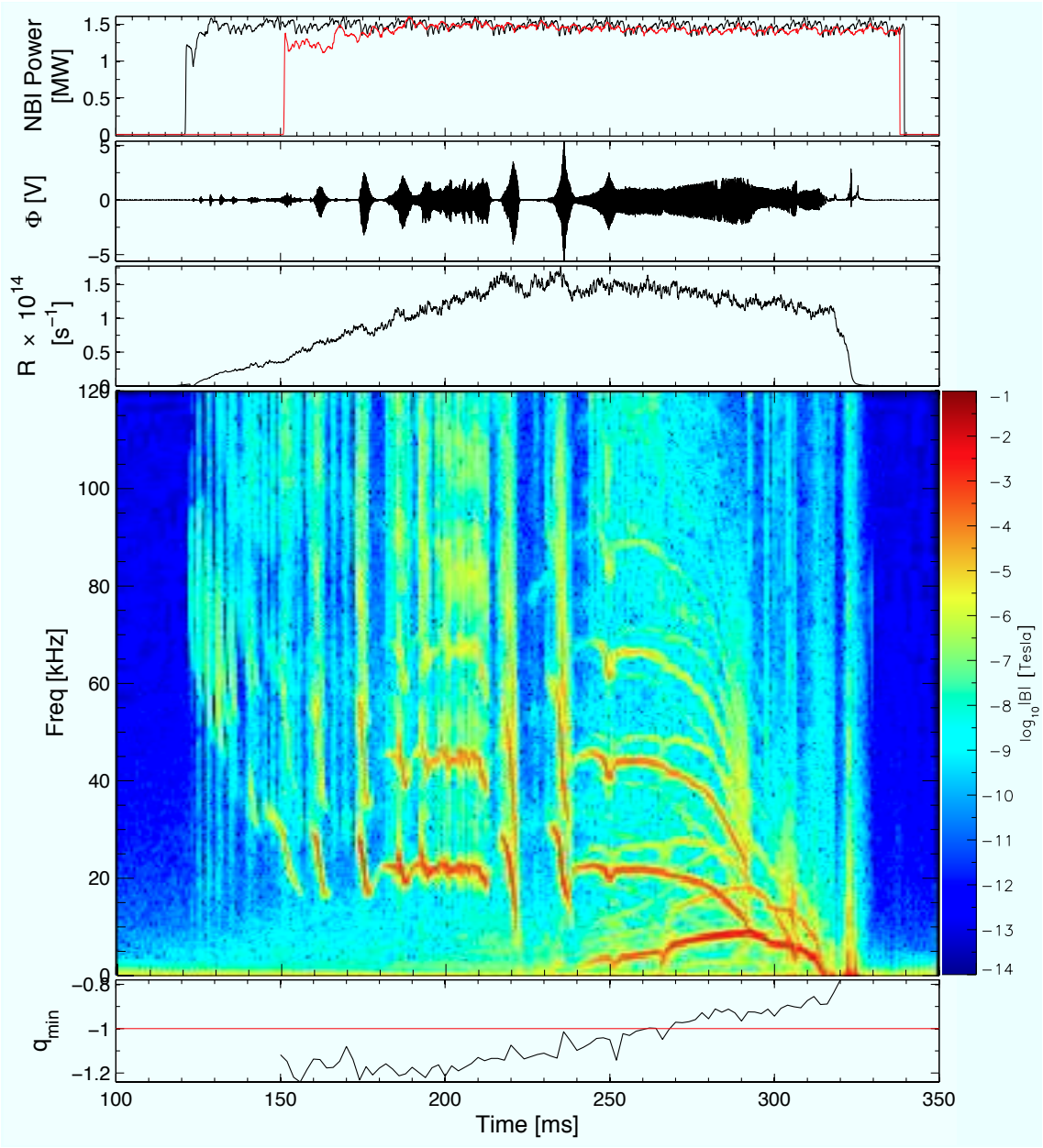

Figure 3.4: Time evolution of shot #27920. (a) NBI power (SS beam in red, SW beam in black), (b) Mirnov coil signal (OMV110) and (c) neutron rate all come from the MAST diagnostics. (d) shows the spectrograph that is a sliding Fourier transform of (b). (e) shows the q_{min} evolution, which comes from the EFIT++ equilibrium reconstruction (see Chapter 5). The value of $|q_{\min}|$ falls throughout the shot, such that a rational $|q| = 1$ surface is established at $t = 260$ms and is shown to coincide with the transition from chirping behaviour into the LLM. The chirping fishbone modes coincide with drops observed in the neutron rate, and a sustained drop is shown during the LLM.

equatorially located NBI beams in MAST mean that in this configuration the neutral atoms are injected on-axis. Although the beams cannot be physically moved in MAST, it is also capable of performing off-axis injection by changing to a Single Null Discharge (SND) configuration (whereby the single x-point can be either above or below the axis). This displacement of the plasma is possible due to the flexibility of the large MAST vessel.

Of the plasma discharges performed, the most suitable for this fishbone study was shot `#27920`. A spectrograph of the MHD activity for this shot is shown in Figure 3.4(d). During the shot, the plasma current ramps up from 200kA to 850kA during the first 200ms where it remains until the shot disrupts at ∼325ms. The toroidal magnetic field was 0.45T. The plasma is heated by 3MW of NBI power; comprising of 1.5MW from each of the two beams shown in Figure 3.4(a). The q-profile is weakly reversed sheared and the temporal evolution of $|q_{\min}|$ is shown in Figure 3.4(e) and $|q_{\min}|$ falls throughout the discharge (the q-profile is calculated during the equilibrium reconstruction in Chapter 5 and shown in Figure 5.3).

During the period of bursting fishbone activity, the small ion pressure near the magnetic axis leads to a small ion diamagnetic frequency $\omega_{*\mathrm{i}}$. In this period it is smaller than the precessional frequency $\omega_\zeta > \omega_{*\mathrm{i}}$ so it is the continuum-type precessional fishbones prescribed by Chen, White and Rosenbluth that are occurring [103]. The evolving q-profile resulting the conception of a $|q| = 1$ surface at $t =$ 250ms in the high pressure gradient region causes a rise in ω_{i*}. At this point, the LLM 'locks in', and the chirping fishbones cease. The rise in ω_{i*} has lead to the suggestion [110] that the LLM initiation is in fact a transition to the diamagnetic fishbones of Coppi and Porcelli [106], although as explained in Section 3.4 it may be alternatively be attributed to the fact that less kinetic drive is required for the LLM as this is a reverse-sheared plasma [117], as prescribed in Equation 3.12, such that the mode drive from the fast ions can overcome the continuum damping. If the q-profile subsequently returns to having $|q_{\min}| > 1$, the LLM ceases and the chirping fishbone modes resume; this effect has been shown more prominently on other shots, but appears transiently at $t = 260$ms in this shot for ~ 5ms.

The focus of this thesis is the fishbone that occurs in shot `#27920` at 0.2327s $< t <$ 0.2386s which is of the precessional type. It has a duration of 5.9ms and has a frequency in the lab frame of $\omega(t = 0.2327\mathrm{s}) = 30$kHz sweeping down to $\omega(t = 0.2386\mathrm{s}) = 16$kHz with a sweeping rate of $\mathrm{d}\omega/\mathrm{d}t = 2.7119{\times}10^3$ kHz/s.

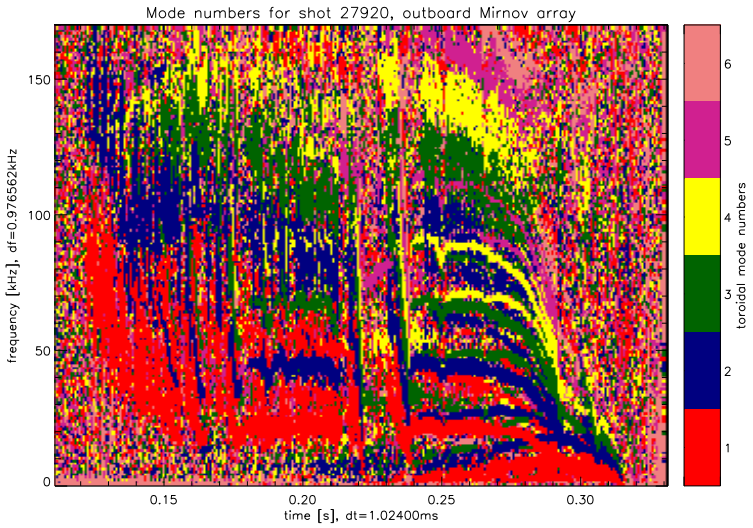

Figure 3.5: Mode number analysis for shot #27920 for $1 \leqslant n \leqslant 6$.

3.6.1 Mode Number Analysis

The spectrograph for this shot (Figure 3.4(d)) simultaneously shows multiple fishbone resonances occurring at each time during the chirping mode region, as well as during the LLM. To better understand what is causing this, mode number analysis has been performed. The multiple toroidal locations of the OMV coils mean it is possible to resolve the toroidal mode number of the internal kink mode (examples of kink modes are shown in Figure 2.3).

The mode number analysis has been carried out, as shown in Figure 3.5. Toroidal mode harmonics are shown to exist for $1 \leqslant n \leqslant 6$. It is understood that the observed modes with $n > 1$ are in fact nonlinear effects associated with the $n = 1$ mode [120]. When modelling the fishbone, it is possible however to interpret these nonlinear effects to be distinct, each represented by an independent mode eigenfunction. This treatment has previously been applied during a study of the LLM [117], and similarly (again in the case of saturated modes) in [121].

In the case of the fishbones that make the focus of this theses, it is necessary to make the following assumptions:

(a) Although nonlinear effects of the same mode, for the sake of modelling they will be treated as separate linear instabilities.

(b) This is a suitable approach considering the short ($\sim$ 5ms) duration of the modes, such that a summation of linear effects are equivalent to the single nonlinear

mode.

(c) The different modes decay equivalently out of the plasma to the location of the Mirnov coil in which the magnetic perturbation is diagnosed.

Another potential interpretation for the observed presence of these higher harmonics suggest a similar structure to the 'snake' MHD mode, comprising of a narrow rotating current filament [122]. In analogy to snake modes, it is possible that the higher n harmonics are due to the creation of a current filament during the nonlinear phase of the fishbone development [110].

The frequencies of the toroidal harmonics in the lab frame are linked, with each of the $n > 1$ harmonics $n\times$ the frequency of the $n = 1$ mode,

$$\omega_{k,\mathrm{lab}} \sim n\ \omega_{k=1,\mathrm{lab}}\ .$$

Although it is difficult to determine from the spectrograph, it is likely that there is an additional term on the right hand side of this equation $\sim \omega_{*\mathrm{i}}$. This is due to the internal frequency of the mode, which would be more apparent in the absence of plasma rotation.

3.6.2 Relative Toroidal Mode Amplitudes

In order to model the nonlinear $n = 1$ mode behaviour observed as multiple toroidal resonances in the spectrograph for shot `#27920` as independent linear mode eigenfunctions according to the assumptions above, it is necessary to determine the relative mode amplitudes of each n harmonic. This can be done by taking the Fourier transform of the perturbation signal measured by the OMV coil, which measures a voltage $V \propto \partial\delta\mathbf{B}/\partial t$. The sizes of the perturbations relative to each other can be estimated from the Mirnov coil signal using

$$\delta\mathbf{B} \sim \frac{\partial\delta\mathbf{B}}{\partial t}\frac{1}{\omega}\ . \tag{3.13}$$

The Mirnov coil signal for the fishbone studied is shown in Figure 3.6(a)(i). For each time, the Fourier transform is taken in order to see what frequency components are present. The amplitudes of the components present at several time points is calculated using Equation 3.13 and plotted in Figure 3.6(b). By taking the peak amplitude associated with each $n > 1$ harmonic in this figure and dividing it by the peak mode amplitude of the $n = 1$ harmonic, the relative mode amplitude of the higher harmonics is determined. Ignoring the first time point (when the Mirnov coil signal is insignificant), it is shown that throughout the burst the relative fraction

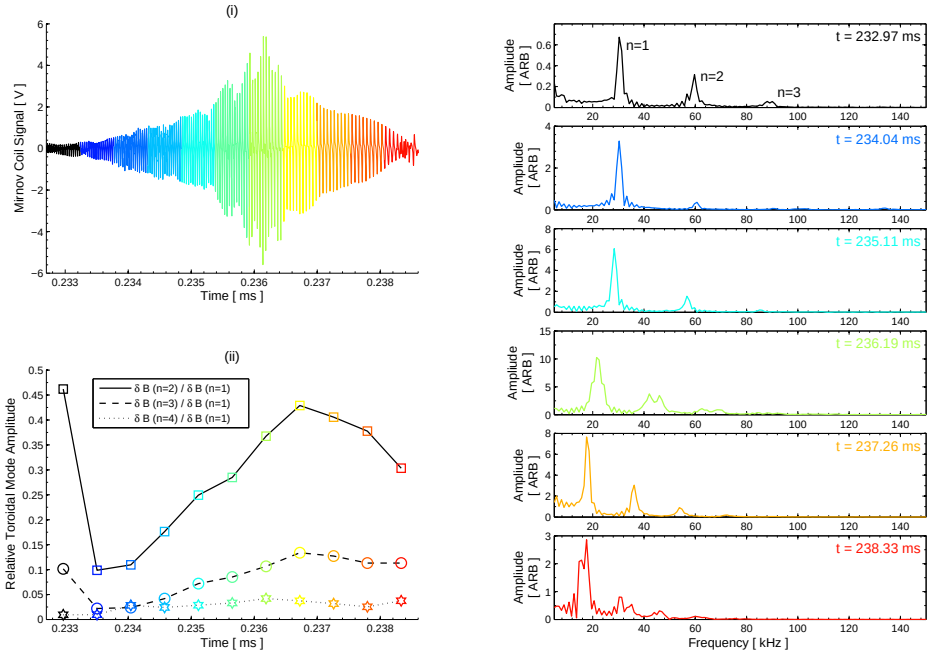

(a) (i) Mirnov coil signal, split into times (b) Relative magnitudes of the δB for each n (shown by different colours). (ii) Amplitude harmonic of the mode at different times during of $n = 2, 3, 4$ modes as a fraction of the $n = 1$ the burst.
mode amplitude throughout the burst.

Figure 3.6: Determination of relative contribution from each toroidal mode number during the fishbone.

of the $n > 1$ modes increases until just after the mode saturates, before decreasing again. Analogy may be drawn with the increasing relative amplitude of the $n = 2$ mode found for the LLM in [117], albeit the two are on disparate timescales.

It is shown that at its peak the $n = 2$ harmonic reaches an amplitude of 43% that of the $n = 1$, with the $n = 3$ and $n = 4$ harmonics peaking at 13% and 4% respectively.

3.6.3 Mode Direction Analysis

It is necessary to determine the direction of travel of the internal kink responsible for the observed fishbones. This is done by using the sign of the toroidal mode number, defining whether it is a $n = 1$ or $n = -1$ mode. The mode number analysis performed in Figure 3.5 measures the mode to be $n = +1$. This is confirmed by looking at the magnetic perturbation signal detected by different Mirnov coils at a range of toroidal locations. The mode moves in the same direction as the NBI particles are injected (which it must do as it is driven by the beam fast ion population) which in MAST is co-parallel to the I_p and anti-parallel to the toroidal magnetic field B_t (see Table A.1). This results in a negative q-profile in MAST and means that for these modes the poloidal mode number is negative since $m \sim nq$. The dominant mode for the fishbone in MAST that is studied is therefore $n = 1$, $m = -1$. The beam-injected particles have $\lambda = \mathbf{v}.\mathbf{B}/vB < 0$ but are referred to as 'co-passing' since the definition of co- and counter-passing is with respect to the toroidal current I_p.

3.6.4 Scaling of Fast Ion Redistribution with Mode Amplitude

The amplitude of the mode is proportional to the amplitude of the signal detected in the Mirnov coil (Equation 3.13). Figure 3.7(a) shows the magnitude of the drop in total neutron rate detected from the plasma against the perturbation amplitude detected by the Mirnov coil, and Figure 3.7(b) shows this as a fraction of the neutron rate at that time. It can be seen that these fishbone events typically account for a drop in the detected neutron rate of the order of ∼10-15%, but the largest fishbone shows a drop in the total neutron rate of more than 20%. The neutron rate drops because the fast ions are redistributed away from the hot core, some of which are even lost from the plasma altogether.

Figure 3.7(a) shows a strong linear trend that does not pass through the origin. The implication from this is that there is a threshold that must be surpassed in order to excite fishbone activity. Once the EP drive is sufficient, this threshold is

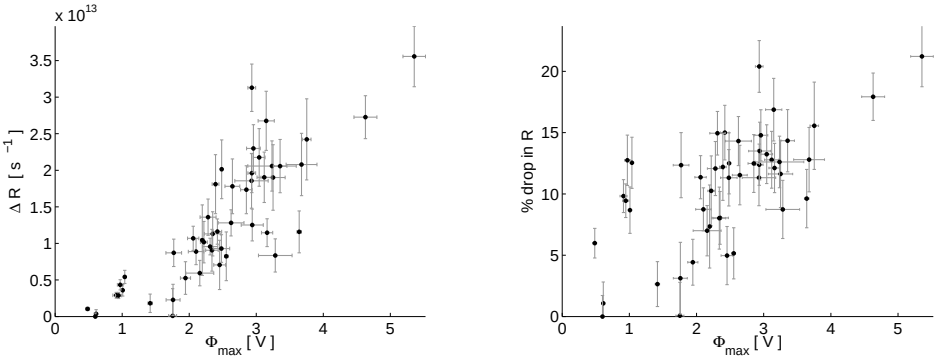

(a) Drop in neutron rate against mode amplitude.

(b) Percentage drop in neutron rate against mode amplitude.

Figure 3.7: Drop in neutron rate detected by the fission chamber against the magnitude of the mode in volts detected by the Mirnov coil. The figure comprises of all the fishbone events occurring in shots: #26786 #26787 #26788 #26789 #26790 #26791 #27920 #27926 #27927 #27928.

overcome and the mode is destabilised, redistributing the fast ions (seen by a drop in the observed neutron rate). A similar mode amplitude threshold has recently been observed in the case of TAE avalanche modes in NSTX [85].

3.7 Summary

The fishbone mode has been explained in detail, from its initial identification to how it manifests itself in present day plasmas and its potential to have detrimental effects on future devices. The stability of fishbones has been explained by means of a dispersion relation. Experiments have been performed on MAST which provide information to enable us to better understand the instability, which has been identified as a interaction between fast ions and an $n = 1$, $m = -1$ kink mode. The data that has been taken experimentally is interpreted by means of computational modelling, the results of which are explained in the following chapters.

Chapter 4

Development of Model

An accurate numerical model is required to study the effect of fishbones in MAST. The code that has been chosen to do so is HAMILTONIAN GUIDING CENTRE SYSTEM (HAGIS), a nonlinear drift-kinetic δf code developed to study wave-particle interactions in tokamak plasmas [65, 74]. It uses the guiding centre Hamiltonian approach set out in Section 2.6 to evolve an EP population in response to an MHD instability.

4.1 The HAGIS code

The HAGIS system uses N_j simulation 'markers' to represent N_p particles in the plasma. The code solves $4 \times N_j$ ordinary differential equations (found in Section 2.6.1) that represent the energetic particles, in conjunction with $2 \times N_\mathrm{w}$ ordinary differential equations that evolve the N_w waves in the system that are used to represent the mode. The equations that govern the wave evolution in addition to those that determine the interaction with the particles are given in Section 4.1.3. The equations are solved within the straight field line coordinate system prescribed by Boozer that was explained in Section 2.5.1.

4.1.1 Phase Space

In HAGIS, the physical phase space $\Gamma^{(p)}$ is divided up into spatial and velocity components. Integrals of this phase space are subsequently performed with respect to an infinitesimally small physical phase space volume element $\mathrm{d}\Gamma^{(p)}$, the product of the spatial element d^3x and the velocity element d^3v,

$$\mathrm{d}\Gamma^{(p)} \equiv \mathrm{d}^3x \; \mathrm{d}^3v \; . \tag{4.1}$$

In cartesian space (x, y, z), the phase space volume element is elementary,

$$\mathrm{d}\Gamma^{(p)} \equiv \mathrm{d}x\ \mathrm{d}y\ \mathrm{d}z\ \mathrm{d}v_x\ \mathrm{d}v_y\ \mathrm{d}v_z\ . \tag{4.2}$$

An analogous form is required in terms of the Boozer coordinates defined in Section 2.5.1. In order to do this, it is necessary to define the velocity components with respect to the direction on the magnetic field $\mathbf{B}$,

$$v_\parallel = \frac{\mathbf{v}\cdot\mathbf{B}}{B} \qquad\qquad v_\perp = \sqrt{v^2 - v_\parallel^2}$$

such that $v^2 = v_\parallel^2 + v_\perp^2$. The angle between the velocity vector and the magnetic field direction is the polar angle θ_v, given in Equation 2.14. The angle between the projection of the velocity vector onto the perpendicular plane and the axis is known as the azimuthal angle φ_v. The velocity phase space element is therefore given by

$$\begin{aligned}
\mathrm{d}^3v &= \mathrm{d}v\ \ (v\ \mathrm{d}\theta_v)\,(v\sin\theta_v\ \mathrm{d}\varphi_v) \\
&= \int_0^{2\pi} v^2\ \mathrm{d}v\ \mathrm{d}\lambda\ \mathrm{d}\varphi_v \\
&= 2\pi v^2\ \mathrm{d}v\ \mathrm{d}\lambda
\end{aligned}$$

where the final step was made by integrating over the azimuthal angle, $\int_0^{2\pi}\mathrm{d}\varphi_v = 2\pi$. This is possible since only the magnitude of the azimuthal angle is required (not the direction), as here it is a Cherenkov-type resonance between the wave and the fast ion and not a gyro-resonance effect that is studied. The spatial phase space volume element in Boozer coordinates is given by

$$\mathrm{d}^3x = \mathcal{J}\ \mathrm{d}\psi_p\ \mathrm{d}\theta\ \mathrm{d}\zeta\ , \tag{4.3}$$

where $\mathcal{J}$ is the Boozer coordinates' Jacobian given in Equation 2.51. The phase space volume element found using Equation 4.1 is therefore

$$\mathrm{d}\Gamma^{(p)} = 2\pi v^2 \mathrm{d}v\ \mathrm{d}\lambda\ \mathcal{J}\ \mathrm{d}\psi_p\ \mathrm{d}\theta\ \mathrm{d}\zeta\ . \tag{4.4}$$

The element of phase space represented by each simulation marker is subject to change throughout the run as it traverses the plasma. It is required during the simulation in order to perform integrals, for example to find the number of markers N_p or the total energy $\mathcal{E}_{\mathrm{tot}}$ of the system,

$$N_p = \int f \, \mathrm{d}\Gamma^{(p)} = \sum_{j=1}^{N_j} f_j \, \mathrm{d}\Gamma_j^{(p)} \, , \tag{4.5}$$

$$\mathcal{E}_{\mathrm{tot}} = \int f \, \mathcal{E} \, \mathrm{d}\Gamma^{(p)} = \sum_{j=1}^{N_j} f_j \, \mathcal{E}_j \, \mathrm{d}\Gamma_j^{(p)} \, .$$

Since a set of canonical coordinates is used, the physical phase space element is defined from the canonical phase space element. The canonical phase space element is defined in terms of the canonical variables (ξ, θ, ζ) as

$$\mathrm{d}\Gamma_c^{(c)} \equiv \mathrm{d}\xi \, \mathrm{d}P_\xi \, \mathrm{d}\theta \, \mathrm{d}P_\theta \, \mathrm{d}\zeta \, \mathrm{d}P_\zeta \, .$$

We know from Equation 2.57c that $P_\xi = \mu$, and by integrating over the gyro-phase ξ the canonical phase space volume element may be re-written as

$$\mathrm{d}\Gamma^{(c)} \equiv 2\pi \, \mathrm{d}\mu \, \mathrm{d}\theta \, \mathrm{d}\zeta \, \mathrm{d}P_\theta \, \mathrm{d}P_\zeta \, . \tag{4.6}$$

The two phase space volume elements are related via another Jacobian required to convert from canonical to physical space $\mathcal{J}^{(pc)}$,

$$\mathrm{d}\Gamma^{(p)} = \mathcal{J}^{(pc)} \, \mathrm{d}\Gamma^{(c)}$$

which is derived in [65] as

$$\mathcal{J}^{(pc)} = \frac{\mathcal{J} B^2}{D}$$

where

$$D = \rho_{\|} \left[g I' - g' I \right] + I + q g \, .$$

In HAGIS, the markers can be loaded in a uniform phase-space $\mathcal{U}$. Each one of the N_j markers (represented by subscript j) is loaded such that it represents an element of this uniform phase space $\Delta\mathcal{U}_j$ chosen to be

$$\Delta\mathcal{U}_j = \frac{\int \mathrm{d}\mathcal{U}}{N_j} \, ,$$

where the uniform phase-space volume element is chosen to be

$$\mathrm{d}\mathcal{U} = \mathrm{d}v \, \mathrm{d}\lambda \, \mathrm{d}s \, \mathrm{d}\theta \, \mathrm{d}\zeta \, .$$

Here,

$$s = \sqrt{\frac{\psi_p - \psi_{p,0}}{\psi_p(a) - \psi_{p,0}}}$$

is the square root of the normalised radial flux ($\psi_p(a)$ and $\psi_{p,0}$ represent the poloidal flux at the edge of the plasma and on axis respectively), which is used as a radial coordinate that runs from zero in the core to one at the plasma edge. The uniform phase space volume element in HAGIS is found from the canonical phase space volume element via a further Jacobian $\mathcal{J}^{(cu)}$. Upon loading the markers at $t = t_0$, the volume of the physical phase space represented by a single marker j is given by

$$\Delta\Gamma_j^{(p)} \equiv \mathcal{J}^{(pc)}\mathcal{J}^{(cu)}\Delta\mathcal{U} \ .$$

For this reason, it is not computationally possible to subsequently separate the physical phase space element into its composite physical space and velocity space elements. A detailed explanation of the subtleties associated in loading the uniform phase space in order to accurately represent the particle distribution using Monte-Carlo methods is provided in [65].

4.1.2 HAGIS Representation of Perturbed Wave Field

The perturbed fields are modelled in HAGIS by means of a perturbed scalar potential $\tilde{\Phi}$ and a perturbed vector potential $\tilde{A}$, defined through a variable $\tilde{\alpha}$ (via the constraint $\tilde{\mathbf{B}}_{\parallel} = 0$ which allows only shear Alfvén waves to be studied) as $\tilde{A} = \tilde{\alpha}\mathbf{B}$. From this, the resulting perturbation to the magnetic field is $\tilde{\mathbf{B}} = \boldsymbol{\nabla} \times (\tilde{\alpha}\mathbf{B}_0)$. Each wave is characterised by a distinct toroidal eigenfunction (index k) and represented by a sum of poloidal harmonics m, such that

$$\tilde{\Phi}_k = \sum_m \tilde{\phi}_{km}(\psi_p)\mathrm{e}^{i(\mathbf{k}_{km}.\mathbf{x} - \omega_k t)} \tag{4.7}$$

where $\tilde{\phi}_{km}$ represents the eigenfunctions read in from the linear stability analysis (for example radial mode eigenfunctions found using the MISHKA code), and may be a complex quantity representing phase information between the relative harmonics. For a wave vector $\mathbf{k}_{km} = n_k\boldsymbol{\nabla}\zeta - m\boldsymbol{\nabla}\theta$, Equation 4.7 may be written as a sum over the poloidal and toroidal Fourier harmonics as

$$\tilde{\Phi}_k\left(\psi_p, \theta, \zeta, t\right) = \sum_m \tilde{\phi}_{km}(\psi_p)\mathrm{e}^{i(n_k\zeta - m\theta - \omega_k t)} \ . \tag{4.8}$$

and a similar relation for the perturbation parameter $\tilde{\alpha}_k$ given by

$$\tilde{\alpha}_k\left(\psi_p,\theta,\zeta,t\right)=\sum_m \tilde{\alpha}_{km}(\psi_p)\mathrm{e}^{i(n_k\zeta-m\theta-\omega_k t)}\ . \tag{4.9}$$

The electric field is

$$E_k=-\boldsymbol{\nabla}\tilde{\Phi}_k-\frac{\partial \tilde{A}_k}{\partial t}\ ,$$

the parallel component of which is

$$E_{\parallel,k}=-\boldsymbol{\nabla}_\parallel\tilde{\Phi}_k-\frac{\partial}{\partial t}\left(\tilde{\alpha}_k B_0\right)\ . \tag{4.10}$$

Ideal MHD is enforced in this model, which allows the constraint that $E_{\parallel,k}=0$ to be employed (this would not be the case in a resistive or gyrokinetic code). Doing so enables a relationship to be found for the perturbation parameter $\tilde{\alpha}_{km}$ from the scalar potential $\tilde{\Phi}_{km}$. By substituting Equation 4.8 and Equation 4.9 into Equation 4.10 one finds the relation to be

$$\begin{aligned}
\boldsymbol{\nabla}_\parallel\tilde{\Phi}_k &= -\frac{\partial}{\partial t}\left(\tilde{\alpha}_{km}B_0\right)\\
k_{\parallel,m}\sum_m\tilde{\phi}_{km}\mathrm{e}^{i(n_k\zeta-m\theta-\omega_k t)} &= \omega_k B_0\sum_m\tilde{\alpha}_{km}\mathrm{e}^{i(n_k\zeta-m\theta-\omega_k t)}\\
\tilde{\alpha}_{km} &= \frac{k_{\parallel m}\tilde{\phi}_{km}}{\omega_k B_0}\ .
\end{aligned} \tag{4.11}$$

4.1.3 Wave Particle Interaction

The system of N_w waves interacting with N_p particles modelled using the HAGIS code is modelled by means of a Lagrangian approach. The total system Lagrangian $\mathcal{L}$ is composed of four parts: the fast particle Lagrangian $\mathcal{L}_{\mathrm{fp}}$, which represents the motion of the population of fast ions as they traverse the equilibrium wave field; the interaction Lagrangian $\mathcal{L}_{\mathrm{int}}$ determined by the interaction of the waves with the resonant part of the distribution function; the background (bulk) contribution to the Alfvén waves $\mathcal{L}_{\mathrm{bulk}}$; and the electromagnetic contribution $\mathcal{L}_{\mathrm{em}}$,

$$\mathcal{L}=\underbrace{\mathcal{L}_{\mathrm{fp}}+\mathcal{L}_{\mathrm{int}}}_{\mathcal{L}_{\mathrm{p}}}+\underbrace{\mathcal{L}_{\mathrm{bulk}}+\mathcal{L}_{\mathrm{em}}}_{\mathcal{L}_{\mathrm{w}}}. \tag{4.12}$$

Detailed explanation and derivation of the above Lagrangian is available in [65] and [74]. The particle Lagrangian $\mathcal{L}_{\mathrm{p}}$ is given by Equation 2.54 and the wave Lagrangian

$\mathcal{L}_{\rm w}$ comprises of the following [123]

$$\mathcal{L}_{\rm w} = \sum_k \frac{E_k}{\omega_k} \left[A_k^2 \dot{\sigma}_k \right] \ , \tag{4.13}$$

where E_k, referred to as the 'wave energy' is equal to

$$E_k = \frac{1}{2\mu_0} \int_V \frac{\left| \boldsymbol{\nabla}_\perp \tilde{\phi}_k \right|^2}{v_A^2} \ \mathrm{d}^3 x \ . \tag{4.14}$$

From the above it is possible to find the mode amplitude and phase of the k^{th} wave, A_k and σ_k respectively. It is however numerically favourable to do so in an alternative way, by introducing two new variables to represent the real and imaginary parts of the wave, such that

$$A_k(t) e^{-i\sigma_k(t)} = \mathcal{X}_k(t) - i \ \mathcal{Y}_k(t). \tag{4.15}$$

From this, the scalar potential at the location of the j^{th} particle is written as a sum over each of the m poloidal harmonics of the k waves as

$$\tilde{\Phi}_j = \sum_{k=1}^{N_w} \sum_m \left[\mathcal{X}_k(t) C_{jkm} + \mathcal{Y}_k(t) S_{jkm} \right] \ , \tag{4.16}$$

and it follows from Equation 4.11 that the magnetic perturbation parameter at that location is

$$\tilde{\alpha}_k = \frac{1}{B_0} \sum_{k=1}^{N_w} \frac{1}{\omega_k} \sum_m \left[\mathcal{X}_k(t) C_{jkm} + \mathcal{Y}_k(t) S_{jkm} \right] \tag{4.17}$$

where two further quantities have been introduced

$$\begin{aligned} C_{jkm} &\equiv \mathbb{R}\mathrm{e} \left[\tilde{\phi}_{km}(\psi_{p,j}) \ e^{i\Theta_{jkm}} \right] \ , \\ S_{jkm} &\equiv \mathbb{I}\mathrm{m} \left[\tilde{\phi}_{km}(\psi_{p,j}) \ e^{i\Theta_{jkm}} \right] \ , \end{aligned}$$

where

$$\Theta = n_k \zeta_j - m\theta_j - \omega_k t \ . \tag{4.18}$$

The interaction Lagrangian evaluated at the location of the j^{th} particle is

$$\begin{aligned}\mathcal{L}_{\text{int}} &= \sum_{j=1}^{N_j}\left(\tilde{\mathbf{A}}_j\cdot\mathbf{v}_j-\tilde{\Phi}_j\right)\\ &= \sum_{j=1}^{N_j}\sum_{k=1}^{N_w}\frac{1}{\omega_k}\sum_m\left(k_{\|m}v_{\|j}-\omega_k\right)\left[\mathcal{X}_kC_{jkm}+\mathcal{Y}_kS_{jkm}\right],\end{aligned}$$

subsequently allowing the total system Lagrangian $\mathcal{L}=\mathcal{L}_{\text{w}}+\mathcal{L}_{\text{int}}$ to be written as

$$\mathcal{L}=\sum_{k=1}^{N_w}\frac{1}{\omega_k}\left[\sum_{j=1}^{N_j}\sum_m\left(k_{\|m}v_{\|j}-\omega_k\right)\left[\mathcal{X}_kC_{jkm}+\mathcal{Y}_kS_{jkm}\right]+E_k\left[\mathcal{X}_k\dot{\mathcal{Y}}_k-\cdot\mathcal{X}_k\mathcal{Y}_k\right]\right].$$

The resulting pair of differential equations that need to be solved to describe the wave evolution are therefore

$$\begin{aligned}\dot{\mathcal{X}}_k &= \frac{1}{2E_k}\sum_{j=1}^{N_j}\sum_m\left(k_{\|m}v_{\|j}-\omega_k\right)S_{jkm}\ ,\\ \dot{\mathcal{Y}}_k &= -\frac{1}{2E_k}\sum_{j=1}^{N_j}\sum_m\left(k_{\|m}v_{\|j}-\omega_k\right)C_{jkm}\ .\end{aligned}$$

4.1.4 Particle Distributions

It is necessary to find a technique to represent the distribution of particles in the plasma. The location of each fast ion, along with its velocity must be recorded. Storing the precise location and velocity of $\sim 10^{18}$ particles is not feasible, so a distribution function is used which represents the density at each point in phase space and can be sampled to find the number of particles and their energy at that location.

$$f_0=f_0(x,y,z;v_x,v_y,v_z) \tag{4.19}$$

There is however a more efficient method of storing the distribution function. Throughout an unperturbed orbit, each fast ion retains three constants of motion outlined in Chapter 2, ($\mathcal{E}^{(0)}=\mathcal{E}-\tilde{\Phi}$, $P_\zeta^{(0)}=P_\zeta-\tilde{\alpha}g$ and μ). For this reason, the distribution function can be represented by these, along with $\sigma_d=v_\|/\left|v_\|\right|$ to resolve the degeneracies of which direction a fast ion is travelling in at a certain location in phase space. The unperturbed distribution function can therefore be fully represented in the form

$$f_0=f_0(\mathcal{E}^{(0)},P_\zeta^{(0)},\mu,\sigma_d)\ . \tag{4.20}$$

4.1.5 The δf Method

The HAGIS code solves the aforementioned set of differential equations for the particles (Equations 2.61a, 2.61b, 2.62a and 2.62b) and the waves (Equations 4.19 and 4.19). As the particles traverse the six dimensional phase space, they interact with the waves in a self-consistent manner. It is obviously computationally advantageous to reduce the number of particles that need to be followed in the simulation. For this reason, a technique is required to limit the number of particles that must be followed. HAGIS employs the 'δf' method [124], an algorithm first conceived by Tajima and Perkins [125] which is now common in not just fast particle codes like HAGIS but also local (e.g. GS2, [126]) and global (e.g. NEMORB, [127]) gyrokinetic codes.

The δf approach is to split the distribution function f into an unperturbed, time independent background distribution function f_0 and a time dependent perturbation to this, δf. It is the perturbation that is represented by the N_j discrete weighted markers, each of which represents a part of the phase space. The markers are loaded to have different weights, therefore representing different numbers of real-life particles.

$$f = f_0 + \delta f \tag{4.21}$$

This separation makes no assumptions regarding the size of the perturbation - it does not require $\delta f \ll f_0$, however this is the case in which the most significant reduction in noise is expected. The noise in the system is reduced by using the δf method of the order $|\delta f/f|^2$ [128]. The system is evolved in time by differentiating Equation 4.21,

$$\dot{f} = \dot{f_0} + \dot{\delta f}$$

with no sources or sinks in the system $\dot{f} = 0$. For a distribution function of fast ions that are quantified by their CoM, the following kinetic equation is found for $\dot{\delta f}$,

$$\begin{aligned} \dot{\delta f} &= -\dot{f_0} \\ &= -\dot{\mathcal{E}^{(0)}}\frac{\partial f_0}{\partial \mathcal{E}^{(0)}} - \dot{P_\zeta^{(0)}}\frac{\partial f_0}{\partial P_\zeta^{(0)}} - \dot{\mu}\frac{\partial f_0}{\partial \mu} \, . \end{aligned} \tag{4.22}$$

If no waves are present in the system, $\dot{\mu}$, $\dot{P_\zeta^{(0)}}$ and $\dot{\mathcal{E}^{(0)}}$ remain constant, thus f remains constant. Also, setting $f_0 = f$ reverts the simulation to a conventional (non-δf) form, with fixed marker weight δf=0.

4.2 Orbit Classification

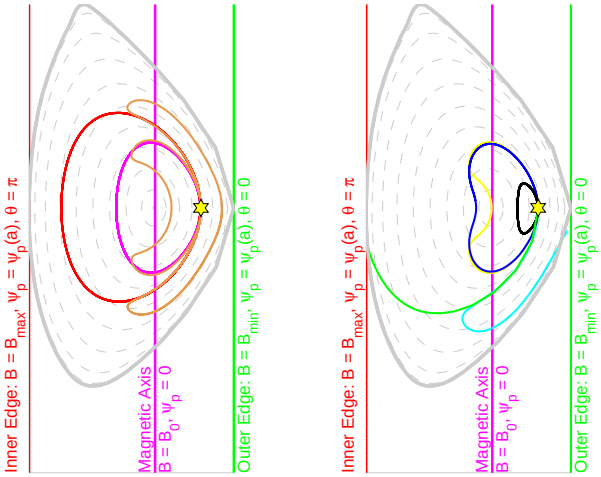

Figure 4.1: Examples of fast particle orbits in fusion plasmas (the plots are equivalent, but have been separated into two figures for clarity).

The properties that define the fast ion guiding centre orbits allows for them to be naturally segregated into various orbit classifications. These classifications are determined by the energy, pitch angle and location of the particle in question. The poloidal projection of several examples of fast particle orbits launched at the same location in the plasma (denoted by the yellow star) is shown in Figure 4.1. Passing orbits encircle the magnetic axis and complete full orbits without changing direction. Examples are shown for co-passing and counter-passing orbits by the magenta and red lines respectively. The terms 'co-' and 'counter-' passing are defined with respect to the plasma current I_p and not the magnetic field B, hence in MAST co-passing particles have $\sigma_d = -1$ and counter-passing particles therefore have $\sigma_d = +1$.

Trapped particles experience the magnetic mirror effect, causing them to change direction as they approach the HFS of the plasma (denoted by a change in the sign of $\dot{\theta}$ during their orbit). Particle drifts result in a finite orbit with, such that these particles being referred to as having 'banana' orbits. Particles with banana orbits do not encircle the magnetic axis, and examples are shown by the orange lines (for co- and counter- launched particles). Low energy particles fall exclusively into the classification of either trapped or passing, but higher energy ions have more exotic orbits.

A species of orbit exists that experiences a bounce point but does also encircle

the axis - this is known as a 'potato' (or 'bean') orbit, and is shown by the blue trajectory in Figure 4.1. The transition from banana to potato is when the orbit intersects the magnetic axis, shown by the yellow trajectory. Both trapped and passing particles can posses sufficient energy such that their orbit is not confined by the field, causing them to become 'lost' from the plasma. Examples of lost orbit trajectories are shown for trapped and passing particles by the cyan and green lines respectively. A further class of orbit exists that is passing but does not encircle the axis; these are referred to as 'stagnation' orbits, shown by the black line. A 'true' stagnation orbit traverses the plasma at all times parallel to the magnetic axis, and subsequently in this poloidal projection is hidden beneath the yellow star for its entire trajectory.

4.3 Constants of Motion Phase Space

By defining each particle by its CoM, a three-dimensional CoM phase space can be considered (with a fourth dimension σ_d required to distinguish between the direction of travel in degenerate regions where more than one orbit exists with a certain $\mathcal{E}$, P_ζ, μ). This phase space can subsequently be divided by topological boundaries into different types of orbits. The boundaries are surfaces in the three dimensional phase space, whereby orbits on each side fall under different orbit classifications. These are crucial, and the crossing of these boundaries represents the transition to a different orbit type or even to a region where they will no longer be confined by the plasma and are lost altogether, as defined by the second type of fast particle transport explained in Section 2.7.4.

Region	**Orbits**
A	Trapped
B	Co-Passing
C	Counter-Passing
D	Counter-Passing (Lost)
E	Trapped (Lost)
F	Co-Passing (Lost)
G	Stagnation
H	Potato
I	Co-Passing & Counter-Passing

Table 4.1: Fast particle orbit classifications.

A slice at constant energy of such a CoM phase-space diagram is shown in Figure 4.2. Regions can be seen where the fourth dimension σ_d is required to resolve

degeneracy, for example the trapped region where at any point in time the particles could be travelling along the direction of the plasma current I_p or in the opposite direction to it depending upon their location within a bounce.

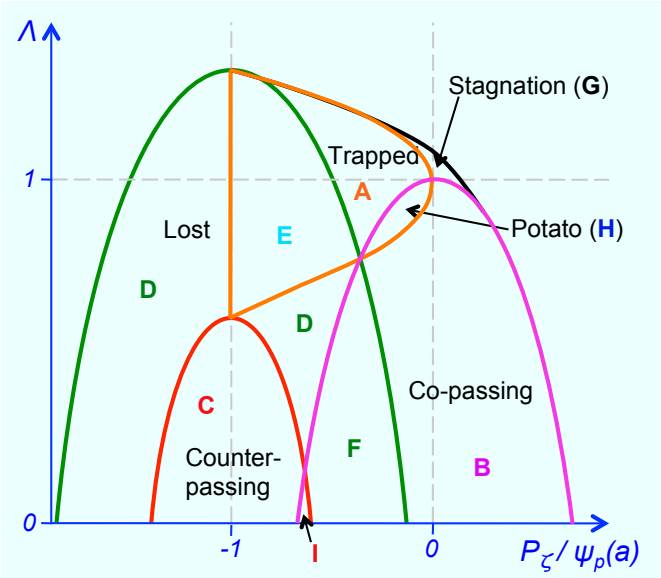

Figure 4.2: CoM phase space schematic. The constants of motion are ($\mathcal{E}$, P_ζ, μ), but to simplify the figure it is normalised such that the y-axis is $\Lambda = \mu B_0/\mathcal{E}$. The third dimension is $\mathcal{E}$, hence this figure is a 'slice' through the phase space at a constant energy. Orbit classifications are separated by the coloured lines.

The different regions describe the type of orbit phenomenology of the particles contained within it, separated by the coloured topological boundaries described below. The energy for any particle orbit may be written in the form

$$\begin{aligned} \mathcal{E} = \frac{1}{2}mv^2 &= \frac{1}{2}mv_\parallel^2 + \frac{1}{2}mv_\perp^2 \\ &= \frac{1}{2}m\rho_\parallel^2\omega_c^2 + \mu B \\ &= \frac{(P_\zeta + \psi_p)^2 B^2 e^2}{2mg^2} + \mu B \end{aligned}$$

which is left in SI units in order to show what the energy would be like for particles of different species. In the plasma physics units used in this thesis ($m = e = 1$) it is re-written as

$$\mathcal{E} = \frac{(P_\zeta + \psi_p)^2 B^2}{2g^2} + \mu B \ . \tag{4.23}$$

The green line in Figure 4.2 represents the HFS boundary of the plasma. If

a particle is transported from one of the confined regions such that its orbit now lies on this line, it will be lost from the plasma. At the point the particle exits the plasma, $B = B_{\min}$, $\psi_p = \psi_p(a)$ and $\theta = \pi$. Putting these into Equation 4.23 defines the equation for the line as

$$\frac{\left(P_\zeta + \psi_p(a)\right)^2 B_{\min}^2}{2g^2(\psi_t(a))} + \mu B_{\min} - \mathcal{E} = 0 \ . \tag{4.24}$$

The red line in Figure 4.2 represents the LFS boundary of the plasma. Orbits represented by a point on this line will be lost from the plasma, for example that shown by the cyan line in Figure 4.1. At this point, $B = B_{\max}$, $\psi_p = \psi_p(a)$ and $\theta = 0$. Putting these into Equation 4.23 gives the equation for the line as

$$\frac{\left(P_\zeta + \psi_p(a)\right)^2 B_{\max}^2}{2g^2(\psi_t(a))} + \mu B_{\max} - \mathcal{E} = 0 \ . \tag{4.25}$$

For an arbitrary distribution function, there may be particles whose unperturbed CoM lie in the lost particle region between the green and red lines. If they are immediately lost within one poloidal orbit, they are referred to as 'prompt loss' particles.

The magnetic axis of the plasma equilibrium is shown in Figure 4.2 by the magenta line. Orbits that at some point go through the magnetic axis lie along this line. Figure 4.2 shows that co-passing, counter-passing, trapped, stagnation and lost orbits are all capable of passing through the magnetic axis at some point. The yellow orbit in Figure 4.1 shows the boundary between potato and trapped orbits, and passes through the magnetic axis. On the line itself, $B = B_0$ and $\psi_p = 0$, so the line is given by the equation

$$\frac{P_\zeta^2 B_0^2}{2g^2(0)} + \mu B_0 - \mathcal{E} = 0 \ . \tag{4.26}$$

The orange boundary in Figure 4.2 discriminates between trapped orbits that have a bounce point and those which do not, completing full passing orbits. This occurs (to leading order) when $\rho_\parallel = 0$. From the unperturbed toroidal canonical angular momentum (Equations 2.57b) and 4.23 this line is defined by

$$\mu B(\psi_p, \theta) = \mathcal{E}; \qquad\qquad P_\zeta = -\psi_p \ ,$$

at $\theta = 0$ and $\theta = \pi$, and is subsequently referred to as the trapped-passing boundary. The region encased by the orange line is therefore the trapped particle region.

Where this region coincides with the lost region, trapped particles are lost from the plasma, and where it coincides with the passing region is where the potato orbits lie. A small region remains, encased by the black line. Within this region are passing orbits that do not encircle the magnetic axis - the stagnation orbits.

4.4 Linking LOCUST-GPU to HAGIS

Previous HAGIS simulations have typically used fast ion distribution functions that consisted of the product of two one dimensional functions (of radius and energy). It is desirable to use a full, six dimensional fast ion distribution function in order to gain an improved quantitative accuracy in the modelling. It is required that the distribution function has smooth, contiguous derivatives of f_0 with respect to $\mathcal{E}$, P_ζ and μ. An ideal source of such a distribution function is the the LOrentz Code for Use in Spherical Tokamaks (LOCUST-GPU) code, a fast ion code [129] that has recently been developed to run on Graphics Processing Units (GPUs) [130]. This section outlines how I have linked the two codes together.

4.4.1 The LOCUST-GPU Code

LOCUST-GPU is a fully gyro-phase resolved fast ion code capable of generating high-resolution distribution functions for use in tokamak simulations [130]. Rather than using a Monte-Carlo approach which requires post-processing to smooth the distribution function, LOCUST-GPU runs on the latest generation of General Purpose computing on GPUs (GPGPU) co-processors, and can therefore track sufficient particles in a short enough time to generate smooth enough distribution functions for use in MHD codes such as HAGIS. The previous Monte-Carlo codes such as TRANSP [131, 132] and NUBEAM [133] took much longer, and did not generate sufficiently smooth distribution functions required for HAGIS. An example of a distribution function from TRANSP that is calculated by NUBEAM is shown in Figure 4.3 [134]. A smooth distribution function is a requirement as it is the gradients in the distribution function that drive the MHD activity (Equation 2.66). LOCUST-GPU uses the Boris leap-frog tracking integrator scheme [135] to follow $\sim 10^7$ ions in $\sim$ 10 hours on four GPU cards. The result is a fully gyro-phase resolved tokamak fast ion distribution function.

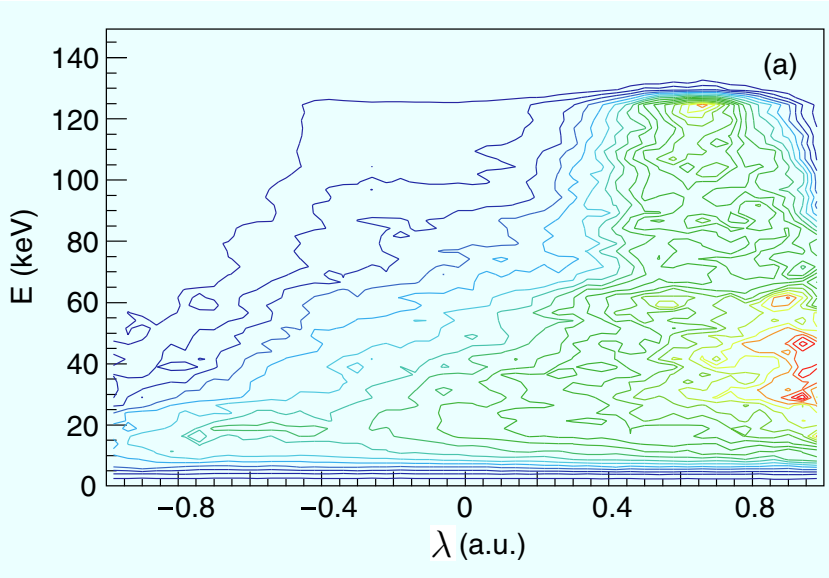

Figure 4.3: A beam ion slowing-down distribution function of λ vs $\mathcal{E}$ typically produced by TRANSP (figure taken from [134]).

4.4.2 Distribution Function Format

For use in the HAGIS code, the LOCUST-GPU distribution function has been converted into guiding centre format and stored in terms of the guiding centre CoM of the fast ions given by Equation 4.20. In order to more fully fill phase space (and hence get more accuracy per unit space of the distribution function), the magnetic moment dimension of the distribution function has instead been stored as $\mu/\mathcal{E}^{(0)} = \Lambda B$,

$$f_0 = f_0\left(\mathcal{E}^{(0)}, P_\zeta^{(0)}, \mu/\mathcal{E}^{(0)}, \sigma_d\right) \ , \tag{4.27}$$

where Λ is often referred to as the normalised pitch angle in the literature. Binning into the CoM space provides an element of orbit averaging for $\mathcal{E}$, P_ζ and μ since they are constants of the guiding centre motion. This is demonstrated in Figure 4.4. During the conversion to the CoM format, oscillations can be seen in the first-order calculation of μ; this is more pronounced on STs such as MAST. Previously in this thesis, it has been shown that the magnetic moment is approximately constant for a particle in a magnetic field (a result discovered by Alfvén [136]). It was shown by Kruskal [137] however to be the first term in a series,

$$\mu = \mu_0 + \epsilon\mu_1 + \epsilon^2\mu_2 + \cdots$$

such that the time derivative of μ is zero. The expansion parameter here is $\epsilon = \mathcal{O}(m/e)$, and μ_0 refers to the Alfvén solution given in Equation 2.9. To ensure that the magnetic moment remains a sufficiently close enough approximation to a constant in time during the transformation to the guiding centre approximation in LOCUST-GPU, the first order correction μ_1 is required [130]. The values of $(\mu_1, \mu_2, \cdots)$ are not specifically of relevance in this thesis, but are fully explained in [137–140].

In order to accommodate for the distribution function in terms of $\mu/\mathcal{E}^{(0)}$ in HAGIS, the following modification to Equation 4.22 is required

$$\dot{\delta f} = -\dot{\mathcal{E}} \left[\frac{\partial f_0}{\partial \mathcal{E}}\bigg|_{P_\zeta, \mu/\mathcal{E}} - \frac{\mu}{\mathcal{E}^2} \frac{\partial f_0}{\partial \left(\frac{\mu}{\mathcal{E}}\right)}\bigg|_{\mathcal{E}, P_\zeta} \right] - \dot{P}_\zeta \frac{\partial f_0}{\partial P_\zeta}\bigg|_{\mathcal{E}, \mu/\mathcal{E}} \underbrace{-\frac{\dot{\mu}}{\mathcal{E}} \frac{\partial f_0}{\partial \left(\frac{\mu}{\mathcal{E}}\right)}\bigg|_{\mathcal{E}, P_\zeta}}_{=0} \tag{4.28}$$

whereby the final term equals zero because in the guiding centre approximation μ is constant in time.

4.4.3 Coordinate System Transform

The LOCUST-GPU distribution function is written in terms of particles per unit $\mathrm{d}\mathcal{E}\ \mathrm{d}P_\zeta\ \mathrm{d}(\mu/\mathcal{E})$. To find it in terms of physical units (i.e. per unit space, per unit velocity space) that are required to calculate moments of the distribution function, a Jacobian is required. The LOCUST-GPU Jacobian $\mathcal{J}^L$ cannot be determined analytically, so is instead calculated (in LOCUST-GPU) using Monte-Carlo techniques [130]. The six dimensional space uniformly loaded Jacobian is found using [130]

$$\mathcal{J}^L = \frac{\Delta N(P_\zeta, \mu, \mathcal{E})}{\Delta P_\zeta \Delta\mu \Delta\mathcal{E}} \tag{4.29}$$

so the number of markers in the LOCUST-GPU distribution function (loaded into HAGIS) can now be written using Equation 4.5 in the form

$$\begin{aligned} N_p = \int f_0\ \mathrm{d}\Gamma^{(p)} &= \int f_{0,L}\ \mathrm{d}\Gamma^{(L)} \\ &= \int f_{0,L}\ \mathcal{J}^{(L)} \mathrm{d}\Gamma^{(p)} \end{aligned} \tag{4.30}$$

where f_0 is the unperturbed HAGIS distribution function, $f_{0,L}$ is the corresponding LOCUST-GPU distribution function and

$$\mathrm{d}\Gamma^{(L)} = \mathrm{d}^3x_L\ \mathrm{d}^3v_L = \mathcal{J}^{(L)}\ \mathrm{d}\Gamma^{(p)}$$

is the LOCUST-GPU phase space element, written in terms of the HAGIS phase space element.

4.4.4 HAGIS use of Distribution Function

HAGIS reads in the LOCUST-GPU distribution function. The distribution function f_0 is splined using third-order cubic spline interpolation in order to evaluate it at the required location of phase space where the marker resides. The Jacobian $\mathcal{J}^L$ is also splined as it is required for calculating moments of the distribution function.

4.4.5 Orbit Verification

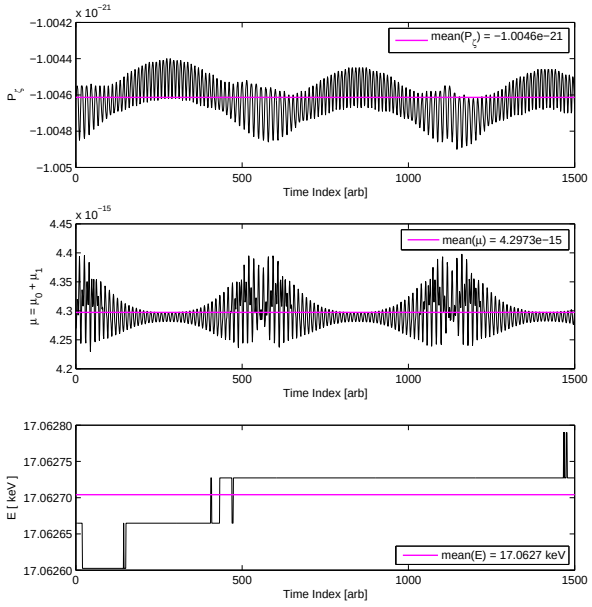

Figure 4.4: Mean CoM values for an example particle orbit in a LOCUST-GPU MAST fast ion distribution function. The full orbit values are shown in black and the guiding centre approximation in magenta.

A good way to confirm that like-for-like is being compared when the two codes have been linked is by comparing orbits. Here, orbits have been evaluated in both codes and plotted simultaneously to confirm that the two are equivalent, and that all of the quantities (such as the orbit precession) are pointing in the same direction. LOCUST-GPU is a full-orbit code, and the CoM are conserved for the full particle orbit. In converting to the guiding centre approximation, the constants of motion have slight variations. Full-orbit and the associated guiding centre for

two types of orbit have been taken from LOCUST-GPU. The mean orbit CoM ($\mathcal{E}$, P_ζ, $\mu = \mu_0 + \mu_1$) are found from the full orbit values as shown in Figure 4.4. An identical particle is then launched in HAGIS, within the same equilibrium at the same location in the tokamak and with the same velocity components (given by $\mathcal{E}$ and λ, calculated from the constants of motion using $\lambda = \sqrt{1 - \frac{\mu B}{\mathcal{E}}}$).

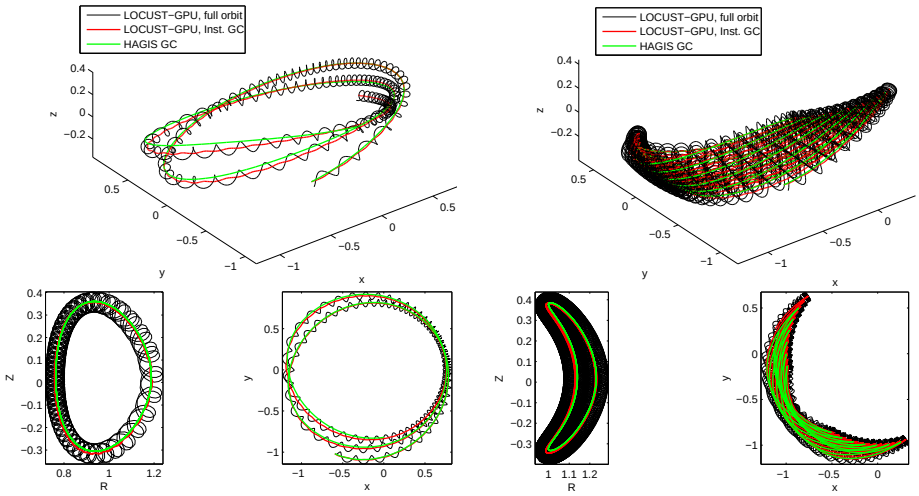

(a) Passing Particle (b) Trapped Particle

Figure 4.5: Comparison of orbits from the LOCUST-GPU code and the HAGIS code. The green line shows the HAGIS guiding centre particle orbit, the black line the LOCUST-GPU particle fully gyro-phase resolved orbit and the red line the LOCUST-GPU guiding centre approximation.

Figure 4.5 shows that the orbits are close. Due to the different particle tracking techniques used in the two codes, the orbits are not identical at the end, but show the two codes are shown to be consistent so this fast ion distribution function is suitable for using in HAGIS. By using a trapped particle, as shown in Figure 4.5(b), the precession of the orbits is also shown to be the same. The tips of the trapped orbits do not exactly match the tips of the LOCUST-GPU orbits due to the application of the Boris scheme [141].

4.4.6 Benchmarking Code Changes

In order to verify the code implemented to enable the use of a fast ion distribution function from LOCUST-GPU, HAGIS must be benchmarked against previous runs as well as against other comparable plasma physics codes. A very unstable high-n TAE mode is considered, which provides sufficient drive for the growth rate to be determined within a few wave periods of the simulation. It is performed in an

ITER-like plasma containing an isotropic distribution of α-particles equivalent to that expected in an ignited plasma. This EP population is in the form of a slowing-down distribution function. It is prescribed as a product of two functions, one of radius $f_1(\psi_p)$ and one of energy $f_2(\mathcal{E})$ and is given in Equation 4.31.

$$f_0(\psi_p, \mathcal{E}) = C \underbrace{\left(\frac{1}{\exp[(\psi_p/\psi_0)/\Delta\psi] + 1} \right)}_{f_1(\psi_p)} \underbrace{\frac{1}{\mathcal{E}^{3/2} + \mathcal{E}_c^{3/2}} \mathrm{Erf_c} \left[\frac{\mathcal{E} - \mathcal{E}_0}{\Delta\mathcal{E}} \right]}_{f_2(\mathcal{E})} \tag{4.31}$$

where ψ_0 is the deposition radius (chosen to be near the $q = 1$ surface), $\mathcal{E}_0$ is the initial energy of the fast ions (for α-particle this is the energy they are born at) and $\Delta\psi$ and $\Delta\mathcal{E}$ are parameters given below. $\mathcal{E}_c$ is the critical energy above which the fast particle power goes primarily to the electrons. Up until this energy, the bulk ion friction balances the electron friction and the power transfer to both is equal. The critical energy is given by [142]

$$\mathcal{E}_c = 14.8 A_f T_e \left(\frac{\sum_i n_i \left(Z_i^2 / A_i \right) \ln \Lambda_i}{n_e \ln \Lambda_e} \right)^{2/3} \tag{4.32}$$

where A_f and A_i are the atomic masses of the fast and thermal ions, T_e is the the electron temperature n_i and n_e are the ion and electron densities and Z_i is the thermal ion atomic number. The ratio between the Debye length and the distance of closest approach (from Coulomb scattering theory) is given by Λ_i and Λ_e. For a $D - T$ plasma where the reactants have a common temperature, this gives an energy distribution that is roughly Gaussian in shape, and a Fermi-shaped radial distribution. The ITER-like parameters chosen for this simulation are $\psi_0 = 0.2$, $\Delta\psi = 1/14$, $\mathcal{E}_0 = 3.52$ MeV, $\mathcal{E}_c = 329.6$ keV and $\delta\mathcal{E} = 335.2$ keV.

This distribution function has been represented both analytically using Equation 4.31 (the conventional way) and also numerically, in a format that is equivalent to the LOCUST-GPU fast ion distribution function. The numerical distribution function was found by sampling Equation 4.31 on a regular ($\mathcal{E}$, P_ζ, $\mu/\mathcal{E}$) grid. The two sets of runs retained all other simulation parameters equal to those used in previous runs of this benchmark, done in [65] and [74] to benchmark HAGIS against the CASTOR-K code [143], which is a hybrid MHD-gyrokinetic model developed for the stability analysis of global Alfvén waves in the presence of energetic ions. This has been repeated to ensure that the code is still reporting the same results, and to ensure that the new numerical distribution function is equivalent. In this comparison, the phase of the mode was held fixed and a scan was performed through mode frequency. The original results found in [65, 74, 143] are recovered. The HAGIS

growth rates, performed using the analytical fast ion distribution function are shown by the black dots in 4.6. The agreement remains good with the CASTOR-K code [143] at two different orbit sizes (the squares and the line in Figure 4.6). The results found using the new numerical fast ion distribution function are also plotted, and shown to coincide well with the equivalent analytical HAGIS distribution function. Slight discrepancies exist between the runs done using the analytical and numerical distribution functions, these are due to the limited grid resolution used. The analytical method can determine the precise values of f_0, whereas the numerical one relies on cubic spline interpolation to do so. The LOCUST-GPU distribution functions are performed at much higher resolution so this effect will be reduced; the grid resolution used in this case was sufficient to confirm the accuracy of the benchmark. As the mode frequency changes, different classes of particles become resonant. This accounts for the lines not being smooth; it is particularly significant as these classes of orbits are very clearly defined in a LOCUST-GPU distribution function, more so than in a distribution function that is a product only of radial and energy functions (although in this benchmark that is not necessarily the case as the distribution function was not created in LOCUST-GPU).

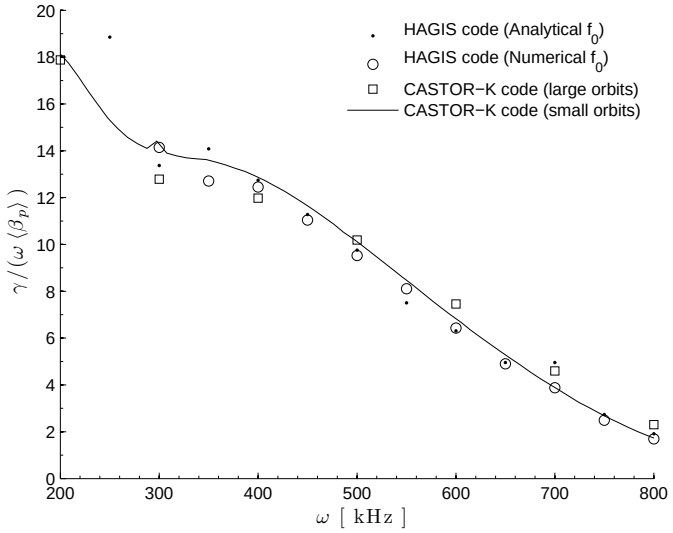

Figure 4.6: Comparison of growth rate at different mode frequencies for a ($n = 10$, $m = 8, 9$) TAE mode. The numerical LOCUST-GPU-like fast ion distribution function gives the same results as the analytically prescribed distribution function.

4.5 Summary

The HAGIS code has been outlined, and the requirement for a high-resolution, multi-dimensional fast ion distribution function in this code to replace the current analytical product of two one dimensional functions has been explained. This leads on to the LOCUST-GPU code, capable of creating such distribution functions. These can be accurately represented in terms of the particle's CoM, which are best pictured in a CoM phase space that is easily separated into different orbit classifications.

The method used to link the two codes together has been described, providing a new framework in which more quantitative results can be found using the HAGIS code. The newly implemented capability in HAGIS to use distribution functions from LOCUST-GPU has been benchmarked against previous results, and also compared for an example in which the same distribution function has been used in two ways to find the same level of radial redistribution. We are now in a position to use HAGIS to investigate a real MAST phenomenon using a LOCUST-GPU fast ion distribution function, the method for doing so is explained in the next chapter.

Chapter 5

Modelling Fishbones in MAST

In order to model complex plasma phenomena such as fishbones in tokamaks, a suite of interconnected plasma physics codes is required. The flow of information throughout the entire process is shown schematically in Figure 5.1. This chapter

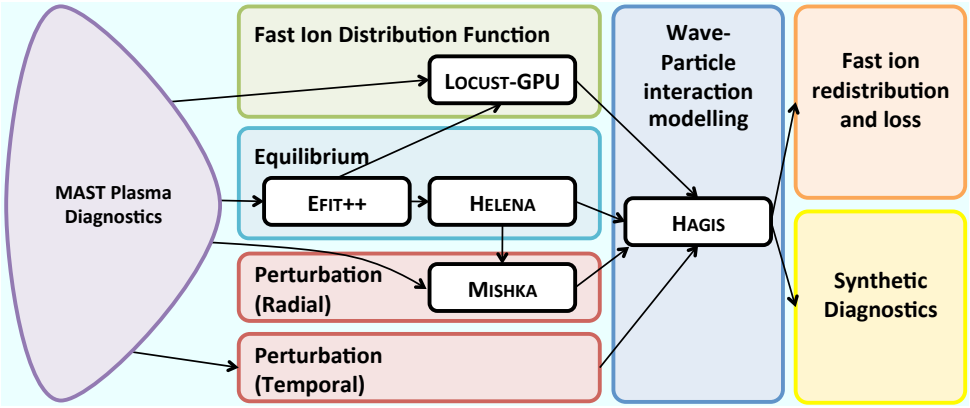

Figure 5.1: MAST fishbone mode model. The relationships between the codes used (shown in white boxes) and how the model is built up from the inputs required by HAGIS to the outputs.

describes the steps taken in the modelling, building up the complexity via explanations of each stage in the process. The three primary inputs into HAGIS are the equilibrium, the fast ion distribution function and the fishbone mode perturbation, which are explained in detail in Sections 5.2 - 5.4. The HAGIS modelling is then explained in detail, such that the redistribution and loss of fast ions may be subsequently quantified (in Chapter 6) in addition to computationally modelling what the experimental diagnostics measure by means of 'synthetic diagnostics' (Chapter 7). The modelling that has been done also yields important information about what parts of phase space are resonant with the mode, which provide us with a better

understanding of fishbone modes. It also affords us a predictive capability to design experiments that potentially ameliorate fishbones.

Fishbones are strongly nonlinear phenomena, this is identified by their burst-like structure and significant decrease in oscillation frequency during a chirp. Diamagnetic fishbones, which exist in the diamagnetic frequency gap ($\omega \approx \omega_{*\mathrm{i}}$), are modelled using a perturbative approach [110]. This draws similarities to the bump-on-tail problem, along with other wave-particle interaction phenomena [144]. Precessional fishbones however lie within the nonlinear regime that they may be modelled using a non-perturbative method [110] - this approach is employed in the work presented in this thesis. Further discussion of the strong and weak nonlinear regimes can be found in [145].

5.1 Reference Frames

Plasmas in STs such as MAST are capable of rotating toroidally at velocities up to the ion sound speed [146]. This means that there are two relevant reference frames that may be considered in this model: the first is the stationary lab frame; the second is the plasma frame, which in comparison to the lab frame rotates at the rotation frequency of the plasma. Assuming each flux surface rotates as a rigid body at the same toroidal rotation velocity [147], the angular velocity associated with the toroidal rotation is considered to be a flux function. The plasma rotation from the bulk (thermal) ions is shown in Figure 5.9(c).

5.2 Equilibrium

The first requirement of the modelling is to perform an accurate equilibrium reconstruction. In this investigation the equilibrium for MAST shot `#27920` is taken as a reconstruction of the plasma during a period of quiescent MHD activity at $t = 230$ms. Shown in Figure 3.4, this is at the centre of an inter-fishbone period in order to provide to closest approximation to a steady-state plasma. In the modelling, the equilibrium remains unchanged during the fishbone. This assumption is made on the basis that the fishbone timescale is shorter than the timescale of changes to the equilibrium, and is made for all modelling done using HAGIS.

The equilibrium is reconstructed in Cartesian coordinates from the MAST diagnostics using EFIT++ [148]. The reconstruction was made using an MSE-constrained q-profile, density profiles from the TS system [54] and temperature profiles from both the TS and the CXRS. Impurities were ignored, i.e. Z_{eff} was

assumed to be unity. The equilibrium was adjusted to take into account the fast ions (this was required in order to find the $n = 1$ $m = -1$ internal kink mode in the stability analysis, see Section 5.4.1). It is then processed using the HELENA code [149], which solves the Grad-Shafranov equation (Equation 2.47) in the (R, Z) plane using an isoparametric bicubic Hermite finite element approach and outputs the equilibrium in straight field line coordinates.

A cross section of the resulting axisymmetric tokamak equilibrium is shown in Figure 5.2. The other equilibrium quantities that are calculated are the q-profile, the pressure, the toroidal current function and the poloidal current function. These are shown in Figure 5.3 (the q-profile is inverted compared to some MAST publications - this is because of the definition of q that is used here). The accuracy of the LCFS in the equilibrium reconstruction has been verified via comparison with the optical data from the high speed visible camera diagnostic using the OFIT code [150], shown in Figure 5.2. This confirms that the EFIT++ equilibrium is accurate (OFIT incorporates the two x-points of the DND, hence the discrepancy at the top and bottom of the plasma).

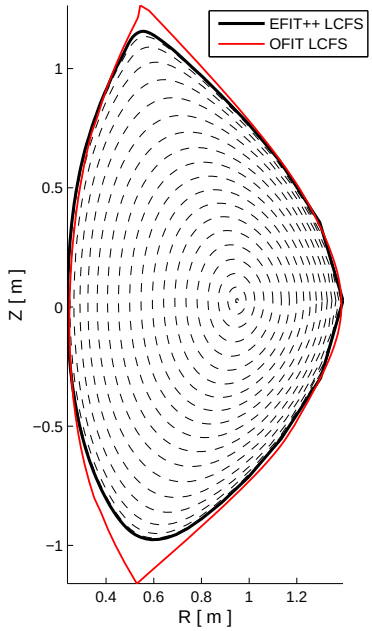

Figure 5.2: MAST shot #27920 axisymmetric flux surface plot. The black lines show the EFIT++ reconstruction (for clarity, only every fifth flux surface used in the modelling is plotted) and the red line shows the LCFS approximation from the high speed camera found using OFIT.

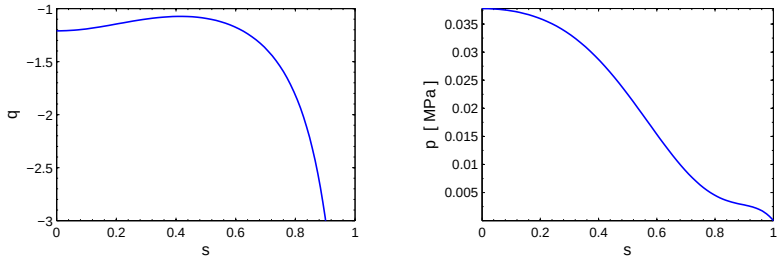

(a) Safety Factor (b) Pressure

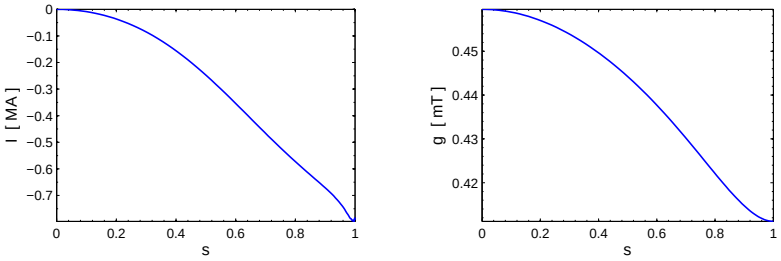

(c) Toroidal Current Function (d) Poloidal current function

Figure 5.3: Quantities from the equilibrium reconstruction of shot #27920 at 230ms as a function of the normalised radial coordinate s.

5.3 Fast Ion Distribution Function

An accurate representation of the fast ion distribution function is crucial. In this investigation, a fast ion distribution from the LOCUST-GPU code has been used. How this has been read into the HAGIS code is explained in detail in Chapter 4. As with the equilibrium, the EP population present in MAST shot #27920 has been reconstructed during the quiescent period of MHD activity at $t = 230$ms. The distribution function is calculated in LOCUST-GPU, using the same EFIT++ equilibrium as HAGIS. This is crucial as it is the equilibrium that defines the guiding centre CoM $(\mathcal{E}, P_\zeta, \mu)$ of the fast particles.

During shot #27920 both NBI beams were on, each producing 1.5MW of beam power. The beams drive plasma current, and are injected in the co-current direction resulting in a predominantly co-passing distribution function. Figure 5.4(a) and 5.4(b) show a slice of distribution function in terms of the orbit invariants $(\mathcal{E}, P_\zeta, \mu)$ at $\mathcal{E} = 20$keV. This is a fully-thermalised two-beam distribution function, written out in terms of the CoM of the EP population onto a grid of resolution $(N_\mathcal{E} \times N_{P_\zeta} \times N_\mu)$ where $N_\mathcal{E} = 119$, $N_{P_\zeta} = 339$ and $N_\mu = 124$. The LOCUST-GPU Jacobian (see Equation 4.29), is determined numerically in the code using the technique outlined in Section 4.4.3 and is shown in Figure 5.4(c) and 5.4(d). These

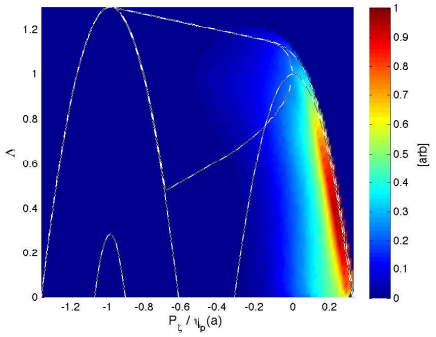

(a) f_0 (co-propagating particles) in terms of the CoM units.

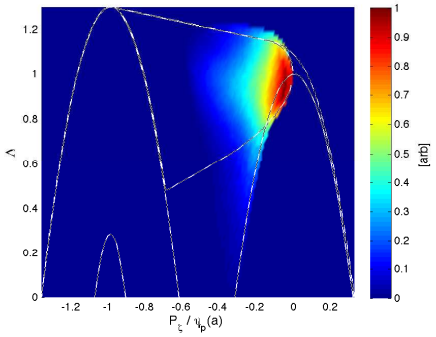

(b) f_0 (counter-propagating particles) in terms of the CoM units.

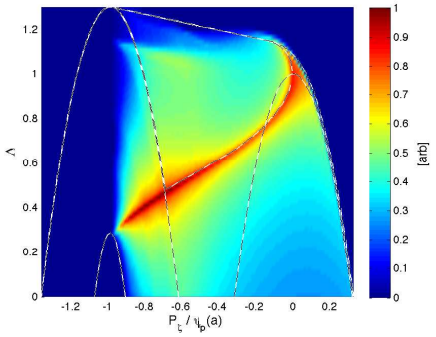

(c) $\mathcal{J}^L$ (co-propagating particles).

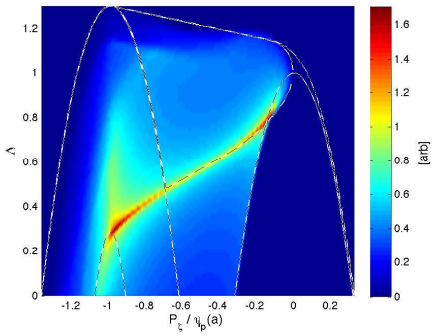

(d) $\mathcal{J}^L$ (counter-propagating particles).

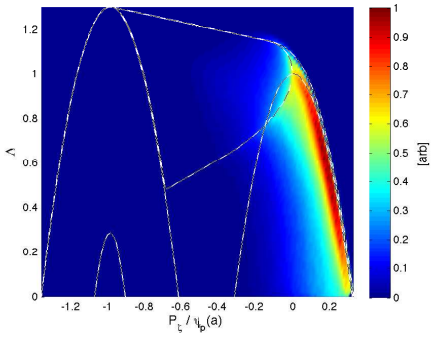

(e) $f_0\mathcal{J}^L$ (co-propagating particles) in terms of the real-space units.

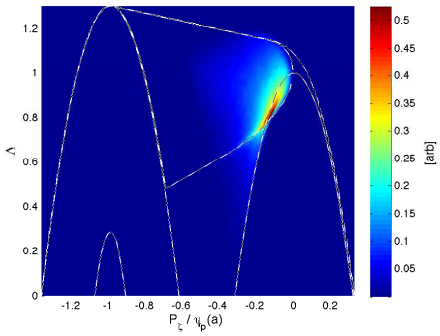

(f) $f_0\mathcal{J}^L$ (counter-propagating particles) in terms of the real-space units.

Figure 5.4: A slice of the fast ion distribution function and corresponding Jacobian created by the LOCUST-GPU code at $\mathcal{E}$ =20keV. (a) and (b) show the fast ion distribution function where each location represents the density of fast particles per unit ($\mathcal{E}$, P_ζ, μ). The Jacobian shown in (c) and (d) is calculated using Equation 4.29, and converts from this into per physical space units (i.e. per $\mathrm{m^3 s^{-1}}$). The red areas show regions of this phase space which make up the largest parts of the real units phase space. (d) and (e) show $f_0\mathcal{J}^L$, the fast ion distribution function in real space units. Note the different scaling, whereby the trapped region in both is the same but in order to see the co-passing particle region in (e) they have been plotted on different scales. The black and white dashed lines show the intersects between regions containing different orbit classifications (see Figure 4.2).

figures show how the CoM phase space written in units of $(\mathcal{E}, P_\zeta, \mu)$ relate to it when it is written in terms of real space units, and allows a physical understanding of where the phase space lies in terms of the real units. In terms of the real units, the distribution function is shown in Figures 5.4(e) and 5.4(f) for the co- and counter-passing particles respectively; integrating this gives N_p (as in Equation 4.30). Both the co- and counter-passing regions have the same density in the trapped region (note the scaling is different due to the co/counter density disparity in the passing region).

5.4 Perturbation

During the fishbone, the mode evolves temporally in both amplitude (the bursting nature) and frequency (the chirping nature). The spatial structure of the mode is determined by means of a radial displacement, and is assumed to be invariant in time. The temporal evolution is prescribed to the model in order to match the experimental observations, rather than allowing the mode to evolve according to the drive from the EP population.

5.4.1 Radial Perturbation

The radial displacement of the plasma is determined using MHD stability analysis carried out using the linear MHD stability code MISHKA [151]. It has been assumed that the internal kink mode observed for the fishbone is identical to the internal kink mode that is found using the linear stability analysis (which is a normal mode of the background plasma). Within the framework of the additional assumptions made in Section 3.6.2, multiple toroidal mode harmonics can be studied, modelled using different waves in HAGIS. The experimental data showed that toroidal modes up to $n = 3$ made significant contributions to the perturbation, shown in Figure 3.6. Mode eigenfunctions have been found for $1 < n < 4$, and for the dominant poloidal modes $-6 < m < 0$.

Finding Unstable Eigenmodes in MISHKA

The linear MHD mode found during stability analysis using MISHKA is dependent upon the equilibrium. The unstable growing modes have positive growth rates, $\gamma > 0$, the oscillating modes have negative growth rates, $\gamma < 0$. Since the fishbone mode is a growing mode the growth rate must be positive, providing a way to be sure the correct mode has been found. These modes are found using MISHKA for $1 < n < 4$.

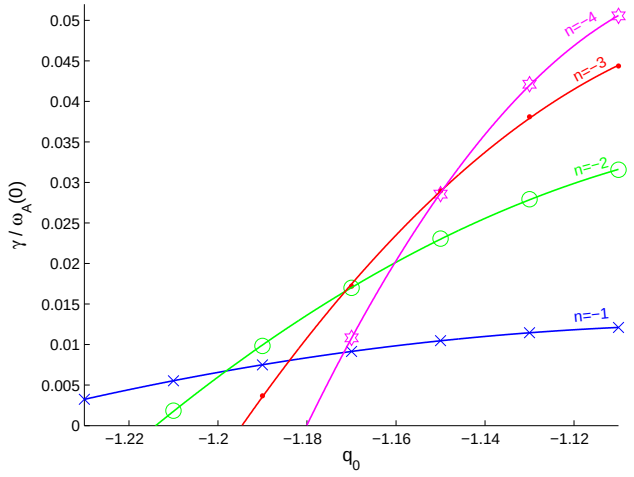

Figure 5.5: Finding growing modes ($\gamma > 0$) using the MISHKA code by varying q_0 to scale the q profile. Unstable modes require the q_0 to be lowered from the equilibrium level. The growth rate of the mode has been normalised to the on-axis Alfvén frequency $\omega_A(0)$

The equilibrium used for this study has $q_0 = -1.23$. Figure 5.5 shows that for this equilibrium, no unstable modes exist for $n > 1$ at this q_0. For this reason, during the stability analysis the q-profile had to be adjusted by lowering the value of q_0 in order to find the unstable mode. This is satisfactory, as the fishbone mode is known to be a low frequency internal kink; the stability analysis cannot however find it as it requires additional fast ion effects (the modelling here assumes that it is identical to an equivalent normal mode of the plasma). The value of q_0 needed to find a growing mode increases with growing n. The growth rate of the unstable modes was tracked as a function of q_0 for each of the n harmonics. In order to find the $n = 3$ mode, the q_0 only had to be dropped by less than 3%. Similar analysis has previously been made for the higher n components of the LLM in [117].

The resulting radial mode displacements ξ_r for the four toroidal and six poloidal modes are shown in Figure 5.6, determined from the linear stability analysis performed using MISHKA. The q-profile is shown for these shots in Figure 5.3(a), which was scaled by varying the value of q_0 used in order to find a linearly unstable kink mode, given by the point at which the relevant line crosses the x-axis in Figure 5.5.

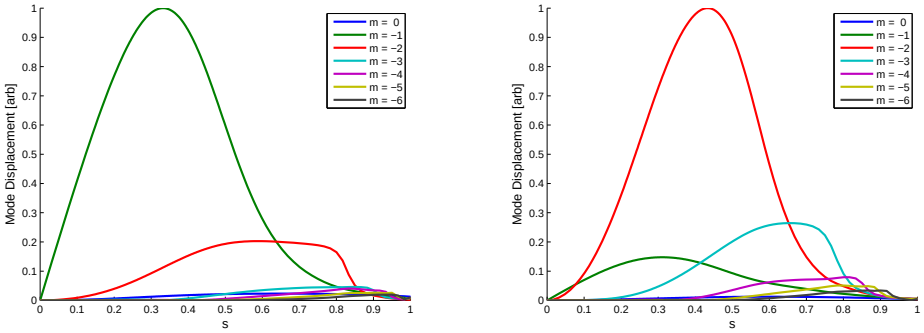

(a) $n = 1$ (b) $n = 2$

(c) $n = 3$ (d) $n = 4$

Figure 5.6: Radial mode perturbation determined from linear MHD analysis performed using the MISHKA code. The dominant poloidal harmonics occur when $m = -n$.

5.4.2 Temporal Perturbation

The mode frequency is evolved in time according to what is observed experimentally in the Mirnov coil signal, as is shown in Figure 5.7. The chirping mode frequency of the n^{th} harmonic detected by the Mirnov coil in the lab frame $\omega_{k,\text{lab}}$ is the sum of the frequency in the plasma frame ω_k and the rotation frequency ω_r,

$$\omega_{k,\text{lab}}(t) = \omega_k(t) + n\omega_r \ . \tag{5.1}$$

Previous work has assumed that the rotation frequency remains constant during the fishbone burst. Recent research [152] has suggested however that this may not be the case, pinpointing a radial torque from a change in ω_r to be the cause of the frequency chirping. In this investigation it has been assumed that the plasma rotation remains

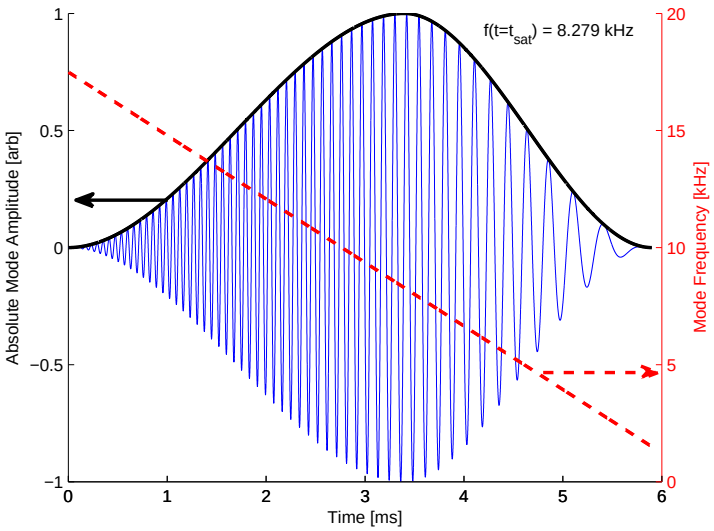

Figure 5.7: The forced temporal mode evolution input into HAGIS. Absolute magnitude (thick solid black line), mode frequency (dashed, red line) and mode amplitude (thin solid blue line). The initial frequency is 17.5kHz and chirps down at a sweeping rate of -2.71×10^6kHz/s.

constant throughout the fishbone. The frequency sweeping is evolved according to

$$\omega_k(t) = \omega_k(t = t_0) + \omega_s \left[t - t_0\right] \tag{5.2}$$

where the initial mode frequency $\omega_k(t = t_0)$ in the Lab frame and the sweeping rate $\omega_s = \partial\omega_k/\partial t$ are measured from the experimental data, taken from Figure 3.4.

The shape of the mode is specified by the normalised mode amplitude, A_{norm}. This is divided into two distinct regions: one for the growth up until the mode saturation time ($t < t_{\text{sat}}$) and one for the subsequent delay following this time ($t \geqslant t_{\text{sat}}$).

$$A_{\text{norm}}(t) = \begin{cases} \frac{(3t_s - 2t)t^2}{t_s^3} & \text{for } t < t_s \\ \frac{(3(\Delta t - t_s) - 2(\Delta t - t))(\Delta t - t)^2}{(\Delta t - t_s)^3} & \text{for } t \geqslant t_s \end{cases} \tag{5.3}$$

where Δt is the duration of the fishbone. The time evolution of the fishbone mode is shown in Figure 5.7. The chirping frequency has been taken from Figure 3.4 and the shape of the mode amplitude envelope has been taken from Figure 3.6(a), parameters for which are given in Table 5.1.

5.4.3 Relative Mode Amplitudes

The relative mode amplitudes of the toroidal mode harmonics were calculated in Section 3.6.2. From this, the relative temporal mode amplitude is evolved according to

$$A_t(t) = \sum_{k=1}^{N_w} A_{\text{norm}}(t) A_k \mathrm{e}^{-i\left(\omega_{k,0}t + \frac{1}{2}\omega_{k,s}t^2\right)} \tag{5.4}$$

where $A_{\text{norm}}(t)$ is the mode amplitude envelope (black line in Figure 5.7), A_k is the relative amplitude of that mode and $\omega_{k,s} = \mathrm{d}\omega_k/\mathrm{d}t$ is the sweeping rate. In order to see what, if any, effect there is of modelling the higher n harmonics in this way, peak relative mode amplitude (for example A_2/A_1) was taken to be that at its largest during the chirp. This was determined in Figure 3.6 as $A_1 = 1$, $A_2 = 0.43$ and $A_3 = 0.13$; $A_{n\neq1,2,3} = 0$. As a check, a spectrograph has been constructed of the signal that is input into HAGIS for the multiple modes evolved according to Equation 5.4, shown in Figure 5.8(b).

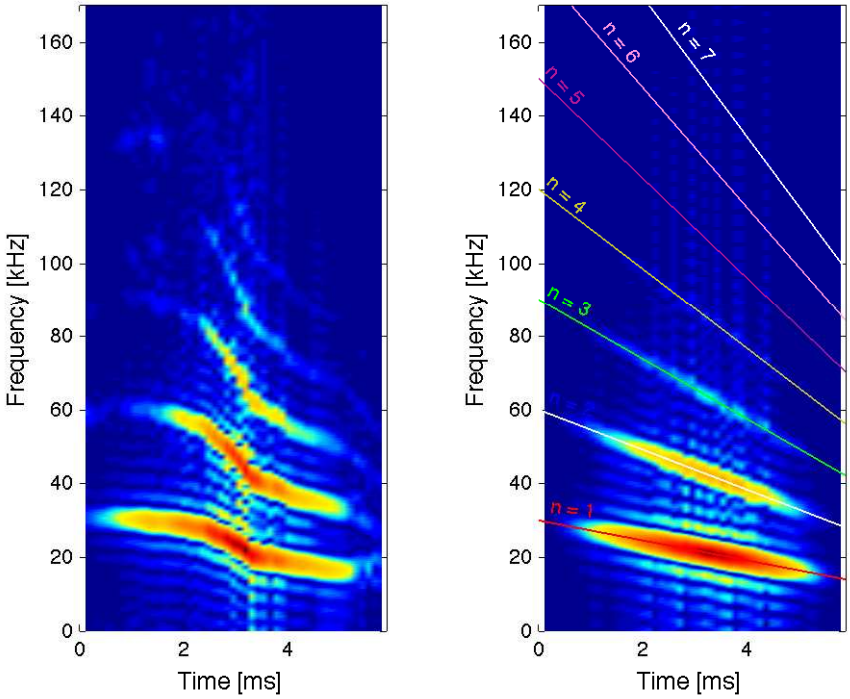

(a) Experimental Spectrograph

(b) Numerical Spectrograph of HAGIS input.

Figure 5.8: Comparison of HAGIS perturbation input to experimental data (in the lab frame). (a) shows the experimentally observed perturbation spectrograph is a zoomed in section of the one shown in Figure 3.4. (b) shows the numerical representation of the perturbation that is prescribed to HAGIS. Toroidal harmonics ($1< n <3$) have been plotted, but lines showing sweeping for theoretical higher modes are also shown.

5.4.4 Perturbation Specification

A summary of the fishbone mode applied according to the variables set out in the preceding sections is given in Table 5.1, which matches the fishbone present in shot #27920 at 230ms as closely as possible.

Parameter	**Value**
Fishbone Duration	$\Delta t = 5.9$ ms
Saturation Time	$t_{\text{sat}} = 3.4$ms
Initial Frequency	$\omega(t = t_0) = 17.5$kHz
Sweeping Rate	ω_s = -2.7119$\times 10^6$kHz/s
Peak Mode Amplitude	$1\times 10^{-4} < \frac{\delta B}{B}(t = t_{\text{sat}}) < 1 \times 10^{-2}$

Table 5.1: Specification of fishbone mode at 230ms in MAST shot #27920.

5.4.5 Mode Evolution

In this investigation, the mode is prescribed according to the experimental diagnostic data, rather than being allowed to evolve self consistently according the the EP drive. The result of this is that the subsequent redistribution of the fast ion population can be determined, which provides synthetic diagnostic data. The mode evolution is prescribed to the code in the following way.

The temporal amplitude evolution $A_t(t)$ is given by Equation 5.3 and the frequency $\omega_k(t)$ chirps downwards to match the experimental fishbone mode. The scalar potential for each mode in the system given these constraints modifies Equation 4.8 such that it is written

$$\tilde{\Phi}_k(\psi_p, \zeta, \theta, t) = A_t(t) \sum_m \tilde{\phi}_{km}(\psi_p) \mathrm{e}^{i\left(n\zeta - m\theta - \int \omega_k(t) \mathrm{d}t\right)} \ , \tag{5.5}$$

where $\omega_k(t) = \omega_{k,0} + \omega_{k,s}t$ is the frequency of that mode harmonic at that time in the chirp. Using Equation 4.10 in the same way as was used to find Equation 4.11, the magnetic perturbation parameter $\tilde{\alpha}$ for a varying mode amplitude is found to be

$$
\begin{aligned}
\boldsymbol{\nabla}_{\parallel}\tilde{\Phi}_k &= -\frac{\partial}{\partial t}\left(\tilde{\alpha}_{km}B_0\right) \\
A_t(t)k_{\parallel,m}\sum_m \tilde{\phi}_{km}\mathrm{e}^{i\left(n_k\zeta - m\theta - \int \omega_k(t)\mathrm{d}t\right)} &= -\left[\dot{A}_t(t) - i\omega_k(t)A_t(t)\right] \\
&\quad \times B_0\sum_m \tilde{\alpha}_{km}\mathrm{e}^{i\left(n_k\zeta - m\theta - \int \omega_k(t)\mathrm{d}t\right)} \\
\tilde{\alpha}_{km}(\psi_p) &= \frac{-k_{\parallel,m}\tilde{\phi}_{km}(\psi_p)}{B_0\left[\dot{A}_t(t)/A_t(t) - i\omega_k(t)\right]}\,,
\end{aligned}
$$

where $\dot{A}_t(t) = \partial A_t(t)/\partial t$.

5.5 Thermal Ions

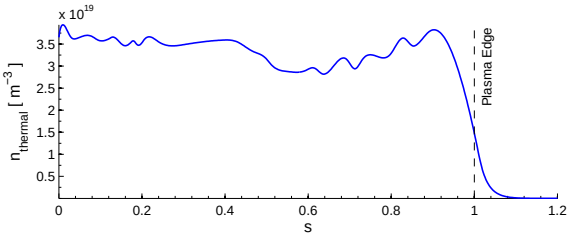

(a) Thermal Ion Density.

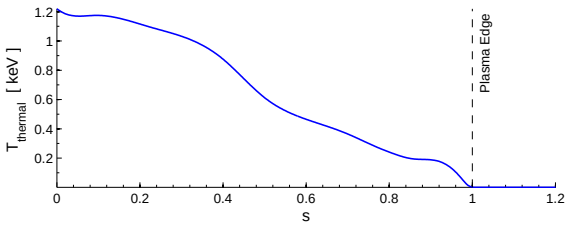

(b) Thermal Ion Temperature

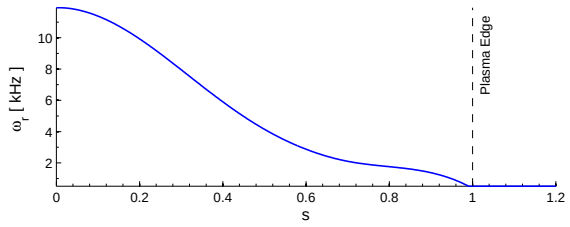

(c) Rotation Frequency

Figure 5.9: Thermal ion profiles for MAST shot `#27920` (flux surface approximations made using the LOCUST-GPU code).

HAGIS simulates only the EP population, made up of ions with energy above a critical level whereby they are referred to as fast ions. The thermal ion population is also relevant, particularly for neutron diagnostics (see Chapter 7). The radial density and temperature profiles along with the rotation frequency for this shot for the thermal ion population, approximated as a flux function, is shown in Figure 5.9.

5.6 Resonant Particles

It is possible to determine the regions of the phase space that will be resonant with the mode. The regions become resonant with the mode at its frequency ω, and since this is a Frequency Sweeping (FS) mode, the resonant regions will sweep out through phase space during the chirp. This results in different parts of the EP population becoming resonant with the mode at different times throughout the burst. As described in Chapter 2, it is the gradients in the distribution function that drive the growth of the mode. For this reason, it is when the resonant particles pass through the steepest positive gradients in P_ζ that the mode will be driven the strongest, and the steepest positive gradients in $\mathcal{E}$ that it will be damped the most.

The complex nature of the trapped particle orbits means that it is not likely that the resonant condition given in Equation 2.65 will be satisfied for the entirety of the orbit [153]. For this reason, it is the precession frequency that is important in the trapped particle resonances; provided that an integer number of toroidal and poloidal precessionary resonances occur then the particles are resonant. The precession is defined by the poloidal transit frequency ω_θ and the toroidal precession frequency ω_ζ. By definition it is only the trapped particles that precess, so in the case of the passing particles ω_ζ represents the toroidal transit frequency (the inverse of the time taken for that particle to traverse the plasma toroidally). The values for ω_θ and ω_ζ are functions only of the equilibrium, and not related to the mode or the distribution function. The distribution function sets how many particles are present at each location in phase space, and the mode determines the frequency at which a particle with a given ω_θ and ω_ζ will be resonant.

The resonance condition is given by Equation 2.65. For each location in phase space that represents a viable particle orbit, the poloidal transit frequency and toroidal precession frequency may be calculated using

$$\omega_\theta = \left\langle \dot{\theta} \right\rangle = \frac{\oint \theta \mathrm{d}t}{\oint \mathrm{d}t} = \frac{2\pi}{\Delta t} , \tag{5.6}$$

$$\omega_\zeta = \left\langle \dot{\zeta} \right\rangle = \frac{\oint \zeta \mathrm{d}t}{\oint \mathrm{d}t} = \frac{\Delta \zeta}{\Delta t} . \tag{5.7}$$

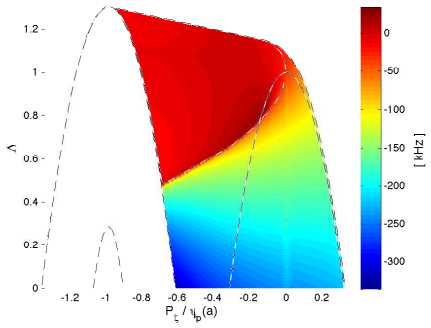

(a) Toroidal transit frequency ω_ζ for the passing particles (co-passing launched particles).

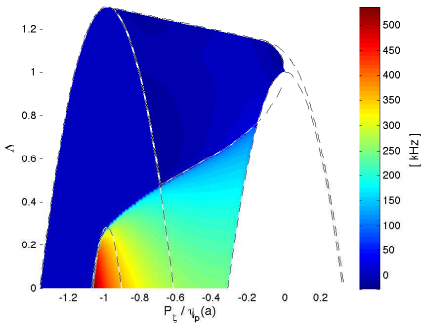

(b) Toroidal transit frequency ω_ζ for the passing particles (counter-passing launched particles).

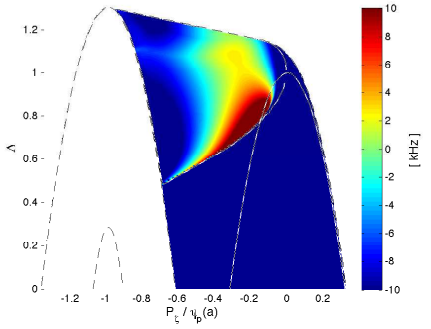

(c) Toroidal precession frequency ω_ζ for the trapped particles (co-passing launched particles).

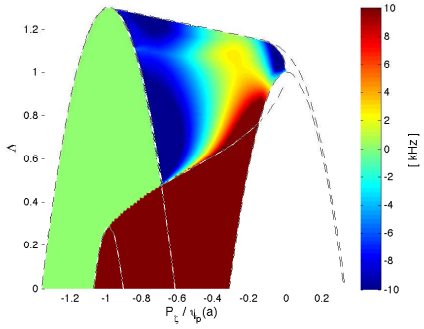

(d) Toroidal precession frequency ω_ζ for the trapped particles (counter-passing launched particles).

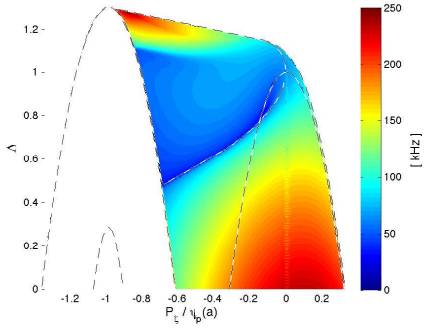

(e) Poloidal transit frequency ω_θ (co-passing launched particles).

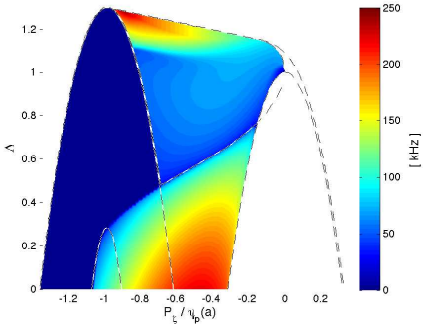

(f) Poloidal transit frequency ω_θ (counter-passing launched particles).

Figure 5.10: Slices at $\mathcal{E} = 20$keV of toroidal and poloidal frequencies for particles in MAST shot `#27920` at 230ms in CoM phase space. ω_ζ has been plotted on two different frequency scales, since the trapped particles and passing particles traverse the device toroidally at very different frequencies due to bounce points in the trapped particle orbits. Negative frequency denotes particles which orbit the device in the opposite direction.

where the integrals are around a single orbit projection. The HAGIS code can be used in order to determine the the resonant regions. For each location in the three dimensional phase space ($\mathcal{E}$,P_ζ,μ) a marker is launched, and the two frequencies are calculated. A slice at $\mathcal{E} = 20$keV is shown in Figure 5.10. This is plotted separately for co- and counter-launched particles (defined by σ_d). Both are required in order to show the frequencies for the whole of phase space, since some regions in the CoM phase space contain degenerate orbits. Since the passing particles do not experience the magnetic mirror effect and change direction, their toroidal transit frequencies are much higher than the precession frequencies of the trapped particles. For the passing particles, ω_ζ is shown in Figures 5.10(a) and 5.10(b). By changing the scale, the slower precession frequency variation within the trapped region becomes apparent, shown in Figures 5.10(c) and 5.10(d). This effect is less pronounced for the poloidal transit frequency, so all regions are shown at the same time in Figures 5.10(e) and 5.10(f).

By plotting $\log(1/\Omega_{np})$, where

$$\Omega_{np} = n\omega_\zeta - p\omega_\theta - \omega, \tag{5.8}$$

the resonant regions are highlighted as Ω_{np} tends to zero. By choosing the mode frequency to be the mode frequency at the peak amplitude $\omega = \omega(t = t_{sat})$ (considering at this point only the $n = 1$ internal kink mode), the resonant regions of phase space when the mode is at its saturation point are identified. For this example, $\omega(t = t_{sat}) = 8.28$kHz, see Figure 5.7. Regions resonant with the $n = 1$ mode are shown at low energy (20keV) and high energy (60keV) for both the co- and counter-launched particles in Figures 5.11(a) to 5.11(d). Plotted as lines in these figures, they are in fact surfaces in the three-dimensional phase space. These surfaces depict the regions of phase space which have become resonant at that time in the chirp. Through interaction with the waves, it is on these surfaces that the particles move, along lines defined by constant K given by Equation 2.63. The fishbone modes are low frequency compared to the ion cyclotron frequency ($\omega < \omega_c$). The result of this is that the interaction results predominantly in a change of canonical angular momentum P_ζ (rather than $\mathcal{E}$), which itself yields a radial redistribution of the fast ions from the assumption that $P_\zeta \sim -\psi_p$.

5.6.1 Resonant Particle Orbits

By taking a journey along one of the resonance lines, it is possible to plot the guiding centre orbits that are resonant with the $n = 1$ internal kink mode at a given

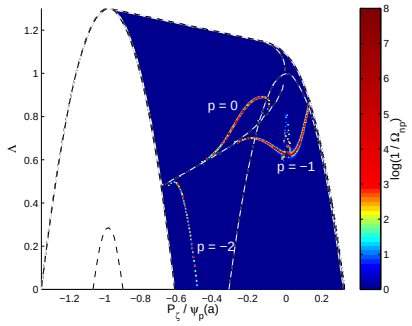

(a) Co-launched particles at $\mathcal{E} = 20$keV.

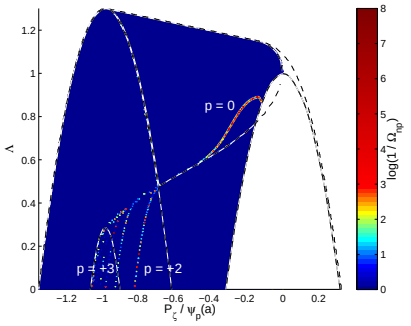

(b) Counter-launched particles at $\mathcal{E} = 20$keV.

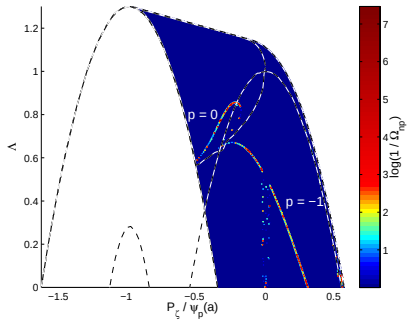

(c) Co-launched particles at $\mathcal{E} = 60$keV.

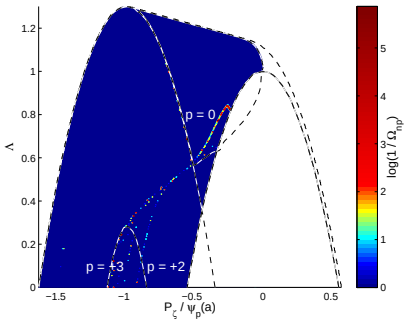

(d) Counter-launched particles at $\mathcal{E} = 60$keV.

Figure 5.11: Slices at different energies of $\log(1/\Omega_{np})$. The lines represent slices through surfaces in the $(\mathcal{E}, P_\zeta, \mu)$ CoM phase space which are resonant with the $n = 1$ internal kink mode at $\omega = 8.28$kHz. It is on these surfaces that the fast ions are redistributed through phase space by the mode.

frequency. The resonance line that has been chosen to do this along is made up of the $p = -1$ and $p = 0$ lines for the co-launched particles at $\mathcal{E} = 20$keV that is shown in Figure 5.11(a). To get an idea of where the resonance interacts with the fast ions, Figure 5.12 shows the resonance line superimposed onto the fast ion distribution function at $\mathcal{E} = 20$keV.

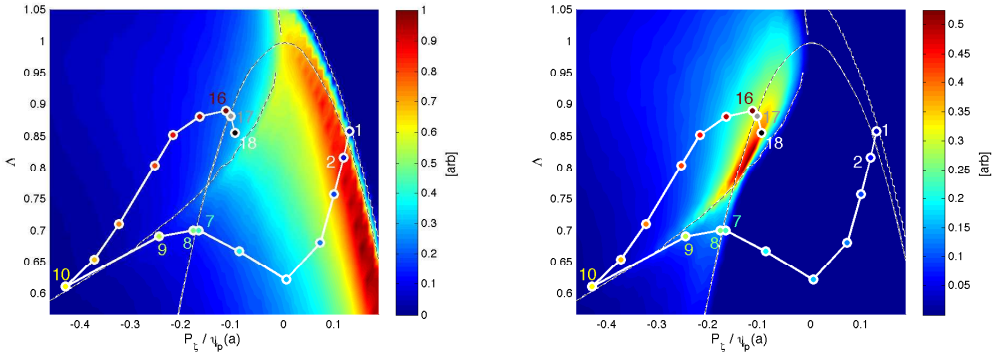

(a) Co-launched particles.

(b) Counter-launched particles.

Figure 5.12: A path along the $n = 1$, $p = -1, 0$ resonance line (taken from Figure 5.11(a)) is shown in white. This has been superimposed onto the fast ion distribution function for both co- and counter-passing orbits (identical to Figure 5.4) at $\mathcal{E} = 20$keV. The orbit of the particle at the location of each of the coloured dots is plotted in Figure 5.13.

By looking back at the orbit classifications shown in Figure 4.2, it is observed that the white line in Figure 5.12 passes through regions containing five different types of orbits. Starting in the stagnation orbit region at point 1 and ending in the potato orbit region at point 18, each of the orbits is plotted individually in Figure 5.13.

In addition to showing the orbits that are resonant with the mode, this figure also demonstrates the boundaries between the orbit classifications. In crossing from orbit number 1 to number 2, the particle goes from having a stagnation orbit (Figure 5.13(a)) to encircling the magnetic axis and becoming a co-passing orbit (Figure 5.13(b)). It the crosses into the counter-passing region (Figure 5.13(c)), in which its value of σ_d changes from negative to positive. Next, the line passes through the trapped-passing boundary, as the particle experiences a bounce in its orbit due to the magnetic mirror effect (Figure 5.13(d)). The point at which the particle no longer encircles the magnetic axis is shown as it passes into the potato orbit region (Figure 5.13(e)). The density of particles which posses the orbits plotted here is given by the magnitude of the fast particle distribution function at that location in the CoM phase space.

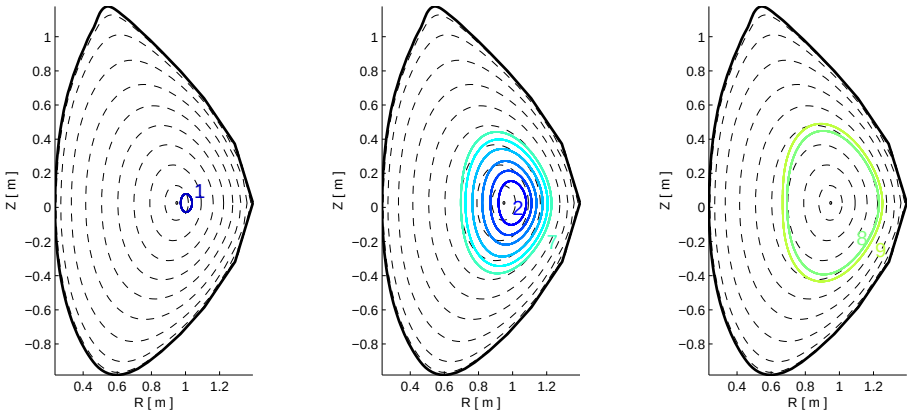

(a) Stagnation Orbit (1) (b) Co-passing Orbits (2-7) (c) Counter-passing Orbits (8-9)

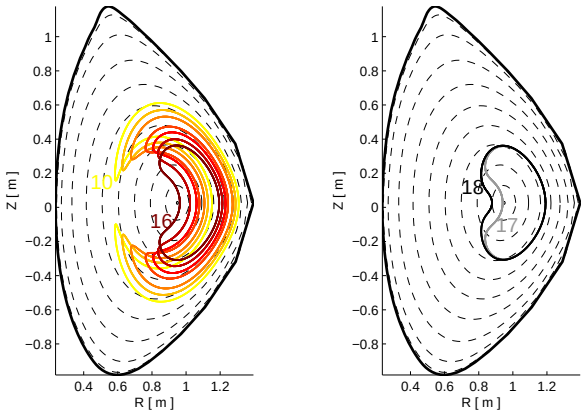

(d) Trapped Orbits (10-16) (e) Potato Orbits (17-18)

Figure 5.13: Guiding centre orbits of resonant particles.

5.6.2 Effect of Frequency Sweeping on Resonant Regions of Phase Space

The chirping nature of the fishbone mode means that the frequency sweeps downwards during the burst. Because of a changing mode frequency ω in Equation 5.8, the resonant regions of phase space are not static and move through phase space with different locations becoming resonant at different times during the burst. The effect that the frequency chirp has on the resonances is shown in Figure 5.14, whereby their time dependence is depicted. By looking back at Figure 5.4, it is shown that the resonant regions intersect with regions of significant fast ion density at this energy. It is where the resonant regions intersect the largest gradients in P_ζ of the

distribution function that the strongest mode drive is experienced.

It is this figure which is important when considering the varying mode amplitude (the bursting nature) of the mode. When the resonant region overlaps with the strongest gradients in the distribution function, the drive will be strongest. If this coincides with the time that the mode amplitude is largest (the maximum of the black line in Figure 5.7) then the redistribution of the fast ions will be the greatest. The effect of changing the bursting window of the mode is investigated in Section 6.5.4, and is shown to give largest redistribution when they overlap.

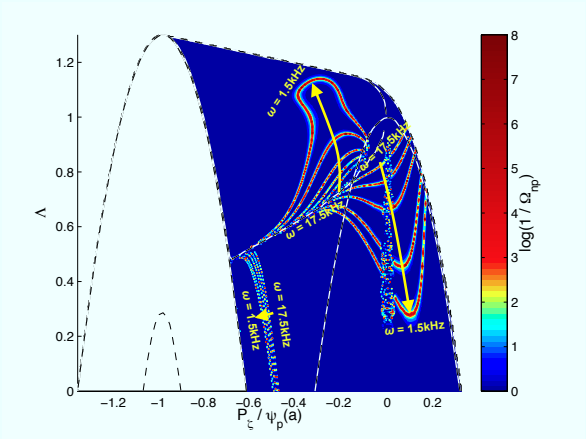

(a) Co-launched particles at $\mathcal{E} = 20$keV.

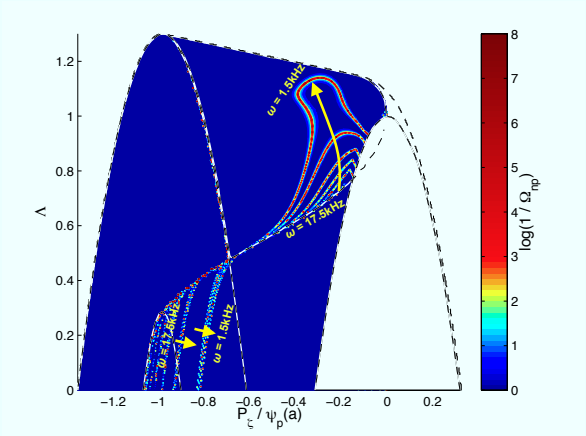

(b) Counter-launched particles at $\mathcal{E} = 20$keV.

Figure 5.14: The regions of phase space resonant with the mode at five equally spaced times throughout the chirp, corresponding to five different mode frequencies. The chirp sweeps down from 17.5kHz to 1.5kHz (shown in Figure 5.7). The region swept out encompasses the region of high fast-ion density shown in Figure 5.4 at $\mathcal{E} = 20$keV.

5.6.3 n > 1 Resonances

By interpreting the $n > 1$ modes shown in the spectrogram image for this shot (Figure 3.4) as independent toroidal mode eigenfunctions, they will contribute separately to which regions of phase space become resonant with the mode, so it is necessary to look at where these resonances occur in phase space. Additionally, this investigation is of relevance for tokamak discharges in which only $n > 1$ are present. To find the resonances, the same treatment as for $n = 1$ mode has been applied. The modes sweep at higher frequency for these harmonics and the frequency at peak amplitude for each of the next three modes is $\omega_{\mathrm{k}=2}(t = t_{sat}) = 16.56\mathrm{kHz}$, $\omega_{\mathrm{k}=3}(t = t_{sat}) = 24.84\mathrm{kHz}$ and $\omega_{\mathrm{k}=4}(t = t_{sat}) = 33.12\mathrm{kHz}$. The regions of phase space that come into resonance with these modes are shown in Figure 5.15. It is important to note however that they are decreasing in amplitude (see Section 5.4.3) so will have less effect in redistributing the fast ions.

For shots where only higher mode number instabilities are seen, this technique can demonstrate why they cause a different amount of redistribution than the $n = 1$ mode, due to interaction with different parts of the distribution function. An example of this is when the radial fast ion diffusivity is reduced from 2-3$\mathrm{m^2s^{-1}}$ in the presence of $n = 1$ chirping modes to 0.5$\mathrm{m^2s^{-1}}$ in the presence of $n = 2, 3$ chirping modes by moving the NBI beam off-axis [154].

The overlap of wave-particle resonances will be of significant importance on ITER, where due to the ratio of typical gyroradius to minor radius of the device ($\rho_a/a \sim 10^{-3}$ to 10^{-2}, compared to $\sim$0.1 in current devices) will require multiple resonant modes in order to provide global transport across the minor radius [110].

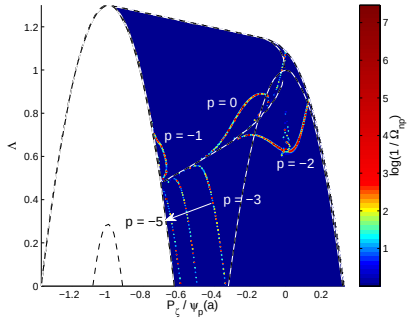

(a) n=2 (co-propagating).

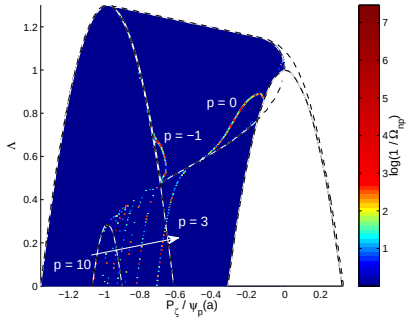

(b) n=2 (counter-propagating).

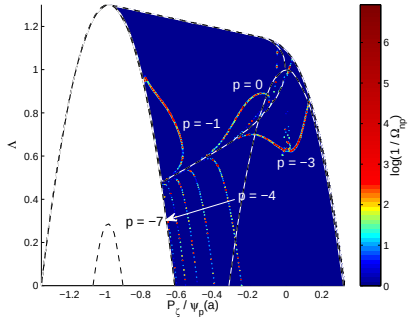

(c) n=3 (co-propagating).

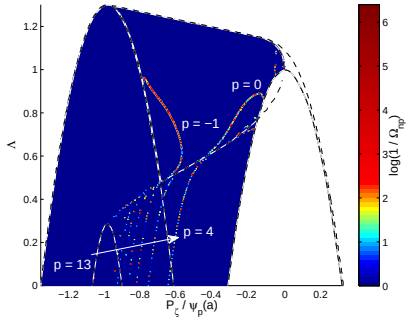

(d) n=3 (counter-propagating).

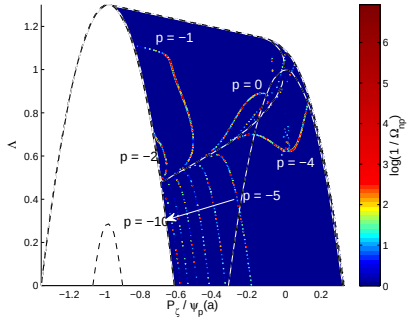

(e) n=4 (co-propagating).

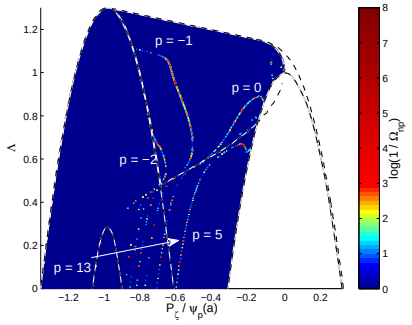

(f) n=4 (counter-propagating).

Figure 5.15: Regions of CoM phase space that come into resonance with the fast ions for the $n > 1$ harmonics at $\mathcal{E} = 20$keV. The frequency used for each is $\omega_k(t = t_{\text{sat}}) = n\omega_{k=1}(t = t_{\text{sat}})$

5.6.4 Resonant s - λ Phase Space

The CoM phase space plots show which parts of phase space are resonant with the mode. In order to get a better idea of where the resonances lie radially and in pitch angle, it is informative to plot them in an alternative phase space format. The coordinates for this are energy, normalised radius and pitch angle, $(\mathcal{E}, s, \lambda)$ This representation of the phase space can once again be split up into regions which represent different types of orbits, as was the case for the CoM phase space in Figure 4.2. The orbit types in this space is shown in Figure 5.16. The bottom half of this figure represents the co-propagating particle orbits and the top half represents the counter-propagating orbits. It has been plotted along side the radial profile of the mode eigenfunction for the $n = 1$ kink mode used to model the fishbone and gives a good physical understanding of which orbit types are present at the peak mode displacement. The figure shows that the eigenfunction peaks in a region where co, counter and trapped orbits can all exist. The distribution function however is strongly peaked in the co-passing and trapped region.

By following the same procedure as before, the resonant regions are determined in terms of the radius and pitch angle, as plotted in Figure 5.17. The co-launched particles have a negative pitch angle. The $n = 1$ kink mode is again shown below the figure. The peak of the mode corresponds to resonances in both the trapped ($p = 0$) and passing ($p = $ -1) regions.

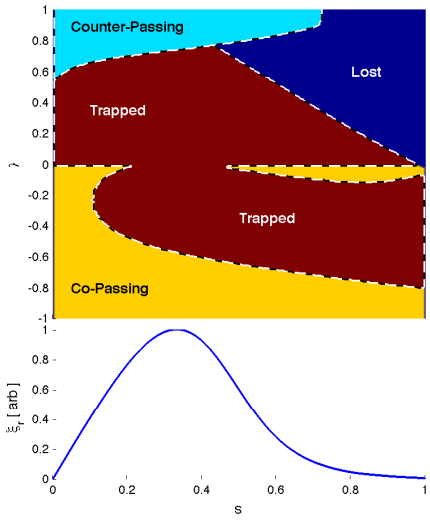

Figure 5.16: Orbit types in $(\mathcal{E}, s, \lambda)$ phase space. Co-passing particles have $\lambda < 0$ and counter-passing particles have $\lambda > 1$. The radial mode structure of the dominant harmonic is shown to give an idea of which types of particles are present at its peak.

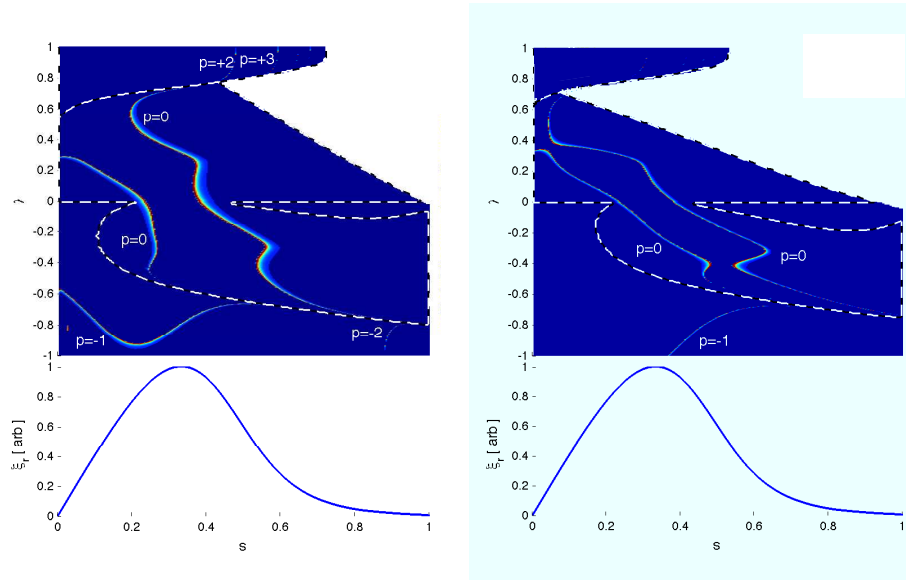

(a) 20keV. (b) 60keV.

Figure 5.17: The resonant regions as a function of s and λ for two energy levels in MAST shot #27920 at 230ms. The orbit classification boundaries and the resonances present at $\omega = 8.28$kHz are shown, and can be compared to the mode eigenfunction plotted underneath.

5.7 Relevance to MAST-Upgrade

The impending MAST-U device [155] is due to begin operation in 2015 [156]. Stage one of the upgrade will feature a new off-axis NBI that will raise the beam power from < 5.0MW to < 7.5MW. This should triple the energy deposited into the plasma and coincide with an increased pulse length of up to four seconds in the new device. The second beam will be vertically off-axis by 0.65m [157].

The fast ions deposited by the off-axis beam will peak at a radius of $s \sim 0.7$ and are injected co-current, with the peak in the pitch angle at $\lambda \sim -0.9$. The slice of $s - \lambda$ phase space described in the previous section provides a good platform on which to visualise the combined on and off-axis beam fast ion distribution function in MAST-U and determine if the EPs injected by the off-axis beam will be resonant with modes driven by the on-axis beam. Although MAST-U will have a different equilibrium, some qualitative conclusions may be drawn by revisiting Figure 5.17. If the resonances in MAST-U are in the same location to those found in this figure using a MAST equilibrium, it suggests that the fast ions will be injected into a region of phase space that may coincide with the n=1 resonance at 8.27 kHz for p

= -2 or $p = 0$ (for the trapped particles). For similar chirping modes in MAST-U, this could lead to further drive of the mode if the gradients in the off-axis beam contribute to the drive of this mode.

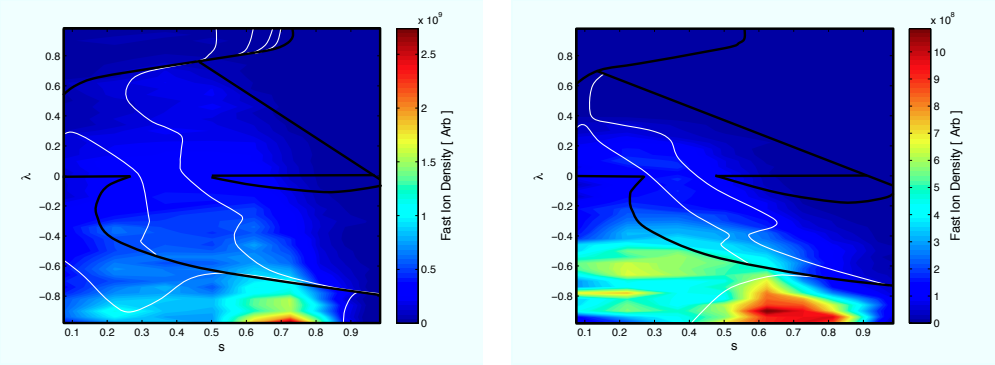

(a) 20 keV (b) 60 keV

Figure 5.18: Slices through a MAST-U fast ion distribution function for Scenario A1 with core scope beams (RunID `K25`) at high and low energy. In this scenario, each beam injects 2.5MW of power. The on-axis beam is focused in the plasma core ($s \lesssim 0.3$), and the second (off-axis) beam is centred around a radius of $s = 0.7$. To make predictions, the orbit classification regions (black) and lines that will be resonant with the fishbone mode (white) in MAST are over plotted. Note that since a MAST equilibrium was used to find these, they will be in different locations in MAST-U so should be used as a guide only.

Figure 5.18 shows a slice through a fast ion distribution function for MAST-U at $\mathcal{E} = 20$ keV and $\mathcal{E} = 60$ keV in s-λ space. Despite using a different equilibrium, this allows general comparisons to be drawn with the regions of phase that are resonant with the fishbone mode driven unstable by the on-axis beam in MAST. It shows that the fast ion density resulting from the off-axis beam is in a region broadly located as far away from a resonance with the modes driven unstable by the on-axis beam as possible. There is still some overlap, such that it is likely the fishbones will cause some redistribution of the fast ions resulting from the off-axis beam.

5.8 Summary

This chapter has described in detail the process building up the MAST fishbone model, and how each of the codes required have been used in a consistent way. The precise equilibrium, perturbation and fast ion distribution function present in MAST shot `#27920` at 230ms have been determined and the method used to

evolve the mode has been described. From this, the regions of the phase space that are resonant with the mode have been identified, and shown to coexist with steep gradients of the distribution function. By visualising the fast ions that are resonant with the mode, this technique has also been used as a predictive tool for the additional off-axis beam that will be present in MAST-U.

In the next chapter the resulting redistribution of the fast ions caused by the fishbone mode will be shown. This redistribution will be parameterised in a way that enables comparison with other research, and compared directly to experimental observations via the use of synthetic diagnostics.

Chapter 6

Fast Ion Redistribution and Transport Coefficients

The interaction between the fast ions and the perturbed wave field in the tokamak results in nonconservation of $\mathcal{E}$ and P_ζ. Due to this, the fast ions are transported away from the hot core and even lost from the plasma altogether. Simulations have been run using HAGIS in order to quantify the redistribution and loss of these particles, and the effect this has on the plasma discharge. The level of anomalous transport of the particles observed during these simulations is quantified by means of diffusive and convective transport coefficients.

6.1 Radial Fast Ion Redistribution

In HAGIS, the fast ion density $n_\mathrm{f} = \int f \ \mathrm{d}^3v$ cannot be found directly, since the phase space is split up simultaneously into both physical and velocity space (it is $\mathrm{d}\Gamma = \mathrm{d}^3x \ \mathrm{d}^3v$ that is known, not d^3x and d^3v individually - see Section 4.1.1). For this reason, it is necessary to bin the radial fast ion density out by dividing the number of particles represented by each simulation marker into concentric radial volume bins,

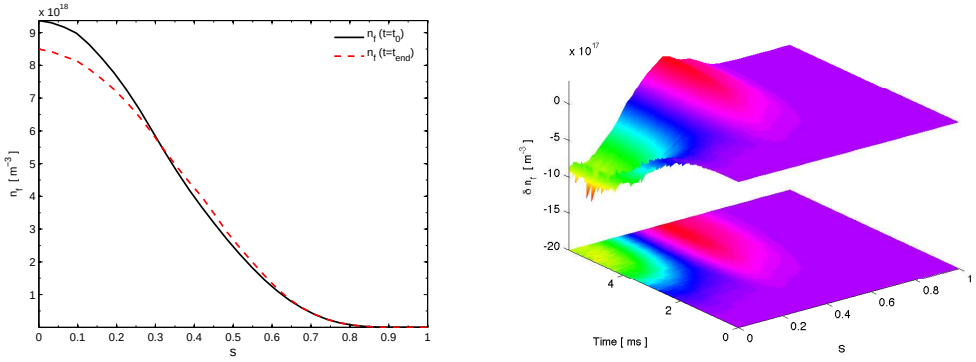

(a) Radial fast ion density before (black, solid line) and after (red, dashed line) the fishbone perturbation.

(b) Change in fast ion density as a function of time and radius.

Figure 6.1: Fast ion redistribution for an $n = 1$, $m =$ -1 mode of peak amplitude $\delta B/B = 1{\times}10^{-3}$.

$$
\begin{aligned}
n_{\mathrm{f}}(\psi_p, t) &= n_{\mathrm{f},0}(\psi_p) + \delta n_{\mathrm{f}}(\psi_p, t) \\
&= \frac{\int f_0 \, \mathrm{d}\Gamma^{(p)}}{\int \mathrm{d}^3 x} + \frac{\int \delta f \, \mathrm{d}\Gamma^{(p)}}{\int \mathrm{d}^3 x} \\
&\simeq \frac{\sum_{j=1}^{N_j} \; f_{0,j} \left(\psi_{p,x} \to \psi_{p,x} + \Delta\psi_{p,x}\right) \; \Delta\Gamma_j^{(p)}}{\Delta V_x} \\
&\quad + \frac{\sum_{j=1}^{N_j} \; \delta f_j \left(\psi_{p,x} \to \psi_{p,x} + \Delta\psi_{p,x}\right) \; \Delta\Gamma_j^{(p)}}{\Delta V_x}
\end{aligned}
\tag{6.1}
$$

where ΔV_x is the x^{th} volume bin, which effectively makes up a shell between flux surfaces located at $\psi_{p,x}$ and $\psi_{p,x} + \Delta\psi_{p,x}$ into which the markers in that range are put in order to find the fast ion density.

The redistribution of the fast ions by the fishbone mode results in a flattening of the radial density profile. The centrally (core) peaked initial distribution from LOCUST-GPU of fast ions is binned out and shown as a function of radius in Figure 6.1(a) - this is akin to making a flux-surface average approximation of the density (the density is not a flux surface quantity due to the high trapped particle fraction on the LFS). Following an $n = 1$, $m = -1$ perturbation evolved temporally as shown in Figure 5.7 the final radial fast ion density is shown in Figure 6.1(a). This change to the distribution function $\delta n_{\mathrm{f}}(t) = n_{\mathrm{f},0} - n_{\mathrm{f}}(t)$ is shown as a function of time and radius throughout the chirp in Figure 6.1(b). The core fast ion density for a mode of peak perturbation amplitude $\delta B/B = 1 \times 10^{-3}$ is shown in this figure

to drop by 9% from $9.37\times10^{18}\mathrm{m}^{-3}$ to $8.50\times10^{18}\mathrm{m}^{-3}$.

6.1.1 Higher Poloidal Mode Harmonics

The dominant poloidal mode number for the $n = 1$ mode found during the linear stability calculations using MISHKA was $m = -1$. The model has been expanded to additionally include the higher poloidal mode numbers, shown in Figure 5.6(a). Higher poloidal mode harmonics have always been associated with fishbone modes, ever since their initial observation [43]. The second largest poloidal harmonic for the $n = 1$ mode is $m = -2$, which is located radially further out. To gain a better physical understanding of what this means, see Figure 2.3 which shows examples of what the toroidal displacement caused by modes of exaggerated amplitude schematically look like.

The linear stability calculation determined modes for $-6 < m < -1$. The inclusion of the higher poloidal harmonics in the simulation is shown to actually reduce the redistribution by ∼8% to the level shown by the blue line in Figure 6.2; the change in density for the $n = 1$, $m = -1$ mode is also plotted for comparison. An explanation for the reduction in the level of redistribution of the fast ions is that of the new poloidal harmonics, it is the $m = -2$ that is most significant. This is located radially further out (on the $|q| = 2$ surface - see Equation 2.48), as shown in Figure 5.6(a). The location of its peak is radially located in the region that the $n = 1$, $m = -1$ mode has redistributed the fast ions to, hence it appears to be causing secondary redistribution of the already redistributed fast ions, some of which are moved radially back towards the core.

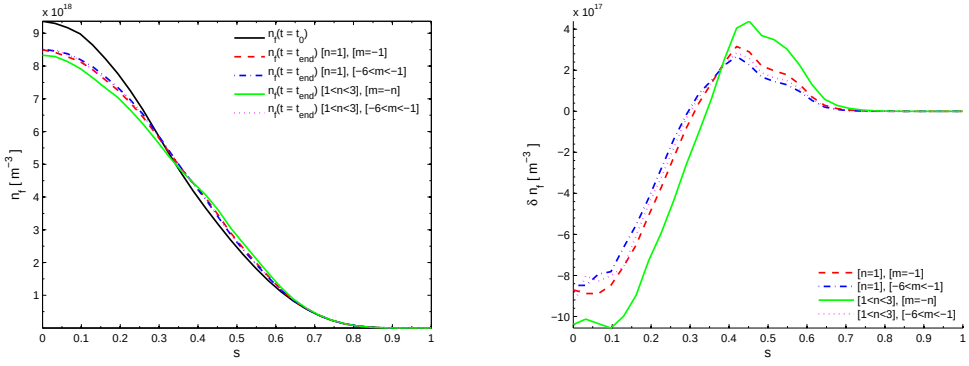

(a) Radial fast ion density n_f.

(b) Change in radial fast ion density δn_f

Figure 6.2: Radial fast ion redistribution due to a fishbone of amplitude $\delta B/B = 1 \times 10^{-3}$. The effect of including different toroidal and poloidal mode harmonics is shown.

6.1.2 Higher Toroidal Mode Harmonics

As explained previously in Section 3.6.1, it is possible to interpret the higher toroidal mode harmonics that are observed in the spectrograph (Figure 3.4) as independent $n > 1$ mode eigenfunctions. The dominant poloidal harmonic for each of these was shown in Figure 5.6 to be when $m = -n$. In order to quantify the effect of the higher toroidal mode harmonics, they were first included as the just dominant mode, i.e. $n = 1$ $m = -1$, $n = 2$ $m = -3$ and $n = 3$ $m = -3$. This led to a fast ion redistribution at a level that was 20% larger than with just the $n = 1$, $m = -1$ mode, with the core density dropping by 11%, shown in Figure 6.2. Following this, all of the m harmonics were also included in the simulation of all the toroidal mode harmonics. This had the same effect as when just the $n = 1$ mode was studied; there was subsequent secondary redistribution such that the core density dropped by 10% during the simulation.

The contribution from the relatively small amplitude higher toroidal mode harmonics have been shown to provide little extra drive for the fishbone mode. The amplitude scaling will be investigated in Section 6.5.2, but for the modelling presented in the majority of the remainder of this thesis only the dominant $n = 1$, $m = -1$ mode will be considered.

6.1.3 Energy Dependence of Redistribution

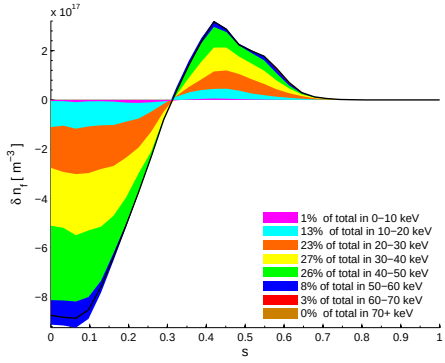

Figure 6.3: Radial fast ion redistribution split into energy levels for an $n = 1$, $m = -1$ fishbone mode of amplitude $\delta B/B = 1 \times 10^{-3}$.

The fast ion redistribution for the $n = 1$, $m = -1$ fishbone mode that was plotted in Figure 6.2(b) has been replotted in Figure 6.3, this time divided into bins representing the energy of the fast ion. Integrating over energy recovers the result found in the original figure. Three quarters of the redistributed ions have energy

between 20 - 50 keV. Only 11% of the total redistributed ions have energy above 50keV. This is significant, as the nonlinear dependence between energy and reaction cross section means that only particles within this energy region contribute to the neutron diagnostics (see section 7.3). The total redistribution in Figure 6.3 is given by the black line. This is shown to be within the blue area of ions with energy between 50 - 60 keV, such that the figure shows that these ions are in fact moved radially inwards by the mode.

6.2 Fast Ion Redistribution in CoM Phase Space

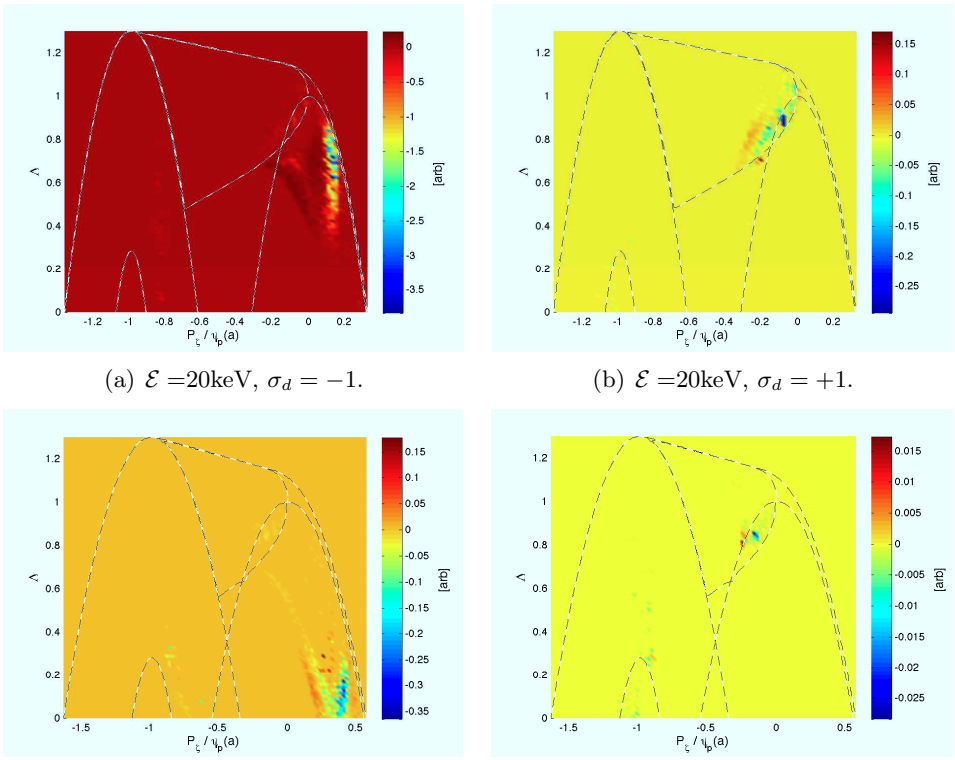

(a) $\mathcal{E}$ =20keV, $\sigma_d = -1$.

(b) $\mathcal{E}$ =20keV, $\sigma_d = +1$.

(c) $\mathcal{E}$ =60keV, $\sigma_d = -1$.

(d) $\mathcal{E}$ =60keV, $\sigma_d = +1$.

Figure 6.4: Fast ion redistribution in terms of the CoM space at different energies. The redistribution occurs when the fast ion distribution function coincides with regions that are resonant with the mode.

Slices of the redistribution of the fast ions in $(\mathcal{E}, P_\zeta, \mu)$ space are shown in Figure 6.4 for both low energy ($\mathcal{E}$ = 20 keV) and high energy ($\mathcal{E}$ = 60 keV). This shows how in the presence of the perturbation these quantities are no longer constant throughout the orbit. The redistribution is shown to occur where the resonant regions sweeping through phase space (Figure 5.14) coincide with areas of

significant fast ion density (Figure 5.4). It is the gradient in the density that drives the redistribution. Note that the redistribution is largest around the resonant regions that occur during the peak in the mode amplitude, shown in Figure 5.11.

Redistribution of fast ions is shown to occur from small regions of phase space, spread out into larger regions. This is because only small areas are significantly resonant with the mode at any one time, but the duration of the resonance changes such that the particles are re-located into different areas. Redistribution occurs along lines defined by Equation 2.63, so particles also travel through the energy dimension of which these figures are slices.

6.3 2D Fast Ion Redistribution

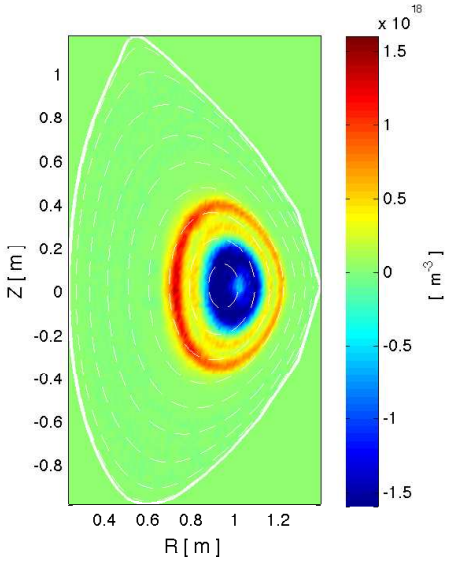

Figure 6.5: Fast ion redistribution projected onto a poloidal cross section of the plasma (integrated toroidally) for a fishbone mode of amplitude $\delta B/B = 1 \times 10^{-3}$.

It is possible to show the redistribution of the fast ions in terms of the change in density of the 2D poloidal cross section of the plasma, integrated toroidally. The density of fast ions cannot be found directly from the distribution function directly using $n_f = \int f \mathrm{d}^3 v$ since the volume element $\mathrm{d}^3 v$ is not known. To find the density, it is therefore necessary to determine the number of particles represented by each marker in the simulation, and bin them out onto an (R, Z) grid for which the volume

of each bin is known,

$$\delta n_{\rm f}(R,Z) = \frac{\int \delta f \mathrm{d}\Gamma^{(p)}}{\int \mathrm{d}^3 v} = \frac{\delta N_{\rm f}(R,Z)}{V(R,Z)} = \frac{\sum_{j=1}^{N_j} \delta f_j \, \Delta\Gamma_j^{(p)}}{\Delta V(R,Z)} \, .$$

An example of this is shown in Figure 6.5. The drop in the core fast ion density is shown, and the fast ions are redistributed radially outwards.

6.4 Transport Coefficients

In order to draw comparisons to other codes and observations it is necessary to find a way to quantify the level of anomalous fast ion redistribution. This can be done by means of anomalous transport coefficients. Anomalous fast ion transport is driven by temperature and density gradients in the EP population.

Transport of fast particles is commonly expressed as a sum of a diffusive term and a convective term [16],

$$\boldsymbol{\Gamma} = -D\boldsymbol{\nabla} n_{\rm f} - V_p n_{\rm f} \tag{6.2}$$

where D is the diffusivity and V_p represents a convective inward pinch. It is not possible to simultaneously determine both D and V_p; to do so transient measurements are required, for example the use of a gas puff into the plasma [16]. What can be done is to consider the two coefficients separately, assuming independently that the transport is purely diffusive or purely convective. This results in two independent equations for the radial transport

$$D_r = -\frac{\Gamma_r}{\partial n_{\rm f}/\partial r} \tag{6.3}$$

$$V_{p,r} = -\frac{\Gamma_r}{n_{\rm f}} \, , \tag{6.4}$$

where the subscript r denotes transport in the outward radial direction. In order to estimate values for D_r and $V_{p,r}$, both the particle flux and the density of the plasma must be determined as a function of radius. The density is given by Equation 6.1 and the covariant particle flux in the ψ_p direction is given by

$$\Gamma_{\psi_p} = n_{\rm f} v_{\psi_p} \, . \tag{6.5}$$

In HAGIS coordinates the velocity is expressed in terms of the $i^{\rm th}$ contravariant

basis vector $\frac{\partial \mathbf{x}}{\partial \xi^i}$ (where $\xi^1 \equiv \psi_p$, $\xi^2 \equiv \theta$, $\xi^3 \equiv \zeta$) as

$$\begin{aligned}
\mathbf{v} = \frac{\mathrm{d}\mathbf{x}}{\mathrm{d}t} &= \frac{\partial \mathbf{x}}{\partial \xi^i}\frac{\mathrm{d}\xi^i}{\mathrm{d}t} \\
&= \frac{\partial \mathbf{x}}{\partial \psi_p}\frac{\partial \psi_p}{\partial t} + \frac{\partial \mathbf{x}}{\partial \theta}\frac{\partial \theta}{\partial t} + \frac{\partial \mathbf{x}}{\partial \zeta}\frac{\partial \zeta}{\partial t} \\
&= \frac{\partial \mathbf{x}}{\partial \psi_p} v^{\psi_p} + \frac{\partial \mathbf{x}}{\partial \theta} v^{\theta} + \frac{\partial \mathbf{x}}{\partial \zeta} v^{\zeta} \ .
\end{aligned}$$

The conversion of this into the covariant form required in Equation 6.5 to determine the particle flux is given by

$$\begin{aligned}
v_{\psi_p} = \mathbf{v} \cdot \frac{\partial \mathbf{x}}{\partial \psi_p} &= \frac{\partial \mathbf{x}}{\partial \psi_p} \cdot \frac{\partial \mathbf{x}}{\partial \xi^i} v^i \\
&\simeq \mathrm{g}_{\psi_p \psi_p} v^{\psi_p} \\
&= \mathrm{g}_{\psi_p \psi_p} \dot{\psi_p} \ ,
\end{aligned}$$

where covariant components of the HAGIS metric tensor $\mathbf{g}$ are given by

$$\mathrm{g}_{ij} = \frac{\partial \mathbf{x}}{\partial \xi^i} \cdot \frac{\partial \mathbf{x}}{\partial \xi^j} \ ,$$

which is calculated from contravariant metric tensor elements in the code for each marker using

$$\mathrm{g}_{\psi_p \psi_p} = \mathcal{J}^2 (\mathrm{g}^{\theta\theta}\mathrm{g}^{\zeta\zeta} - \mathrm{g}^{\theta\zeta}\mathrm{g}^{\zeta\theta}) \ .$$

The plasma density is given by Equation 6.1, and radial particle flux is calculated in the same way

$$\begin{aligned}
\Gamma_{\psi_p}(\psi_p, t) &= \Gamma_{\psi_p,0}(\psi_p) + \delta\Gamma_{\psi_p}(\psi_p, t) \\
&= \frac{\int f_0 \ \mathrm{g}_{\psi_p\psi_p} \ \dot{\psi_p}(t = t_0) \ \mathrm{d}\Gamma^{(p)}}{\int \mathrm{d}^3 x} + \frac{\int \delta f \ \mathrm{g}_{\psi_p\psi_p} \ \dot{\psi_p}(t) \ \mathrm{d}\Gamma^{(p)}}{\int \mathrm{d}^3 x} \\
&\simeq \frac{\sum_{j=1}^{N_j} \delta f_j \ (\psi_{p,x} \rightarrow \psi_{p,x} + \Delta\psi_{p,x}) \ \mathrm{g}_{\psi_p\psi_p,j} \ \dot{\psi_{p,j}}(t) \ \Delta\Gamma_j^{(p)}}{\Delta V_x} \ ,
\end{aligned}$$

where the initial radial particle velocity is zero $\dot{\psi_p}(t = t_0) = 0$, and $\mathrm{g}_{\psi_p\psi_p,j}$ is the value of $\mathrm{g}_{\psi_p\psi_p}$ at the location of the j^{th} particle. In order to find the physical radial component of the flux Γ_r from the covariant form, the standard formula for covariant vector components can be used

$$\Gamma_r = \Gamma_i \frac{\partial x_i}{\partial r}$$

such that the physical radial component of the flux is

$$\Gamma_r = \Gamma_{\psi_p} \frac{\partial \psi_p}{\partial r} \ .$$

An equivalent expansion for the radial density gradient is

$$\frac{\partial n_\mathrm{f}}{\partial r} = \frac{\partial n_\mathrm{f}}{\partial \psi_p} \frac{\partial \psi_p}{\partial r} \ .$$

The subsequent equations required to determine the transport coefficients are

$$D_r = -\frac{\Gamma_{\psi_p}}{\partial n_\mathrm{f}/\partial \psi_p} \tag{6.6}$$

$$V_{p,r} = -\frac{2\psi_p(a) r \Gamma_{\psi_p}}{n_\mathrm{f} a^2} \ , \tag{6.7}$$

where the relation $r = a(\psi_p/\psi_p(a))^{1/2}$ has been used to find

$$\frac{\partial \psi_p}{\partial r} = \frac{2\psi_p(a) r}{a^2}$$

which is required in Equation 6.7.

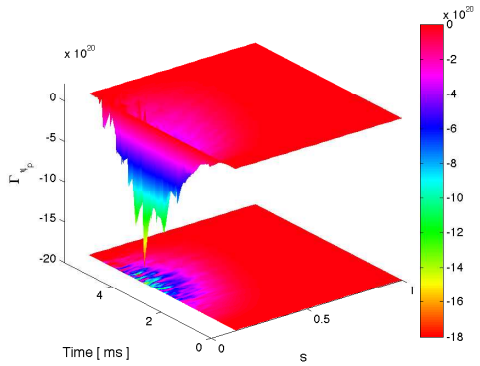

Figure 6.6: Covariant radial particle flux averaged over 0.09ms.

The covariant radial particle flux Γ_{ψ_p} for the fishbone mode studied with a mode amplitude of $\delta B/B = 1{\times}10^{-3}$ is shown in Figure 6.6, averaged over 0.09ms (to reduce the noise level from the HAGIS simulation). It is not well defined on the magnetic axis, which may be interpreted as physically viable as a radial flux out of a line along the magnetic axis is not possible since there is no fast particle source there. For this reason, the flux for $\psi_p < 0.1$ is not plotted. The covariant particle flux in the figure is shown to grow and then decay in the same way as the mode burst, and is responsible for the fast ion redistribution. Using this covariant

particle flux, along with the fast ion density, the diffusive and convective transport coefficients can be determined using Equations 6.6 and 6.7. These coefficients are calculated independently, in each case assuming the other to be zero; in reality, the physical process is a combination of the two. The temporal and radial dependence of these particle transport coefficients is shown in Figure 6.7.

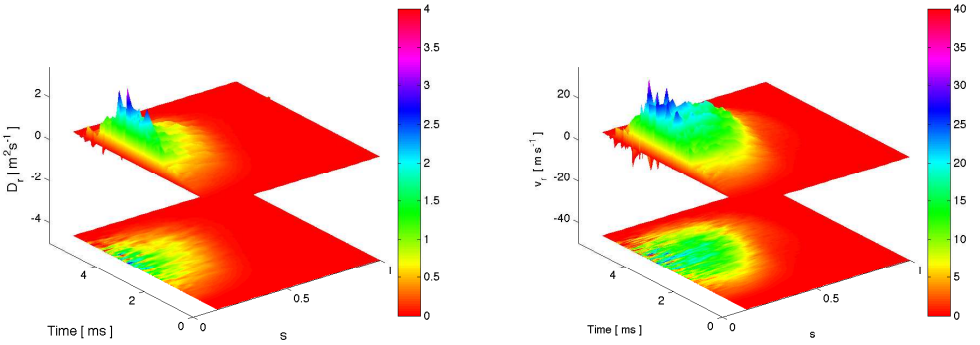

(a) D_r averaged over windows of 0.09ms. (b) $|V_{p,r}|$ averaged over windows of 0.09ms.

Figure 6.7: Transport coefficients for a $n = 1$, $m = -1$ mode of peak amplitude $\delta B/B = 1{\times}10^{-3}$.

Figure 6.7(a) shows a sustained particle diffusivity of $D_r > 0.6$ m^{2}s^{-1} for ~3.5ms out to a radius of ~0.45. This is comparable to typical a TRANSP run, in which an *ad hoc* model is used with an anomalous radial diffusivity that is constant in t, s and $\mathcal{E}$ applied across the core of the plasma [158]. This is scaled in order to observe the required levels of fast ion redistribution. In addition to the broad $D_r > 0.6$ m^{2}s^{-1}, there is a peak in the diffusion coefficient of 3.0 m^{2}s^{-1}. In previous work [159], it was this peak in the coefficient that was quoted - such that a relative mode amplitude of $\delta B/B$ ~$1{\times}10^{-2}$ was required to hit a peak of 0.5 m^{2}s^{-1}. For this new modelling it is shown that for an on-axis beam distribution function the diffusivity can reach this level across a broad radius for a sustained time period at a much more reasonable fishbone mode amplitude of $\delta B/B = 1{\times}10^{-3}$. This value is more reliable than the previous result as a far more in-depth analysis of the MAST fishbone mode has been made. This has been facilitated by using more accurate representation of the instability. Sources for this include the LOCUST-GPU distribution function, a metric tensor that is a function of poloidal angle $g_{\psi_p\psi_p}(\theta)$, a corrected profile of the initial fast ion density $n_{f,0}$, being able to closer compare the modelling to the experiment using synthetic diagnostics (see Chapter 7) and the ability to interpret the redistribution by identifying which parts of the fast ion distribution function are resonant with the mode during the chirp. The scaling of the transport coefficients

will be discussed in detail in Sections 6.5.1-6.5.5, where the reasons behind the scaling are also discussed using the resonance figures (this was not addressed in [159]).

6.5 Parameter Scaling

The identification of the transport coefficients allows various controlled parameters to be scaled in order to determine their effect on the redistribution of the fast ions. Quantifying how the diffusivity scales these parameters provides an insight into which fishbones are most detrimental to the plasma.

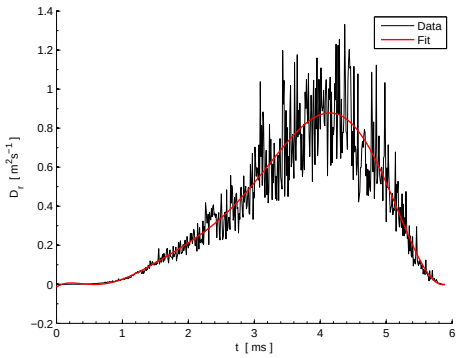

Figure 6.8: Fit to the radial diffusivity used to find its peak value along with an associated error for fishbone with mode amplitude $\delta B/B = 3 \times 10^{-4}$.

The redistribution of the fast ions has been shown to be a function of both time and radius. In order to perform parameter scaling, it is necessary to pick a consistent criterion by which to quantify the level of redistribution. The diffusivity has been shown to be a good way of quantifying the redistribution, so this has been chosen at its 'peak' value during the burst. The diffusivity signal is noisy in time, so the peak value is determined from an 8^{th}-order polynomial fit to the raw diffusivity as a function of time (with no time averaging applied). This also provides an associated error, which is found as an estimate of the standard deviation of the fit to the diffusivity at that time during the burst. An example is shown in Figure 6.8. The peak diffusivity here is $2.9 \pm 0.6\text{m}^2\text{s}^{-1}$ which occurs at $t = 3.8$ms, $t = 0.4$ms after $t = t_{\text{sat}}$.

6.5.1 Mode Amplitude

The typical relative mode amplitude of fishbones on MAST is in the region $10^{-4} < \delta B/B < 10^{-2}$. The peak radial diffusivity $D_{r,\text{peak}}$ is found for these mode amplitudes

and plotted in Figure 6.9(a). The straight line fit in this figure shows that the diffusivity scales as a power law. When written in the form

$$D_{r,\text{peak}} = a\left(\frac{\delta B}{B}\right)^{b} + c\ , \tag{6.8}$$

the values of the fit coefficients are $a = 7190$, $b = 1.16$ and $c = 0.30$. The power (coefficient b) is almost unity, suggesting a near-linear scaling of the diffusivity with mode amplitude. Transport codes such as TRANSP require a sustained diffusion coefficient over a significant radius, typically $0.0 < r < 0.5$ for a long time period of up to 0.5s (such that these simulations incur many fishbone modes, unlike the modelling presented in this thesis which focuses on a single mode). The sustained level is lower than this, as shown in Figure 6.7(a). The HAGIS modelling presented here confirms that the levels of anomalous radial diffusivity required by TRANSP of D_r between $0.5\text{m}^2\text{s}^{-1}$ and $3.0\text{m}^2\text{s}^{-1}$ may be explained by a fishbone of mode amplitude between $\delta B/B \sim 1 \times 10^{-3}$ and 5×10^{-3}. Figure 6.9(b) shows that the

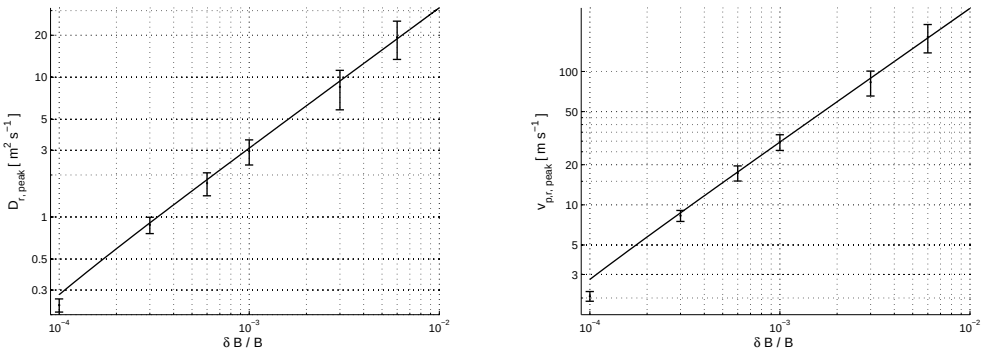

(a) Radial diffusivity.

(b) Radial convection (pinch) velocity.

Figure 6.9: Log-log plots of the transport parameter scaling with fishbone mode amplitude.

peak in the convective transport coefficient also scales in the same way as the peak in the diffusive transport coefficient. The straight line fit in this figure shows that the like the diffusivity, the pinch velocity scales as a power law. By employing a similar technique to the one used to find the scaling of the diffusivity, an equivalent fit equation to Equation 6.8 yields the coefficients $a = 4920$, $b = 1.10$ and $c = 1.95$. This again suggests a near-linear scaling of the pinch velocity with mode amplitude.

6.5.2 Mode Amplitude (All Harmonics)

The effect of the additional poloidal and toroidal mode harmonics of the fishbone on the anomalous radial fast ion diffusivity caused are shown in Figure 6.10. This figure confirms that the secondary redistribution resulting from the higher poloidal harmonics reduces the transport, but the toroidal harmonics cause it to increase.

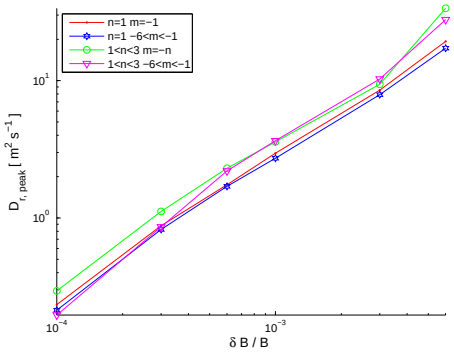

Figure 6.10: Effect of higher mode harmonics on the mode amplitude dependence of the anomalous radial diffusivity caused by the fishbone mode (the error bars have been omitted for clarity, but are of the same order as those in Figure 6.9(a)).

6.5.3 Mode Frequency

The dependence of the fast ion redistribution on the fishbone mode frequency can be determined by varying it and measuring the peak radial diffusivity. In MAST discharges, the fishbones typically start with a mode frequency (in the plasma frame) within the range 17 kHz $< \omega(t = t_0) <$ 25 kHz. By varying the initial frequency, but keeping the mode shape and sweeping rate constant, this effect can be quantified. Figure 6.11(a) shows five different initial frequencies within this range. The figure shows the frequency of the mode as it passes through the peak in the prescribed mode amplitude (which remains constant), shown in the figure.

The peak in the radial diffusivity through the fishbone burst is shown to increase by 34% with increasing initial mode frequency over this range, shown in Figure 6.11(b). The reason for this is best explained by identifying the phase space locations of the resonances during these simulations. The resonant regions sweep through phase space during the fishbone, but are most simply quantified by the point at which the mode amplitude is largest (the saturation time $t = t_{\text{sat}}$). Resonances at the saturation time for the two extreme frequencies are shown in Figure 6.11(c) - the others lie in between. The resonant regions of the distribution function corresponding to a mode frequency of $\omega(t = t_{\text{sat}}) = 18.78$ kHz intersects with steeper

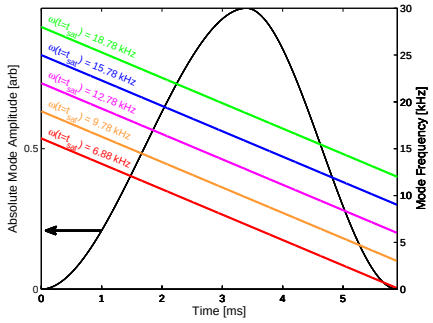

(a) Different mode frequencies during a burst are shown by the different colours, ranging from $\omega(t = t_0)$ =16.1 kHz to $\omega(t = t_0)$ =28 kHz. The mode shape, determined by the value of $t_{\rm sat}$ remains constant.

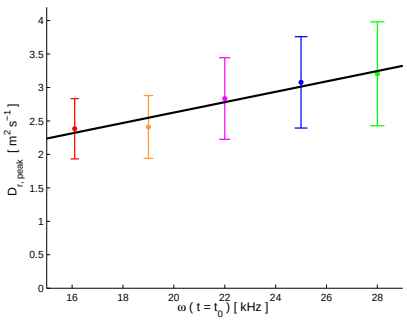

(b) The peak in the radial fast ion diffusivity increases as the mode frequency is increased.

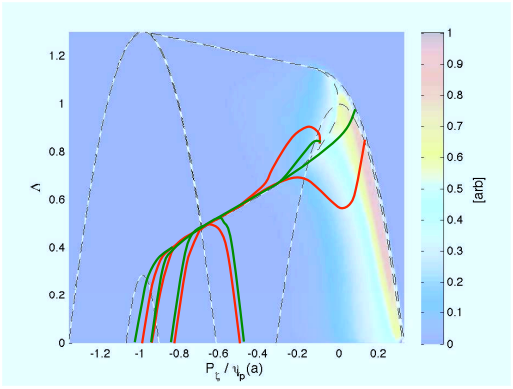

(c) The resonant region at $t = t_{\rm sat}$ varies between the lines shown by the two extreme cases here.

Figure 6.11: Effect of varying the mode frequency of the fishbone.

gradients in the fast ion distribution function, driving the mode harder than the resonant regions at $\omega(t = t_{\rm sat}) = 6.68$ kHz.

6.5.4 Saturation Time

A second parameter that effects the fast ion redistribution is the shape of the fishbone. This is quantified by where the saturation time lies within the burst. The shape of fishbones observed in MAST shots varies greatly, so a range of 1.0 ms $< t_{\mathrm{sat}} <$ 4.0 ms is studied, shown in Figure 6.12(a). The effect of varying this (shown in Figure 6.12(b)) is less pronounced, with only a 12% change in the diffusivity. There is an inflection in the line this time, indicating that there is a defined maxima in the diffusivity for a certain mode shape with a saturation time of $t_{\mathrm{sat}} =$ 2.1 ms. The regions of phase space resonant with the mode at its saturation time are shown in Figure 6.12(c). The mode causes the most significant redistribution when the frequency at the saturation time lies between the green and the red lines.

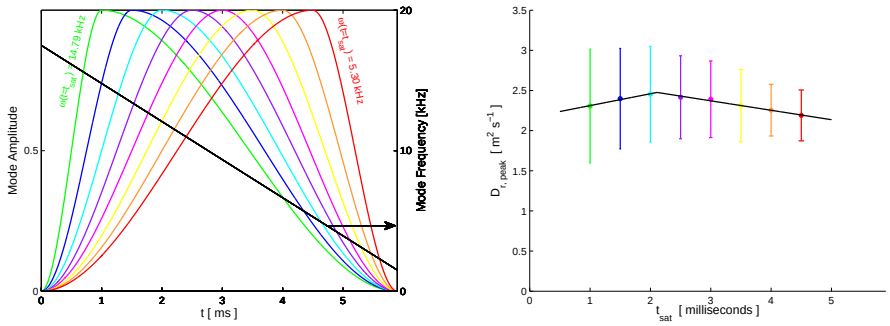

(a) Variation of t_{sat} through 5.9 ms of fishbone burst.

(b) Effect of varying shape of fishbone mode on diffusivity.

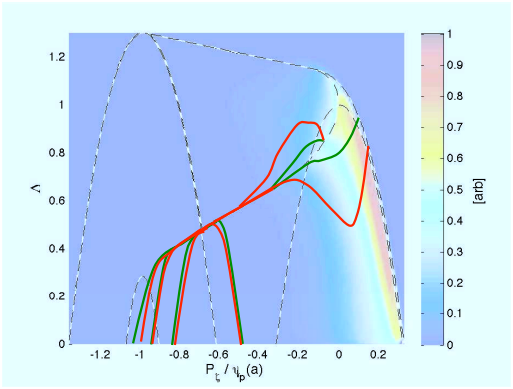

(c) Resonant regions of phase space at two extremes of saturation time.

Figure 6.12: Effect of varying saturation time on the fast ion redistribution.

6.5.5 Sweeping Rate

The sweeping rate has been varied in order to see how this effects the fast ion redistribution due to the fishbone. Figure 6.13(a) shows the difference sweeping rates that were applied. Either the starting frequency of the ending frequency of the mode will have to vary; in order to best contrast with when the initial mode frequency was varied (Figure 6.11), the mode frequency at the saturation time has been kept constant. The chirping modes are shown to always sweep through the same frequency at $t = t_{\text{sat}}$.

The effect this has on the diffusivity is shown in Figure 6.13(b). The diffusivity is more strongly dependent upon the sweeping rate than the initial mode frequency, as the line is steeper. Since the chirping modes all pass through the same point at the saturation time, Figure 6.13 shows only one set of resonance lines is at $\omega(t = t_{\text{sat}}) = 9.42\text{kHz}$. The larger the sweeping rate, the greater the size of the resonant region that is swept out.

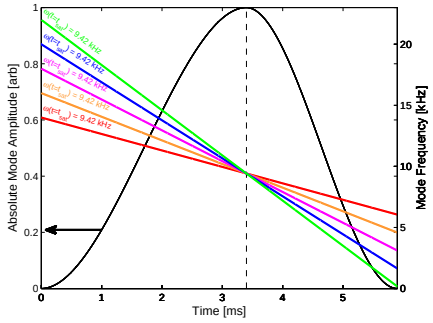

(a) Variation of mode sweeping rate through 5.9 ms of fishbone burst.

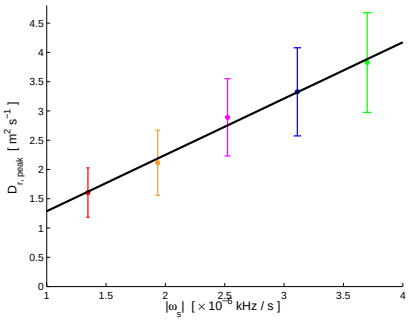

(b) Effect of sweeping rate of fishbone mode on diffusivity..

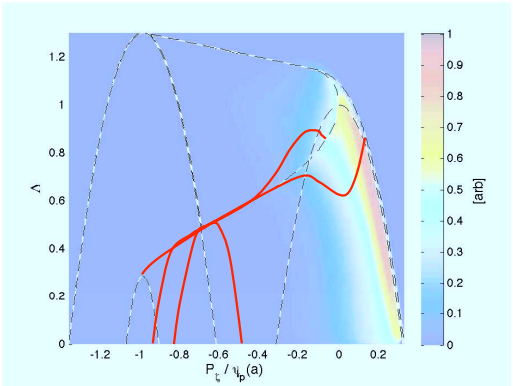

(c) The resonance regions for all sweeping rates at $t = t_{\text{sat}}$ co-align.

Figure 6.13: Effect of varying the sweeping rate on the fast ion redistribution.

6.6 Summary

This section has shown how the fast ions are redistributed away from the core of the plasma due to the fishbone mode. The redistribution of the fast ions has been shown in two dimensions as a projection onto the poloidal cross section, as well as in the CoM phase space that is used to represent the unperturbed fast ion distribution function. It has also been shown as a function of radius, which is quantified by way of anomalous radial transport coefficients. The fishbones studied here provide a diffusive transport at the level that is required to model such phenomena using transport codes such as TRANSP. The parameters of the fishbones that cause the largest levels of redistribution have been identified, and the level of radial transport has been shown to scale linearly with the amplitude of the fishbone mode. The next chapter describes how synthetic diagnostics may be used to compare the fast ion redistribution directly to that observed in the experiments.

Chapter 7

Modelling Experimental Observations

A 'synthetic diagnostic' can be built into a computational model in order to simulate what a real experimental diagnostic would measure. It can then be used to confirm that modelling is providing results that are consistent with experiment, as well as allowing extrapolative measurements to be made in the model that are not possible in the experiment. I have built two synthetic diagnostics into the HAGIS code in order to make direct quantitative comparisons between the results of the modelling that has been performed and the MAST experimental data. The first is the total neutron yield from the plasma, to simulate the integrated value measured by the fission chamber and the second is the radial neutron emissivity profile, which can be determined experimentally by the NC. The synthetic diagnostics have been used to interpret the results from the HAGIS simulations and provide direct comparisons with the experimental tokamak diagnostics.

7.1 Neutron Rate

The neutron rate integrated over the whole plasma is measured by a fission chamber. This diagnostic provides time resolved information on the neutrons emitted from the plasma [58], providing a direct measure of the total fusion yield. The neutron rate $\mathcal{R}$ from two Maxwellian particle species of density n_1 and n_2 is given by [16]

$$\mathcal{R}_{12} = n_1 n_2 \langle \sigma v \rangle \,, \tag{7.1}$$

where $\langle \sigma v \rangle$ is known as the reactivity, a velocity-averaged product of the reaction cross section σ and velocity v for a Maxwellian plasma, and is a function of the

temperature $\langle \sigma v \rangle (T)$. For a single-species plasma, the neutron rate is

$$\mathcal{R}_{11} = \frac{1}{2} n_1^2 \langle \sigma v \rangle \tag{7.2}$$

where the factor of 1/2 accounts for the double-counting of the fusion reactions. The reactivity depends upon the species involved, and as shown in Figure 1.2(b) is largest for D-T fusion at the lowest (most readily attainable) temperatures, which is why this is the favoured approach for fusion. MAST does not contain any tritium, so it is the black D-D line in this figure that is relevant.

By considering the distribution function of each species f_1 and f_2 the total neutron rate per unit volume of the plasma can be written [16]

$$\mathcal{R}_{12} = \int \int \sigma(v') \; v' \; f_1(v_1) \; f_2(v_2) \; \mathrm{d}^3 v_1 \; \mathrm{d}^3 v_2, \tag{7.3}$$

where $v' = v_1 - v_2$ is the 'collision velocity' (or 'centre of mass velocity') of the two particles, and from nuclear physics σ is the reaction cross section, which is itself strongly dependent upon the collision velocity. The HAGIS code used in this thesis simulates only the fast ions in the plasma. To determine a neutron flux from the plasma, it is necessary to consider the thermal (bulk) ions as a second population. These two distinct species then provide the two densities for the neutron rate calculation. The two populations contribute to three terms in the neutron rate. The first term comes from reactions between the fast ions and the bulk thermal ion population, referred to as 'beam-thermal' fusion which is dominant and makes up around 90% [160] of the contribution. The majority of the remaining contribution comes from reactions between the fast ion population with itself, 'beam-beam' fusion. The contribution from the bulk plasma with itself, 'thermal-thermal', is negligible in MAST [161].

The neutron yield in the simulations is determined by integrating over the whole plasma, here considering only the beam-thermal contribution. From the assumption that $v_f \gg v_t$, the collision velocity can be simplified to $v' = v_f$ by considering the thermal ion to be stationary (referred to as a 'cold' thermal ion population). This means that the reaction cross section is a product only of the fast ion velocity. As explained previously, the fast ion density $n_\mathrm{f} = \int f \; \mathrm{d}^3 v$ cannot be found in HAGIS (see Section 6.1). For this reason, the $D-D$ neutron emissivity integrated over the whole plasma volume V is calculated,

$$\mathcal{S}_\mathrm{DD} = \int \mathcal{R}_\mathrm{DD} \; \mathrm{d}^3 x \; . \tag{7.4}$$

For a given population, this can be written in terms of the markers used in HAGIS as

$$\mathcal{S}_{\mathrm{DD}} = \int \sum_{j=1}^{N_j} n_{\mathrm{f},j}\ n_{\mathrm{t},j}\ \sigma(v_{\mathrm{f},j})\ v_{\mathrm{f},j}\ \mathrm{d}^3x, \tag{7.5}$$

where $n_{\mathrm{f},j}$ is the fast ion density represented by the j^{th} simulation marker, and $n_{\mathrm{t},j}$ is the thermal ion density at this point, evaluated using the data in Figure 5.9(a). The reaction cross section is evaluated from the velocity of the j^{th} simulation marker $v_{\mathrm{f},j}$ using the parameters determined by the improved R-matrix theory approach of Bosch and Hale [14]. Equation 7.5 can be rewritten as

$$\mathcal{S}_{\mathrm{DD}} = \sum_{j=1}^{N_j} N_{\mathrm{f},j}\ n_{\mathrm{t},j}\ \sigma(v_{\mathrm{f},j})\ v_{\mathrm{f},j}, \tag{7.6}$$

where $N_{\mathrm{f},j} = \int n_{\mathrm{f},j}\ \mathrm{d}^3x = \int f_{\mathrm{f},j}\ \mathrm{d}\Gamma^{(p)}$ is the total number of particles represented by the j^{th} simulation marker, which can be determined in the code.

The simulation is performed in the plasma frame (see Section 5.1), which is rotating at frequency $\omega_r(\psi_p)$. To calculate the neutron rate in the lab frame, a correction is made to the toroidal component of the particle velocity,

$$v_{\zeta,\mathrm{lab}} = v_{\zeta,\mathrm{plasma}} - v_r\ . \tag{7.7}$$

The radial rotation frequency profile of $\omega_r(\psi_p)$ is shown in Figure 5.9.

7.2 Core Neutron Rate Drop

The density in the core of the plasma has been shown to drop in the HAGIS simulations, since the non-conservation of $\mathcal{E}$ and P_ζ result in an outward radial redistribution of the fast ions. The drop in density core results in a drop in neutron emission. This has been modelled using Equation 7.6. Approximating the plasma core to be within ($s < 0.3$), the core neutron emission is calculated using

$$\mathcal{S}_{\mathrm{DD}}(s < 0.3) = \int_{s=0}^{0.3} \mathcal{R}_{\mathrm{DD}}\ \mathrm{d}^3x\ .$$

For an $n = 1$, $m = -1$ fishbone mode of amplitude $\delta B/B = 6 \times 10^{-3}$ the core neutron emission as a function of time throughout the burst is shown in Figure 7.1 to drop by 15.2%. The fast ions that are redistributed away from the hot core move into the outer region, where the thermal ion density and temperature are lower, so

they will contribute less to the total neutron emission from the plasma.

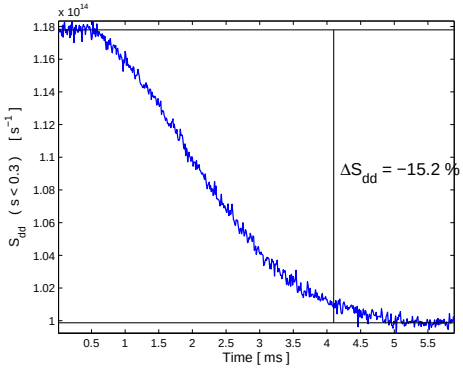

Figure 7.1: Drop in core neutron emission during a fishbone burst of amplitude $\delta B/B = 6 \times 10^{-3}$.

7.3 Neutron Camera

The recently installed NC is a diagnostic capable of producing time-resolved information of the neutrons emitted from the plasma, integrated along the Line of Sight (LoS) of the camera view. This allows for measurements of the redistribution of the fast ions to be performed [59, 60]. It observes a collimated view of the plasma, simultaneously measuring two chords with tangency radii of $0\text{m} < R_{\text{NC}} < 1.22\text{m}$. The radial direction is measured by means of an Impact Parameter (IP), which is the radius at which the chord makes a tangent to the centre column, as shown in the schematic of the diagnostic in Figure 7.2. The camera can be rotated on rails between shots, allowing radial profiles to be built up. Two vertical angles are measured, one through the plasma mid-plane and one diagonally. The diagnostic is calibrated using the ^{235}U fission chamber. Previous work using the TRANSP code has found that an anomalous radial diffusivity of $2\text{m}^2\text{s}^{-1} < D_r < 3\text{m}^2\text{s}^{-1}$ is required in order to match the change in the radial emissivity measured by the NC [162]. From the results shown in Section 6.5.1, this level of anomalous diffusivity (excluding any convective transport, as in the TRANSP runs) corresponds to a mode of peak fishbone mode amplitude $\delta B/B \sim 5 \times 10^{-3}$, which has a peak radial diffusivity of $D_{r,\text{peak}} \sim 15\text{m}^2\text{s}^{-1}$ but a sustained temporal diffusivity for several milliseconds over a broad radial region of $D_r \sim 2$ to $3\text{m}^2\text{s}^{-1}$. Note here that only the $n = 1$, $m = -1$ mode is considered; the mode amplitude required would be smaller with the inclusion of the higher toroidal mode harmonics.

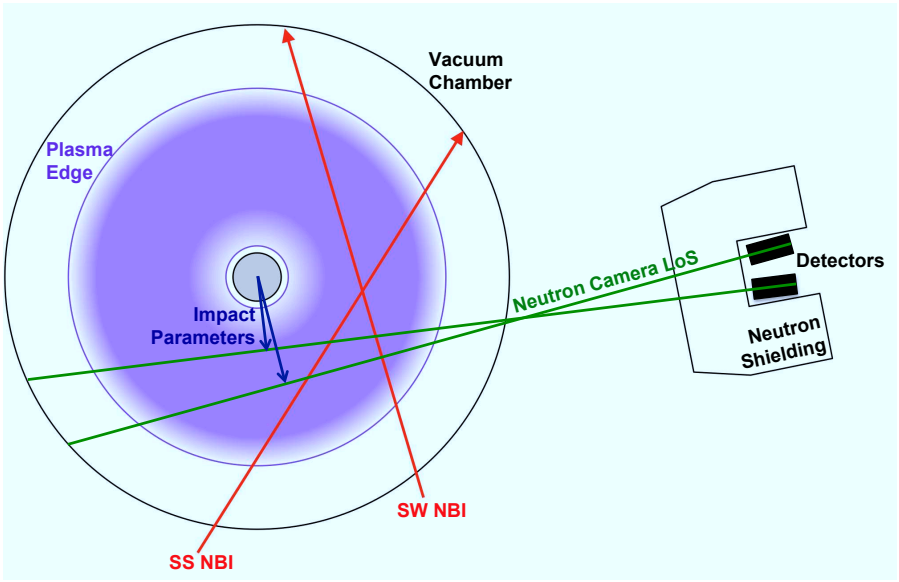

Figure 7.2: Top-down view of the MAST vessel on the equatorial mid-plane. The NC measures neutron emission along two LoS simultaneously, which are defined by their IP. The NC can be moved along rails between shots in order to determine radial profiles. Figure adapted from [60].

7.3.1 Experimental Results

The NC views the plasma from only two radial IP locations during a shot. This means that in order to build up a radial neutron emissivity profile from the horizontal view multiple shots are required, rotating the NC between each one in order to detect from a different location. Due to this, multiple fishbone modes were identified in equivalent plasma discharges in which the camera location was different. These modes all occur between 0.210s and 0.245s (such that the plasma equilibrium is consistent) in shots `#26789`, `#27920` and `#27927`. The magnetic instability data for these shots from the OMV coils is shown in Figure 7.3. A 'composite' fishbone mode is used to make up the radial emissivity profile, comprising of the fishbones within the 6ms windows shown in red in this figure. Neutron emissivities before and after each fishbone event is measured, defined as being 3ms before and 3ms after the peak in the magnetic signal burst (t_{sat}). For the two lines of sight, the pre and post fishbone emissivity is averaged across the two modes chosen in each shot. The subsequent radial profile made up from the composite fishbone modes is plotted in Figure 7.4 against the IP. It shows a core neutron emissivity drop of 19% in the equatorial line of sight. Since the NC is primarily used to diagnose the distribution of fast ions in the core, no data is taken for IP < 0.75m.

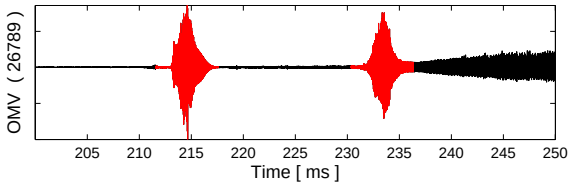

(a) Shot #26789.

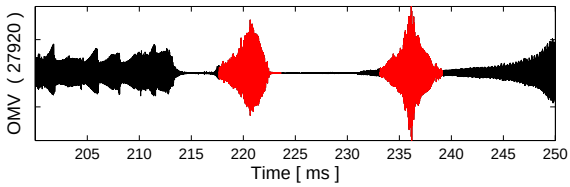

(b) Shot #27920.

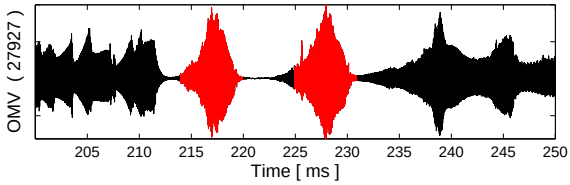

(c) Shot #27927.

Figure 7.3: Magnetic coil signal from the OMV 210 showing equivalent fishbone modes from three different shots that are used to build up a radial profile of neutron emissivity using the NC. The six modes used to make up the radial profile are shown in red.

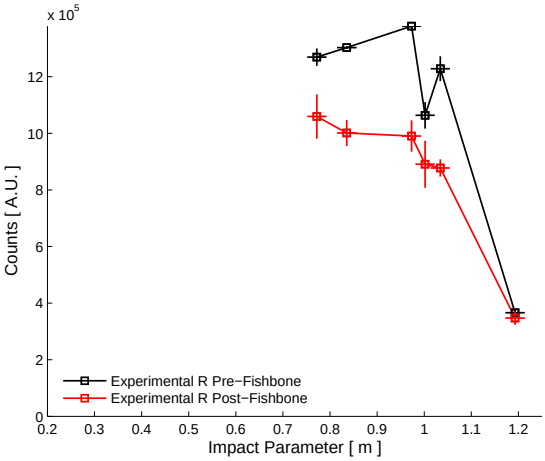

Figure 7.4: Composite radial profile built up using multiple shots to show the pre- and post-fishbone experimental neutron emissivity.

7.3.2 Simulation Results

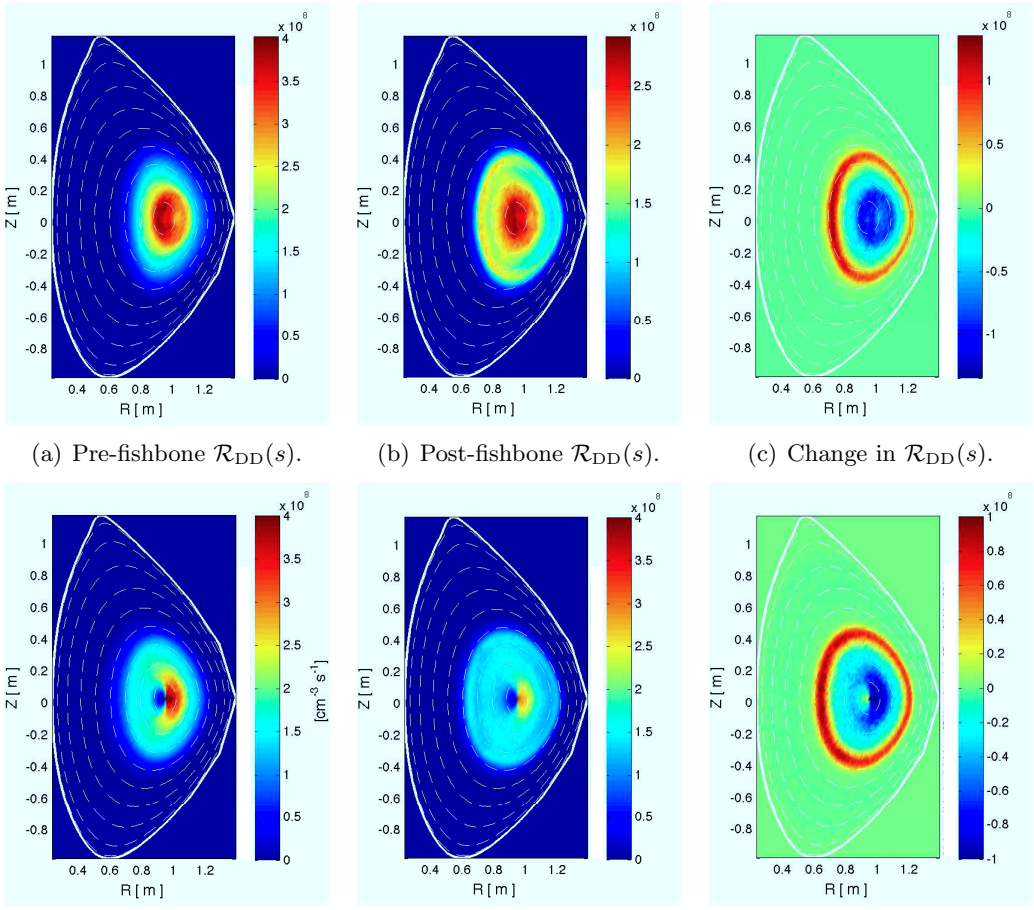

(a) Pre-fishbone $\mathcal{R}_{\mathrm{DD}}(s)$. (b) Post-fishbone $\mathcal{R}_{\mathrm{DD}}(s)$. (c) Change in $\mathcal{R}_{\mathrm{DD}}(s)$.

(d) Pre-fishbone $\mathcal{R}_{\mathrm{DD}}(\langle s \rangle)$. (e) Post-fishbone $\mathcal{R}_{\mathrm{DD}}(\langle s \rangle)$. (f) Change in $\mathcal{R}_{\mathrm{DD}}(\langle s \rangle)$.

Figure 7.5: 2D poloidal cross sections of neutron emission in MAST simulations created using HAGIS for a mode amplitude $\delta B/B = 5 \times 10^{-3}$.

To create a NC synthetic diagnostic, a 2D poloidal cross section of the neutron emissivity is required. From this, a LoS equivalent to that seen by the NC can be calculated using the LINE2 code [163]. From multiple LoS it is possible to build up radial neutron emissivity profiles comparable to the experimental ones. This has been done previously with TRANSP simulation data, where a constant anomalous diffusivity is prescribed in order to model a time period containing fishbones [162, 164]. The 2D poloidal cross section of the neutron emissivity has been calculated in HAGIS by binning out $\mathcal{S}_{\mathrm{DD}}$ found using Equation 7.6 in the poloidal plane using

$$\mathcal{R}_{\mathrm{DD}}(R, Z) = \frac{\mathcal{S}_{\mathrm{DD}}(R, Z)}{\Delta V(R, Z)} \,, \tag{7.8}$$

which is equivalent to the way that the 2D fast particle distribution function was found in Section 6.3. This provides the neutron emissivity integrated toroidally.

As shown in Figure 7.3, the composite fishbones that make up the radial profile are not absolutely identical. Each has a similar mode amplitude, and the equilibrium conditions are considered similar enough to be equivalent. This leads to the requirement of a 'generic' fishbone mode. The saturation time and initial mode frequency vary slightly, so t_{sat} =2.5ms and $\omega(t = t_0)$ =22kHz were chosen. A 6ms time period was simulated, equivalent to the $t_{\text{sat}} = \pm 3$ms considered in the experimental fishbones (the red periods in Figure 7.3). Two peak relative mode amplitudes were chosen (using the results from Chapter 6 as a guide as to what the experimental mode amplitude is) of $\delta B/B = 1 \times 10^{-3}$ and $\delta B/B = 5 \times 10^{-3}$. The specification for this fishbone is shown in Table 7.1.

Parameter	**Value**
Fishbone Duration	$\Delta t = 6.0$ms
Saturation Time	$t_{\text{sat}} = 2.5$ms
Initial Frequency	$\omega(t = t_0) = 22$kHz
Sweeping Rate	ω_s = -2.71$\times 10^6$kHz/s
Peak Mode Amplitude	$\frac{\delta B}{B}(t = t_{\text{sat}}) = 1 \times 10^{-3}$ & 5×10^{-3}

Table 7.1: Specification of a 'generic' MAST fishbone composed from the modes shown in Figure 7.3.

For each of the two mode amplitudes, the 2D neutron emissivity profile was found. An example of this is shown in Figure 7.5. The initial emissivity from just the input LOCUST-GPU distribution function is shown in Figure 7.5(a), and the post-fishbone emissivity from the redistributed fast ions is shown in Figure 7.5(b) for a mode of amplitude $\delta B/B = 5 \times 10^{-3}$. The difference to the emissivity caused by the mode is shown in Figure 7.5(c). It can be seen that the redistribution shown for a similar mode in Figure 6.5 is responsible for the drop in core neutron emissivity. These figures show the emissivity that is binned out according to the instantaneous position of the simulation marker $\mathcal{R}_{\text{DD}}(s)$, labelled by its radius s. For each mode amplitude, the neutron emissivity has additionally been binned out as a function of the orbit-averaged radius of the marker, $\mathcal{R}_{\text{DD}}(\langle s \rangle)$. The difference is shown between the top row and bottom row in Figure 7.5. The presence of the trapped particles on the LFS of the plasma is shown more clearly in the plot of $\mathcal{R}_{\text{DD}}(\langle s \rangle)$, and due to the high trapped-particle fraction in MAST this makes up a more accurate representation of the 2D slice of neutron emissivity. The values of $\langle s \rangle = \left(\langle \psi_p \rangle / \psi_p(a)\right)^{1/2}$

are calculated in HAGIS according to the particle classification,

$$\langle \psi_p \rangle = \begin{cases} \sqrt{2\left(\mathcal{E}-\mu\right)} - P_\zeta^{(0)}, & \text{for } \mathcal{E} > \mu \quad \text{(Co-passing)} \\ - \quad P_\zeta^{(0)}, & \text{for } \mathcal{E} < \mu \quad \text{(Trapped)} \\ - \quad \sqrt{2\left(\mathcal{E}-\mu\right)} - P_\zeta^{(0)}, & \text{for } \mathcal{E} > \mu \quad \text{(Counter-passing)} \end{cases} \tag{7.9}$$

Using the LINE2 code radial profiles are built up, as shown in Figure 7.6 for both

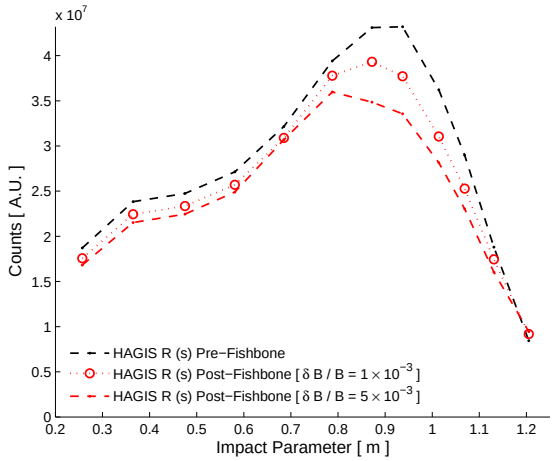

(a) HAGIS neutron emissivity binned out at $\langle s \rangle$.

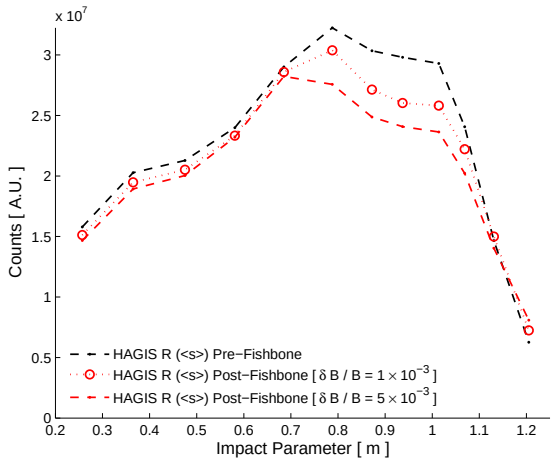

(b) HAGIS neutron emissivity binned out at s.

Figure 7.6: Comparison of the pre- and post- fishbone radial neutron emissivities from the HAGIS simulations.

$\mathcal{R}_{\mathrm{DD}}(s)$ and $\mathcal{R}_{\mathrm{DD}}(\langle s \rangle)$. By comparing this to the experimentally observed drop to the neutron emission (Figure 7.4), it is apparent that the $\mathcal{R}_{\mathrm{DD}}(\langle s \rangle)$ provides a closer fit to the experimental observations. This means that the orbit-averaged fast

ion location provides a better estimate for this modelling (the same was found for TRANSP simulations in [164]). The drop in $\mathcal{R}_{\mathrm{DD}}(\langle s \rangle)$ from the HAGIS simulations

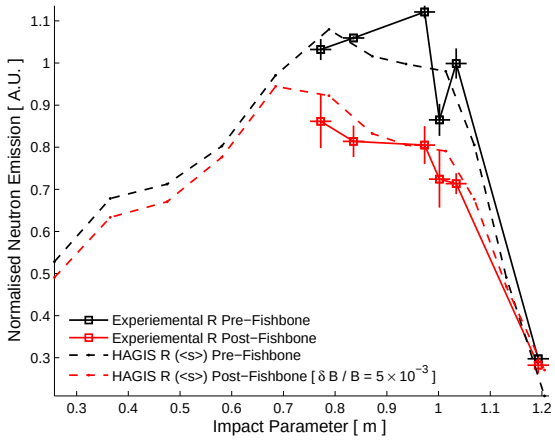

Figure 7.7: Comparison of the drop in the radial neutron emission due to a generic fishbone of mode amplitude 5×10^{-3}. The parameters of the generic fishbone used are given in Table 7.1.

with a peak mode amplitude $\delta B/B = 5 \times 10^{-3}$ is plotted along side the experimentally observed drop in Figure 7.7. This figure shows a comparison between the changes in the radial neutron emissivity, normalised to the initial emission in the core of the plasma. The change in neutron emission in the simulation shows a good agreement with the experimental data from the NC.

7.4 Summary

This chapter has shown that the integrated beam-thermal neutron rate from a MAST plasma can be determined in HAGIS and a drop in the core emission due to the fishbone mode is shown. An experimental radial profile of neutron emission before and after a fishbone mode has been built up from six fishbones which occurred during three equivalent MAST shots using data from the horizontal view of the NC. The drop observed has been shown to be consistent with a generic fishbone applied to the HAGIS model of peak relative mode amplitude $\delta B/B \sim 5 \times 10^{-3}$. This synthetic diagnostic data provides confirmation that the simulations supply a good match with experiment for the change in the fast ion distribution function.

Chapter 8

Summary and Conclusions

8.1 Summary

Since they were first observed during beam-heated plasma discharges in the 1980s [43], low-frequency fast ion driven internal kink mode instabilities, referred to as fishbone modes, have proven to be deleterious to tokamak heating mechanisms. Observed on a wide range of present day devices [44–49], modes such as fishbones are understood to be responsible for the larger than predicted levels of anomalous fast ion transport and are considered to be a genuine challenge faced for the operation of future devices such as ITER [50, 51]. Research into these instabilities provides us with a better understanding of them and will allow us to minimise their detrimental effects in order to retain the EP population long enough to heat the bulk ions and achieve a self-sustained thermonuclear burning plasma.

This thesis has described the dedicated experiments that have been performed in order to better understand fishbones in MAST. The work presented here provides a theoretical interpretation and explanation of the modes, which have been subject to recent experimental research on MAST using the FIDA [57, 165] and NC [60] diagnostics. The fishbone modes have been observed and quantified by the experimental diagnostics. From these observations, an accurate model has been constructed that is prescribed to a numerical code in order to determine the resulting redistribution of the EP population. The drift-kinetic δf code HAGIS was chosen as it is the most appropriate tool to model such plasma phenomena, because it allows a perturbation to be prescribed that matches what is observed in the experiment and will subsequently evolve the fast ion population in order to see how it redistributes the fast ions.

I have used for the first time a fast ion distribution function from the recently-

developed LOCUST-GPU code [130] for this modelling which provides the guiding centre approximation of a fully six dimensional distribution function, rather than one made up of the product of one dimensional functions in radius and energy, offering a new level of quantitative accuracy. The most appropriate way to describe the fast ion distribution is through the unperturbed CoM of the fast ions. Within the CoM phase space regions have been identified that are resonant with the fishbone mode. The resonances are time dependent, and have been shown to sweep out through the densest regions of the distribution function. Guiding centre orbits of the fast ions that exist along these resonances have been plotted and provide a clear understanding of which particles in the plasma are resonant the fishbone mode. The link between LOCUST-GPU and HAGIS has been validated in terms of particle orbits, and benchmarked against an equivalent analytic MAST fast ion distribution function.

By applying the experimentally observed fishbone perturbation within the model, a flux of fast ions was observed away from the hot plasma core. The redistribution has been shown to occur around the radial location of the peak in the internal kink mode that is used to model the fishbone. It has been quantified by means of anomalous transport coefficients, and when considering diffusive transport this was measured to be $D_{r,\mathrm{peak}} \sim 3\mathrm{m}^2\mathrm{s}^{-1}$ for a realistic relative mode amplitude of $\delta B/B = 1 \times 10^{-3}$ for the dominant $n = 1$, $m = -1$ internal kink mode. To achieve this level of diffusivity across a broad radius for a sustained time, a mode amplitude $\delta B/B \sim 5 \times 10^{-3}$ is required. By introducing additional poloidal mode harmonics the level of fast ion redistribution is shown to decrease, which is interpreted as being due to the fact that its peak lies in the region where the fast ions have been redistributed to by the $m = -1$ harmonic. The opposite is true if one interprets the higher toroidal mode harmonics observed in the spectrograph during the burst as individual mode eigenfunctions, the temporal evolution of the relative amplitudes of which I have identified. I have shown for the first time the effect of the inclusion of these higher toroidal mode harmonics, using a technique similar to that in [117]. Running the simulation with all of the modes results in an increase of only ~ 20 % from the $n = 1$, $m = -1$ mode, confirming that to be the dominant cause of the fast ion redistribution. By varying the specification of the fishbone within the experimentally observed parameters, the modes that result in the most significant redistribution have been identified and interpreted using the aforementioned resonance plots.

Fast ion redistribution away from the hot core of the plasma results in a change in the experimental radial neutron emission measured by the NC, presented

for the first time as a result of an individual fishbone mode. The modelling performed incorporates the NC into HAGIS for direct comparison via a synthetic diagnostic. For a generic fishbone mode the change to the neutron emissivity profile has been shown to reproduce the experimental drop when a mode of amplitude $\delta B/B = 5 \times 10^{-3}$ is prescribed. This is within the range of the experimentally observed mode amplitudes in MAST.

8.2 Conclusions

The principle conclusion of this thesis is that fishbone modes observed in MAST are responsible for redistributing the fast ions away from the core of the plasma and into regions where they are less effective at heating it. This has been quantified by means of anomalous radial transport coefficients. We have found the values to be in agreement with those required for modelling performed using global tokamak transport codes that accurately recreate experimental observations [158, 164]. This provides evidence at a more fundamental level than in [158] (in which a level of anomalous transport is prescribed to an *ad-hoc* model) that it is the fishbone modes that offer a viable driving mechanism of the high level of anomalous transport of the EP population that is observed by the experimental diagnostics in MAST discharges, and must be suitably controlled in order to achieve burning plasmas in future devices such as ITER.

The research presented here brings a new level of accuracy to fast ion modelling, by incorporating a realistic EP population from the LOCUST-GPU code which can now be read into HAGIS. This offers an enhancement compared to previous HAGIS modelling of fishbones that has been performed on JET [166, 167] and during off-axis NBI in MAST [159, 168], and can be readily employed for looking at other instabilities using the code such as research that has previously been done, for example on fast ion losses [169] and transport due to AEs [170]. Linking these codes provides an excellent tool for future modelling of tokamak plasmas, and forms a sound basis to make accurate theoretical predictions of the MHD behaviour in them.

The regions of phase space that are resonant with the modes have been identified, which has previously been carried out for TAE modes [169, 170] but not for fishbones in the CoM phase space. These figures have been used in order to understand what specifications of fishbone mode are most deleterious to the fast ion population. It has also been used to make predictions for the MAST-U device that is under construction [155, 156], suggesting that if the fishbones are resonant with

the same regions of phase space as they are in MAST the fast ions resulting from the new off-axis beam should not be radically redistributed, but will be affected. Implementation of this will be crucial in tailoring the heating mechanisms in order to reduce the drive of MHD instabilities. Identification of particle resonances in this manner also has relevance to potential alternative heating techniques. Direct extraction of heat from waves by the ions (rather than via the electrons) referred to as 'α-channelling' has been proposed [171, 172], and it has been suggested that in STs low-frequency $n = 0$ modes may be able to extract energy associated with poloidal bounces of α-particle near the trapped-passing boundary [110]. This system depends upon the resonant frequency of the required area of the EP population being identified.

This work has provided us with a fundamental understanding of the processes behind the level of anomalous fast ion diffusivity in MAST. In addition to this, the validity of the findings in this thesis are reinforced by data in synthetic diagnostics that have been employed in the simulations to show for the first time the effect of an individual fishbone mode on the radial neutron emission, which is compared to that measured experimentally using the NC. This provides both an improved experimental understanding of an individual fishbone compared to references [60, 158, 165] which all focus on time-averaged transport over multiple fishbones. The research in this thesis has shown the importance of the new NC diagnostic for identifying the EP population present in the plasma, and opens up the data it produces via a visual redistribution of the fast ions observed in the modelling. The core drop in neutron emission determined using the NC that I have presented in this thesis show a comparable level to that observed during other MHD activity, for example TAE avalanches in NSTX [86], where the total neutron rate drops experimentally by 23%.

8.3 Further Work

To further develop the research that has been carried out into fishbones in this thesis, the effect of plasma rotation could be more consistently included into this work. This would be done using an equilibrium code such as the Finite Element Solver for Stationary Equilibria (FINESSE) [173, 174] which incorporates the rotation via a radial electric potential, in addition to a mode eigenfunction calculated for the rotating plasma using the PHOENIX code [174, 175].

The link between the HAGIS and LOCUST-GPU codes that has been implemented is bidirectional, allowing collaborative fast ion modelling to be per-

formed with the two codes whereby the accurate distribution function is identified in LOCUST-GPU and the MHD is evolved temporally in HAGIS; multiple runs of each of the codes would provide modelling for longer timescale behaviour of the EP population. By passing the redistributed fast ion distribution function back into LOCUST-GPU, further synthetic diagnostic measurements may be taken in the future, for example to allow comparison with the experimental EP population via the new MAST FIDA diagnostic [57, 165]. The effect of fishbones on other devices could be studied in detail in the way that has been performed in this thesis. The treatment of the modes is general, so by identifying the appropriate equilibrium and mode structure the analysis could be performed on chirping instabilities observed on virtually any tokamak. Other modes could be studied in a similar way, for example TAE avalanches which have been the subject of studies in NSTX [86]. Experiments to study these modes are planned on MAST during the imminent campaign. The combined LOCUST-GPU and HAGIS modelling that has been presented here is an ideal tool to interpret the results from these experiments.

During the low density MAST shot `#27182` Alfvénic chirping modes were observed to be suppressed when the second NBI was switched on some time after the onset of the first NBI. A further experiment is will be performed to recreate this phenomenon, and determine its cause in order to attempt to develop a technique in which these modes are ameliorated. The work that has been performed in this thesis whereby regions of phase space that are resonant with the mode have been identified can be extended to these chirping Alfvénic modes, in an attempt to understand why the change to the fast ion distribution function due to the onset of the second beam removed the instability drive.

The predictive work that has been performed to identify potential fast ion redistribution of the off-axis beam population in MAST-U can be extended by performing the analysis using an accurate MAST-U equilibrium. Assuming that the fishbone modes will remain in the same frequency range in MAST-U, this would provide a clear indication of the scale of the detrimental effects of the modes on the off-axis injected ion population, and make predictions as to its effect on the fuelling and current drive. This is crucial in the development of non-inductive current drive mechanisms [21], a fundamental requirement of future STs such as those proposed as CTFs [176, 177] which are a vital component of long-term fusion research.

Appendix A

Tokamak Devices

Listed in Table A.1 are a range of tokamak devices from around the world, and the relative directions of the plasma current and toroidal magnetic field during normal operation, and the subsequent sign of the q-profile and direction of the $\nabla\mathbf{B}$ drift for the ions.

Machine	NBI	I_p	B_t	Ion ∇B drift	q
MAST	Anti-clockwise	Anticlockwise	Clockwise	Downwards	-ve
JET	Clockwise	Clockwise	Clockwise	Downwards	+ve
ASDEX-U	Anti-clockwise	Anticlockwise	Clockwise	Downwards	-ve
Alcator C-MOD	—	Clockwise	Clockwise	Downwards	+ve
DIII-D	Both	Anticlockwise	Clockwise	Downwards	-ve
Tore Supra	Clockwise	Clockwise	Clockwise	Downwards	+ve
ITER	Clockwise	Clockwise	Clockwise	Downwards	+ve

Table A.1: Relative directions of plasma current and toroidal magnetic field for major tokamaks.

Publications & Conference Proceedings

R.J. Lake, S.D. Pinches, R.J. Akers & E. Verwichte. '*Quantitative Modelling of Fast Ion Behaviour in MAST.*'. Proc. 38th IoP Plasma Physics Group Spring Conference, North Berwick, UK (2011).

S.D. Pinches, R.J. Akers, B.N. Breizman, R.J. Lake, M.K. Lilley & S. Sharapov. '*Fast Ion Driven Instabilities in MAST*'. Proc. 12th IAEA Technical Meeting on Energetic Particles in Magnetic Confinement Systems, Austin, Texas, USA (2011).

R.J. Lake, S.D. Pinches, R.J. Akers & E. Verwichte. '*Instability Driven Fast Ion Transport in MAST*'. FUSENET PhD Event, Garching, Germany (2011).

R.J. Lake, S.D. Pinches, R.J. Akers & E. Verwichte. '*Fast Ion Transport due to Fishbones in MAST*'. Proc. 39th IoP Plasma Physics Group Spring Conference, Oxford, UK (2012).

R.J. Akers, E. Verwichte, T.J. Martin, S.D. Pinches & R.J. Lake. '*GPGPU Monte Carlo Calculation of Gyro-Phase Resolved Fast Ion and n-State Resolved Neutral Deuterium Distributions*'. Proc. 39th EPS Conference on Plasma Physics, Stockholm, Sweden (2012).

R.J. Lake, S.D. Pinches, R.J. Akers & E. Verwichte. '*Advances in Wave-Particle Interaction Modelling of Fishbones in MAST*'. Proc. IOP Computational Plasma Physics Conference, Brighton, UK (2012).

R.J. Lake, S.D. Pinches, R.J. Akers & E. Verwichte. '*Fast Ion Transport due to Fishbones in MAST*'. Proc. 54th APS Division of Plasma Physics Annual Conference, Providence RI, USA (2012)

S.D. Pinches, R.J. Akers, B.N. Breizman, M. Cecconello, R.J. Lake, M.K. Lilley, C. Michael, S. Sangaroon, S.E. Sharapov, M. Turnyanskiy, I. Wodniak & the MAST

Team. '*Development of a Predictive Capability for Fast Ion Behaviour in MAST*'. Proc. 24th IAEA Fusion Energy Conference, San Diego, USA (2012).

H. Meyer, et. al.. '*Overview of Physics Results from MAST towards ITER/DEMO and the Upgrade*'. Proc. 24th IAEA Fusion Energy Conference, San Diego, USA (2012).

O. Jones, C.A. Michael, K.G. McClements, N.J. Conway, B. Crowley, R.J. Akers, R.J. Lake & S.D. Pinches. '*Fast-Ion Deuterium Alpha Observations of the Effects of Fishbones in the Mega-Amp Spherical Tokamak.*'. Proc. 40th IoP Plasma Physics Group Spring Conference, York, UK (2013).

M. Turnyanskiy, C.D. Challis, R.J. Akers, M. Cecconello, D.L. Keeling, A. Kirk, R.J. Lake, S.D. Pinches, S. Sangaroon & I. Wodniak. '*Measurement and control of the fast ion redistribution on MAST*'. Nuclear Fusion (2013) [158].

O. Jones, C.A. Michael, K.G. McClements, N.J. Conway, B. Crowley, R.J. Akers, R.J. Lake & S.D. Pinches. '*Fast-Ion Deuterium Alpha observations of the effects of fast-particle-driven MHD in the Mega-Ampere Spherical Tokamak.*'. Proc. 40th EPS Conference on Plasma Physics, Espoo, Finland (2013).

I. Wodniak, M. Cecconello, R.J. Lake, M. Turnyanskiy, S. Sangaroon, G. Ericsson & the MAST Team. '*TRANSP modelling of experimentally measured fast particle redistribution and losses on MAST*'. Proc. 40th EPS Conference on Plasma Physics, Espoo, Finland (2013).

O. Jones, C.A. Michael, K.G. McClements, N.J. Conway, B. Crowley, R.J. Akers, R.J. Lake & S.D. Pinches. '*Fast-Ion Deuterium Alpha spectroscopic observations of the effects of fishbones in the Mega-Amp Spherical Tokamak*'. Plasma Physics and Controlled Fusion (2013) - Submitted.

Glossary

Alcator C-MOD A MODification to the third of the Alcator (Alto Campo Toro, High Field Torus) series of tokamaks (1991-present). 142

CASTOR-K A hybrid MHD-gyrokinetic model is developed for the stability analysis of global Alfvén waves in the presence of energetic ions [143]. 81

EFIT++ An equilibrium reconstruction code that has been shown to accurately recreate tokamak equilibrium across a range of devices [148]. 54, 85–87

HELENA A code that solves the Grad-Shafranov equation to determine a tokamak equilibrium [149]. 85

ITER The 'next step' tokamak reactor, in construction in Caderache, France. xi, 8–10, 38, 50, 80, 81, 104, 137, 139, 142

LINE2 A code that determines LoS views of plasma neutron emission from the 2D poloidal cross section emission [163]. 133, 135

MISHKA A linear stability analysis code, used to find radial mode eigenfunctions [151]. 67, 89, 90, 112

NUBEAM A comprehensive computational model for NBI in tokamaks [133]. 76

OFIT A code that uses optical camera data to match the LCFS of the plasma [150]. 86

PHOENIX A spectral MHD code developed from CASTOR that can incorporate both toroidal and poloidal flow [175]. 140

Tore Supra Tokamak with Superconducting Magnetic Coils in Caderache, France. 142

TRANSP A large, comprehensive, time-dependent tokamak transport data analysis code developed at Princeton Plasma Physics Laboratory [131, 132]. 76, 119, 121, 125, 130, 133, 135

Acronyms

AE Alfvén Eigenmode. 42, 44, 52, 54, 139

ASDEX-U Axially Symmetric Divertor EXperiment - Upgrade. 10, 142

BAAE Beta-induced Alfvén Acoustic Eigenmode. 42

CAE Compressional Alfvén Eigenmode. 42, 54

CCFE Culham Centre for Fusion Energy. 9

CoM Constants of Motion. 34, 71, 73–77, 79, 82, 86, 87, 97, 99, 101, 103, 106, 114, 125, 137, 139

CTF Component Test Facility. 9, 141

CXRS Charge eXchange Recombination Spectroscopy. 11, 85

DIII-D Doublet 3^{rd} generation 'D'-shaped Tokamak. 10, 142

DND Double Null Discharge. 56, 86

EM electromagnetic. 6, 14, 34, 35, 39

EP energetic particle. xi, 9–11, 22, 38–40, 42–45, 49, 51, 52, 62, 64, 80, 87, 89, 95–97, 107, 116, 137, 139, 140

EPM energetic particle mode. 10, 22, 38, 39, 45, 49, 52–54

FIDA Fast Ion D_α. 11, 56, 137, 140

FINESSE Finite Element Solver for Stationary Equilibria. 140

FS Frequency Sweeping. 97

GAE Global Alfvén Eigenmode. 42

GCF gravitational confinement fusion. 6

GPGPU General Purpose computing on GPUs. 76

GPU Graphics Processing Unit. 76

HAGIS HAmiltonian GuIding centre System. 64, 66–68, 70, 76, 78–85, 87, 89, 90, 93, 96, 97, 110, 116–118, 121, 127–129, 131, 133–140

HFS High Field Side. 8, 17, 24, 72, 74

ICF inertial confinement fusion. 6

IP Impact Parameter. 130, 131

JET Joint European Torus. 7–10, 38, 139, 142

JT-60 Japanese large Tokamak. 8

JT-60SA JT-60 Super Advanced. 10

KTAE Kinetic TAE. 42

LCFS Last Closed Flux Surface. 50, 86

LFS Low Field Side. 24, 36, 75, 111, 134

LLM long-lived $n = 1$ internal kink mode. 53, 54, 58–60, 89

LOCUST-GPU LOrentz Code for Use in Spherical Tokamaks. 76–83, 86, 87, 96, 111, 119, 134, 137, 139, 140

LoS Line of Sight. 130, 133, 145

MAST Mega Ampere Spherical Tokamak. xi, 7, 9–12, 14, 24, 38, 54, 56, 62–64, 72, 77, 79, 83–87, 95–97, 106–108, 119, 120, 122, 124, 127, 128, 130, 131, 134, 136–142

MAST-U MAST-Updgrade. 7, 12, 107, 108, 139, 141

MCF magnetic confinement fusion. 6, 9

MHD magnetohydrodynamic. 6, 8, 12, 18–22, 31, 38, 46–48, 51–54, 58, 60, 64, 68, 76, 81, 85, 87, 89, 90, 139, 140, 145

MSE Motional Stark Effect. 11, 56, 85

NBI Neutral Beam Injection. xi, 6, 9–11, 53, 54, 56, 58, 62, 87, 104, 107, 139, 141

NC Neutron Camera. 11, 56, 127, 130, 131, 133, 135–138, 140

NIF National Ignition Facility. 6

NSTX National Spherical Tokamak Experiment. 9, 10, 39, 62, 140

OECD Organisation for Economic Co-operation and Development. 1, 2

OMAHA Outboard Mirnov Array for High frequency Acquisition. 12

OMV Outboard Vertical Mirnov. 12, 54, 58, 60, 130, 131

PDX Poloidal Divertor Experiment. 10, 47, 54

RSAE Reversed Shear Alfvén Eigenmode. 42

SAW Shear Alfvén Wave. 39, 40, 52

SND Single Null Discharge. 56

SS South South. 54

ST spherical tokamak. 8–10, 14, 31, 49, 77, 85, 139, 141

START Small Tight Aspect Ratio Tokamak. 8, 10

SW South West. 54

SXR Soft X-Ray. 11, 47

TAE Toroidal Alfvén Eigenmode. 39, 41, 42, 54, 62, 80, 82, 139, 140

TFTR Tokamak Fusion Test Reactor. 7, 10

TS Thomson Scattering. 11, 85

Bibliography

[1] A. S. Eddington, Nature **106**, 211 (1920). 1

[2] F. W. Aston, Philosophical Magazine and Journal of Science **39**, 611 (1920). 1

[3] A. Einstein, Annalen der Physik **18**, 639 (1905). 1

[4] United Nations, Department of Economic and Social Affairs. Population Division., 2012. 1

[5] BP, Statistical Review of World Energy (http://www.bp.com/sectionbodycopy.do?categoryId=7500&contentId=7068481), Technical report, 2011. 2

[6] World Nuclear Association, Supply of Uranium (http://www.world-nuclear.org/info/Nuclear-Fuel-Cycle/Uranium-Resources/Supply-of-Uranium/#.UYpMKWSkeG8), Technical report, 2012. 2

[7] N. Zeng, Y. Ding, J. Pan, H. Wang, and J. Gregg, Science (New York, N.Y.) **319**, 730 (2008). 2

[8] UNDP, United Nations Development Programme: Commodity Dependence and International Commodity Prices, 2010. 2

[9] A. E. Waltar and A. B. Reynolds, *Fast Breeder Reactors*, 1981. 3

[10] World-nuclear.org, Safety of Nuclear Power Reactors. 3

[11] OECD, *Nuclear Energy Agency, OECD: Comparing Nuclear Accident Risks with Those form Other Energy Sources*, Number 6861, 2010. 3

[12] World Energy Council: World Energy Insight 2011, 2011. 3

[13] G. Audi and A. Wapstra, Nuclear Physics A **595**, 409 (1995). 3

[14] H.-S. Bosch and G. Hale, Nuclear Fusion **32**, 611 (1992). 3, 129

[15] J. D. Huba, *NRL Plasma Formulary*, The Office of Naval Research, 2011. 4

[16] J. Wesson et al., *Tokamaks*, Clarendon Press, Oxford, third edition, 2004. 5, 7, 27, 28, 29, 36, 37, 38, 50, 51, 116, 127, 128

[17] J. D. Lawson, Proceedings of the Physical Society. Section B **70**, 6 (1957). 6

[18] E. L. Dewald et al., Plasma Physics and Controlled Fusion **47**, B405 (2005). 6

[19] L. Artsimovich, Nuclear Fusion **12**, 215 (1972). 6

[20] M. G. Haines, Plasma Physics and Controlled Fusion **53**, 093001 (2011). 7

[21] J. G. Cordey, Plasma Physics and Controlled Fusion **26**, 123 (1984). 7, 141

[22] R. Prater et al., Physical Review Letters **34**, 1432 (1975). 8

[23] S. Yoshikawa and T. Stix, Nuclear Fusion **25**, 1275 (1985). 8

[24] M. Pick et al., The new first wall configuration of JET, in *15th IEEE/NPSS Symposium on Fusion Engineering - Supplement*, pages 54–57, IEEE. 8

[25] M. L. Watkins, Physics of Plasmas **3**, 1881 (1996). 8

[26] A. Loarte, Plasma Physics and Controlled Fusion **43**, R183 (2001). 8

[27] S. Lisgo et al., Super-X Advanced Divertor Design for MAST Upgrade, in *36th EPS Conference on Plasma Physics*, volume 33, pages 0–4.046, Sofia, 2009. 8

[28] N. Balshaw, All-the-World's Tokamaks, www.tokamak.info. 8

[29] P. Rebut, R. Bickerton, and B. Keen, Nuclear Fusion **25**, 1011 (1985). 8

[30] M. Keilhacker et al., Nuclear Fusion **39**, 209 (1999). 8

[31] TheJT-60Team, Proc. 11th Int. Conf. on Plasma Physics and Controlled Nuclear Fusion Research, page 11, 1986. 8

[32] H. Kishimoto, S. Ishida, M. Kikuchi, and H. Ninomiya, Nuclear Fusion **45**, 986 (2005). 8

[33] M. Shimada et al., Nuclear Fusion **47**, S1 (2007). 8

[34] Y.-K. Peng and D. Strickler, Nuclear Fusion **26**, 769 (1986). 8

[35] M. Gryaznevich et al., Physical Review Letters **80**, 3972 (1998). 9

[36] H. Wilson et al., Nuclear Fusion **44**, 917 (2004). 9

[37] A. Sykes et al., Nuclear Fusion **41**, 1423 (2001). 9

[38] B. Lloyd et al., Nuclear Fusion **51**, 094013 (2011). 9

[39] M. Ono et al., Nuclear Fusion **40**, 557 (2000). 9

[40] L. Chen, Physics of Plasmas **1**, 1519 (1994). 10

[41] E. D. Fredrickson et al., Physics of Plasmas **10**, 2852 (2003). 10

[42] S. D. Pinches et al., 22nd IAEA Fusion Energy Conference , 1 (2010). 10

[43] K. McGuire et al., Physical Review Letters **50**, 891 (1983). 10, 47, 48, 112, 137

[44] S. J. Zweben et al., Physics of Plasmas **1**, 1469 (1994). 10, 137

[45] W. Heidbrink and G. Sager, Nuclear Fusion **30**, 1015 (1990). 10

[46] M. Nave et al., Nuclear Fusion **31**, 697 (1991). 10

[47] T. Kass et al., Nuclear Fusion **38**, 807 (1998). 10

[48] M. P. Gryaznevich and S. E. Sharapov, Plasma Physics and Controlled Fusion **46**, S15 (2004). 11

[49] E. D. Fredrickson et al., Physics of Plasmas **13**, 056109 (2006). 11, 39, 137

[50] I. P. E. G. o. E. Drive and I. P. B. Editors, Nuclear Fusion **39**, 2471 (1999). 11, 42, 50, 137

[51] Y. Wu, C. Z. Cheng, and R. B. White, Physics of Plasmas **1**, 3369 (1994). 11, 50, 137

[52] JT-60SA Research Unit, JT-60SA Research Plan: Research Objectives and Strategy (Version 3.0), Technical Report December, 2011. 11

[53] W. W. Heidbrink, The Review of scientific instruments **81**, 10D727 (2010). 11

[54] R. Scannell et al., The Review of scientific instruments **79**, 10E730 (2008). 11, 85

[55] M. F. M. De Bock, N. J. Conway, M. J. Walsh, P. G. Carolan, and N. C. Hawkes, The Review of scientific instruments **79**, 10F524 (2008). 11

[56] N. J. Conway, P. G. Carolan, J. McCone, M. J. Walsh, and M. Wisse, Review of Scientific Instruments **77**, 10F131 (2006). 11

[57] C. Michael et al., Plasma Physics and Controlled Fusion **Submitted** (2013). 11, 137, 141

[58] K. Stammers and M. Loughlin, Nuclear Instruments and Methods in Physics Research Section A: Accelerators, Spectrometers, Detectors and Associated Equipment **562**, 521 (2006). 11, 127

[59] M. Cecconello et al., The Review of scientific instruments **81**, 10D315 (2010). 12, 56, 130

[60] M. Cecconello et al., Nuclear Fusion **52**, 094015 (2012). 12, 130, 131, 137, 140

[61] M. J. Hole, L. C. Appel, and R. Martin, The Review of scientific instruments **80**, 123507 (2009). 12

[62] R. O. Dendy, *Plasma Physics: An Introductory Course*, Cambridge University Press, Cambridge, 1996. 13, 15, 19

[63] C. Henning et al., The Mirror Fusion Test Facility Magnet System Final Design Report, Technical report, 1980. 17

[64] F. F. Chen, *Introduction to Plasma Physics and Controlled Fusion. Volume 1: Plasma Physics*, Second edition, 1984. 18

[65] S. D. Pinches, *Nonlinear Interaction of Fast Particles with Alfvén Waves in Tokamaks*, Phd thesis, University of Nottingham, 1996. 22, 23, 40, 41, 64, 66, 67, 68, 81

[66] H. Grad and H. Rubin, Proceedings of the 2nd UN Conf. on the Peaceful Uses of Atomic Energy **31**, 190 (1958). 27

[67] V. Shafranov, Reviews of Plasma Physics **2**, 103 (1966). 27

[68] A. H. Boozer, Physics of Fluids **24**, 1999 (1981). 30

[69] W. D. D'haeseleer, W. N. G. Hitchon, J. D. Callen, and J. L. Shohet, *Flux Coordinates and Magnetic Field Structure*, Springer-Verlag, Heidelberg, Germany, 1991. 30

[70] H. Alfvén, Ark. Mat Astron. Fysik A **27**, 20 (1940). 31

[71] H. Goldstein, C. P. Pool, and J. L. Safko, *Classical Mechanics*, Addison Wesley, 2002. 32

[72] R. G. Littlejohn, Journal of Plasma Physics **29**, 111 (1983). 32

[73] L. N. Hand and J. D. Finch, *Analytical Mechanics*, Cambridge University Press, 2008. 33

[74] S. Pinches et al., Computer Physics Communications **111**, 133 (1998). 34, 35, 64, 68, 81

[75] L. Chen, J. Vaclavik, and G. Hammett, Nuclear Fusion **28**, 389 (1988). 35

[76] P. Helander and D. J. Sigmar, *Collisional Transport in Magnetized Plasmas (Cambridge Monographs on Plasma Physics)*, Cambridge University Press, Cambridge, first edition, 2002. 36, 37

[77] J. W. Conner and H. R. Wilson, Plasma Physics and Controlled Fusion **36**, 719 (1994). 38

[78] Iter Organisation, http://www.iter.org/factsfigures, 2013. 38

[79] J. Connor and J. Taylor, Nuclear Fusion **17**, 1047 (1977). 38

[80] E. D. C. T. Physics) et al., Nuclear Fusion **47**, S18 (2007). 38

[81] W. W. Heidbrink, Physics of Plasmas **15**, 055501 (2008). 39, 40, 41, 43, 45

[82] R. B. White, Physics of Fluids **26**, 2958 (1983). 39, 48

[83] D. J. Sigmar, C. T. Hsu, R. White, and C. Z. Cheng, Physics of Fluids B: Plasma Physics **4**, 1506 (1992). 39

[84] H. L. Berk et al., Physics of Plasmas **3**, 1827 (1996). 39

[85] E. D. Fredrickson et al., Physics of Plasmas **16**, 122505 (2009). 39, 63

[86] E. Fredrickson et al., Nuclear Fusion **53**, 013006 (2013). 39, 140, 141

[87] H. Alfvén, Nature **150**, 405 (1942). 40

[88] J. Tataronis and W. Grossman, Z. Physik **261** (1973). 40

[89] S. E. Sharapov et al., Physics of Plasmas **9**, 2027 (2002). 42

[90] K. Appert, R. Gruber, F. Troyuon, and J. Vaclavik, Plasma Physics **24**, 1147 (1982). 43

[91] A. Fasoli et al., Physical Review Letters **76**, 1067 (1996). 43

[92] N. Gorelenkov, H. Berk, E. Fredrickson, and S. Sharapov, Physics Letters A **370**, 70 (2007). 43

[93] L. Landau, J. Phys. (USSR) **10** (1946). 44

[94] L. Chen and F. Zonca, Nuclear Fusion **47**, S727 (2007). 45, 52

[95] T. S. Taylor, Plasma Physics and Controlled Fusion **39**, B47 (1997). 46

[96] E. Joffrin, Plasma Physics and Controlled Fusion **49**, B629 (2007).

[97] X. Litaudon et al., Plasma Physics and Controlled Fusion **49**, B529 (2007). 46

[98] E. Joffrin et al., Nuclear Fusion **45**, 626 (2005). 46

[99] J. Manickam et al., Physics of Plasmas **1**, 1601 (1994). 46

[100] C. Gormezano, Nuclear Fusion **22**, 985 (1982). 47

[101] M. Rosenbluth, S. Tsai, J. Van Dam, and M. Engquist, Physical Review Letters **51**, 1967 (1983). 47

[102] S. D. Pinches, H. L. Berk, M. P. Gryaznevich, S. E. Sharapov, and J.-E. Contributors, Plasma Physics and Controlled Fusion **46**, S47 (2004). 48

[103] L. Chen, R. White, and M. Rosenbluth, Physical Review Letters **52**, 1122 (1984). 48, 52, 53, 58

[104] R. J. Hastie, P. J. Catto, and J. J. Ramos, Physics of Plasmas **7**, 4561 (2000). 49

[105] H. Berk, B. Breizman, and M. Pekker, Physical Review Letters **76**, 1256 (1996). 49

[106] B. Coppi and F. Porcelli, Physical Review Letters **57**, 2272 (1986). 49, 58

[107] W. Heidbrink et al., Physical Review Letters **57**, 835 (1986). 49

[108] R. Betti and J. Freidberg, Physical Review Letters **70**, 3428 (1993). 49

[109] F. Zonca et al., Nuclear Fusion **47**, 1588 (2007). 49

[110] B. N. Breizman and S. E. Sharapov, Plasma Physics and Controlled Fusion **53**, 054001 (2011). 49, 58, 60, 85, 104, 140

[111] D. A. Gates et al., Physics of Plasmas **5**, 1775 (1998). 50

[112] Y. Kolesnichenko, V. Lutsenko, and V. Marchenko, Physical Review Letters **82**, 3260 (1999). 50

[113] Y. Kolesnichenko, V. Lutsenko, and V. Marchenko, Nuclear Fusion **40**, 1731 (2000). 50

[114] M. Bussac, R. Pellat, D. Edery, and J. Soule, Physical Review Letters **35**, 1638 (1975). 51

[115] K. Miyamoto, *Plasma Physics and Controlled Nuclear Fusion*, Springer, 2005. 52

[116] C. Cheng, L. Chen, and M. Chance, Annals of Physics **161**, 21 (1985). 52

[117] I. Chapman et al., Nuclear Fusion **50**, 045007 (2010). 53, 54, 58, 59, 62, 90, 138

[118] J. Manickam and N. Pomphrey, **1461** (1987). 54

[119] R. Lake, S. Pinches, R. Akers, and E. Verwichte, Bulletin of the American Physical Society **57** (2012). 56

[120] S. Sharapov, Private Communication , 22/02/2013. 59

[121] C. Wahlberg and J. P. Graves, Physics of Plasmas **14**, 110703 (2007). 59

[122] R. Gill, A. Edwards, D. Pasini, and A. Weller, Nuclear Fusion **32**, 723 (1992). 60

[123] B. N. Breizman and S. E. Sharapov, Plasma Physics and Controlled Fusion **37**, 1057 (1995). 69

[124] S. E. Parker and W. W. Lee, Physics of Fluids B: Plasma Physics **5**, 77 (1993). 71

[125] T. Tajima and F. W. Perkins, Paper 2P9 (unpublished), in *Sherwood Theory Meeting*, 1983. 71

[126] M. Kotschenreuther, G. Rewoldt, and W. Tang, Computer Physics Communications **88**, 128 (1995). 71

[127] S. Jolliet et al., Computer Physics Communications **177**, 409 (2007). 71

[128] G. Hu and J. A. Krommes, Physics of Plasmas **1**, 863 (1994). 71

[129] R. Akers et al., Nuclear Fusion **42**, 122 (2002). 76

[130] R. J. Akers, E. Verwichte, T. J. Martin, S. D. Pinches, and R. Lake, GPGPU Monte Carlo calculation of gyro-phase resolved fast ion and n-state resolved neutral deuterium distributions ., in *39th EPS Conference & 16th Int. Congress on Plasma Physics*, 2012. 76, 78, 138

[131] R. J. Hawryluk, Physics of Plasmas Close to Thermonuclear Conditions, ed. by B. Coppi, et al. (CEC, Brussels) **1**, 19 (1980). 76, 146

[132] J. Ongena, M. Evrard, and D. McCune, Proceedings of the Third Carolus Magnus Summer School on Plasma Physics, (Spa, Belgium, Sept 1997), as published in Transactions of Fusion Technology **33**, 181 (1998). 76, 146

[133] A. Pankin, D. McCune, R. Andre, G. Bateman, and A. Kritz, Computer Physics Communications **159**, 157 (2004). 76, 145

[134] C. Hellesen et al., Plasma Physics and Controlled Fusion **52**, 085013 (2010). 76, 77

[135] J. Boris, Relativistic Plasma Simulation-Optimization of a Hybrid Code, in *Proceedings of the Fourth Conference on Numberical Simulation of Plasmas*, number NOVEMBER 1970, pages 3–67, 1970. 76

[136] H. Alfvén, *Cosmical Electrodynamics*, Clarenden Press, Oxford, England., second edition, 1950. 77

[137] M. D. Kruskal, Advanced Plasma Theory, in *Proceedings of the International School of Physics "Enrico Fermi" Course XXV*, edited by M. N. Rosenbluth, pages 260–266, Academic Press Inc. New York, 1964. 77, 78

[138] C. S. Gardner, Physics of Fluids **9**, 1997 (1966).

[139] T. J. Martin, Culham Report CLM-PDN 2/73: Computer Programs for Electromagnetic Field and Charged Particle Calculations Part 1, Technical report, 1973.

[140] V. Moiseenko, M. A. Surkova, and O. Å gren, Problems of Atomic Science and Technology , 56 (2011). 78

[141] R. Akers, Private Communication , 18/07/2012. 80

[142] S. D. Pinches et al., Plasma Physics and Controlled Fusion **46**, B187 (2004). 81

[143] D. Borba and W. Kerner, Journal of Computational Physics **153**, 101 (1999). 81, 82, 145

[144] B. N. Breizman et al., Physics of Plasmas **4**, 1559 (1997). 85

[145] F. Zonca et al., Plasma Physics and Controlled Fusion **48**, B15 (2006). 85

[146] I. T. Chapman, S. E. Sharapov, G. T. a. Huysmans, and a. B. Mikhailovskii, Physics of Plasmas **13**, 062511 (2006). 85

[147] A. Field et al., Nuclear Fusion **51**, 063006 (2011). 85

[148] L. Lao, H. St. John, R. Stambaugh, A. Kellman, and W. Pfeiffer, Nuclear Fusion **25**, 1611 (1985). 85, 145

[149] G. T. A. Huysmans, J. P. Goedbloed, and W. Kerner, No Title, in *CP90 Conf. Comput. Phys.*, 1990. 86, 145

[150] G. Hommen et al., The Review of scientific instruments **81**, 113504 (2010). 86, 145

[151] A. B. Mikhailovskii, G. T. A. Huysmans, W. O. K. Kerner, and S. E. Sharapov, Plasma Physics Reports **23**, 844 (1997). 89, 145

[152] V. Marchenko and S. Reznik, Nuclear Fusion **51**, 122001 (2011). 91

[153] R. B. White, *Toroidially Confined Plasmas*, Imperial College Press, London, second edition, 2001. 97

[154] M. Turnyanskiy et al., Measurement and control of the fast ion redistribution on MAST, in *24th IAEA Fusion Energy Conference*, 2012. 104

[155] D. Stork, The upgrade to the Mega Amp Spherical Tokamak, in *Proc. 23rd IAEA Fusion Energy Conf. . (Daejeon, Korea)*, 2010. 107, 139

[156] A. W. Morris, IEEE Transactions on Plasma Science **40**, 682 (2012). 107, 139

[157] T. R. Barrett et al., Fusion Engineering and Design **86**, 789 (2011). 107

[158] M. Turnyanskiy et al., Nuclear Fusion **53**, 053016 (2013). 119, 139, 140, 144

[159] A. Bovet, *Anomalous Diffusion of Fast Ions in the Presence of Fishbone Instabilities in Tokamaks*, Masters thesis, École Polytechnique Fédérale Lausanne, 2009. 119, 120, 139

[160] M. Turnyanskiy, Private Communication (2012). 128

[161] R. J. Akers et al., Plasma Physics and Controlled Fusion **45**, A175 (2003). 128

[162] M. Turnyanskiy et al., Measurement and control of the fast ion redistribution on MAST, in *Proceedings of the 24th IAEA Fusion Energy Conference*, 2012. 130, 133

[163] S. Conroy, LINE2, Department of Physics and Astronomy, Uppsala University, EURATOM-VR Association, Uppsala, Sweden. 133, 145

[164] I. Wodniak et al., TRANSP modelling of neutron emissivity on MAST, in *39th EPS Conference & 16th Int. Congress on Plasma Physics*, 2012. 133, 136, 139

[165] O. M. Jones et al., Plasma Physics and Controlled Fusion **Submitted** (2013). 137, 140, 141

[166] C. P. von Thun et al., Nuclear Fusion **50**, 084009 (2010). 139

[167] C. Perez von Thun et al., Nuclear Fusion **52**, 094010 (2012). 139

[168] S. Pinches, A. Bovet, M. Turnyanskiy, and t. M. Team, Fast Ion Driven Instabilities in MAST, in *11th IAEA Technical Meeting on Energetic Particles in Magnetic Confinement Systems, Kyiv, Ukraine.*, 2009. 139

[169] S. Pinches et al., Nuclear Fusion **46**, S904 (2006). 139

[170] M. Garcia-Munoz et al., Nuclear Fusion **51**, 103013 (2011). 139

[171] N. Fisch and J.-M. Rax, Physical Review Letters **69**, 612 (1992). 140

[172] N. Fisch, Physical Review Letters **97**, 225001 (2006). 140

[173] A. Beliën, M. Botchev, J. Goedbloed, B. van der Holst, and R. Keppens, Journal of Computational Physics **182**, 91 (2002). 140

[174] J. W. S. Blokland and S. D. Pinches, Plasma Physics and Controlled Fusion **53**, 105009 (2011). 140

[175] J. Blokland, B. van der Holst, R. Keppens, and J. Goedbloed, Journal of Computational Physics **226**, 509 (2007). 140, 145

[176] A. Morris et al., Fusion Engineering and Design **74**, 67 (2005). 141

[177] M. Ono et al., Plasma Physics and Controlled Fusion **45**, A335 (2003). 141